Multichannel SAR Range Ambiguity Suppression Method Based on Blind Source Separation

Zur Erlangung des akademischen Grades eines

DOKTOR-INGENIEURS

von der KIT-Fakultät für
Elektrotechnik und Informationstechnik
des Karlsruher Instituts für Technologie (KIT)

genehmigte

DISSERTATION

von

M.Sc. Ershad Junus Amin
geb. in Wonosobo, Central Java, Indonesien

Tag der mündlichen Prüfung: 06.12.2024

Hauptreferent: Prof. Dr.-Ing. habil. Alberto Moreira
Korreferent: Prof. Dr. Antonio Iodice

Acknowledgements

Completing this doctoral thesis has been a long, challenging, and rewarding journey. I would not have reached this milestone without the support, guidance, and encouragement of many individuals and institutions, to whom I am deeply grateful.

First and foremost, I express my deepest gratitude to my supervisor, Prof. Dr. Gerhard Krieger, for his unwavering support and insightful guidance. His expertise and critical feedback have been invaluable in shaping my research and helping me grow as a scholar.

I am equally thankful to my mentor, Dr. Federica Bordoni, for her support and steadfast patience, particularly during the demanding process of journal writing.

I extend my sincere appreciation to my other supervisor and group head, Prof. Dr. Marwan Younis, for his valuable discussions and continuous support throughout my doctoral journey.

I am also profoundly grateful to my advisor, Prof. Dr. Alberto Moreira, for granting me the opportunity to conduct my research at his institute and for his encouragement and guidance during this doctoral journey.

I also extend my gratitude to my co-advisor, Prof. Dr. Antonio Iodice, and the KIT professors for their efforts in evaluating my thesis and for serving on my defense examination committee.

I acknowledge the Indonesia Endowment Fund for Education (LPDP) for generously sponsoring the first four years of my doctoral study, without which this research would not have been possible.

My deep appreciation goes to my colleagues at DLR for their academic and emotional support. The stimulating discussions, brainstorming sessions, and friendship helped make the challenges of this journey more manageable.

I am deeply grateful to my parents for their unwavering love, prayers, and emotional support, which have been an unwavering motivation throughout my doctoral journey.

Lastly, and most importantly, my heartfelt gratitude goes to my wife, my son, and my soon-to-be-born daughter. They have been my biggest supporters, my source of happiness, and my greatest motivation during the ups and downs of this doctoral journey. I love them more than words can express.

Zusammenfassung

Zukünftige weltraumgestützte SAR-Systeme werden mehrkanalige SAR-Architekturen mit mehreren Empfangsstrahlen in Elevation verwenden, um mehrere Abbildungsstreifen zu erfassen. Dies ermöglicht gleichzeitig eine hohe Azimutauflösung und eine große Abbildungsstreifenbreite – Ziele, die mit heutigen modernen SAR-Systemen im Wesentlichen unerreichbar sind. Eine inhärente Herausforderung dieser Systeme ist jedoch das Auftreten von Entfernungsmehrdeutigkeiten, die eine wesentliche Quelle für die Verschlechterung der Bildqualität darstellen. Entfernungsmehrdeutigkeiten entstehen durch unerwünschte Radarechos, die von außerhalb des betrachteten Abbildungsstreifens stammen.

Die derzeitigen Techniken zur Unterdrückung von Mehrdeutigkeiten in der Entfernung basieren stark auf der Kenntnis der Richtcharakteristik der Antenne. Die genaue Schätzung dieser Richtcharakteristik ist jedoch aufgrund von Faktoren wie digitalen Kanalfehlern, Unsicherheiten in der Kalibrierung der Richtcharakteristik, fehlerhafter Ausrichtung und Antennenverformungen herausfordernd. Infolgedessen nehmen die Entfernungsmehrdeutigkeiten erheblich zu, was sich negativ auf die Bildqualität auswirkt.

In dieser Doktorarbeit wird ein neuartiges Verfahren zur Unterdrückung von Entfernungsmehrdeutigkeiten vorgestellt, das unabhängig von der Kenntnis der Richtcharakteristik ist. Dadurch wird das Verfahren robust gegenüber Fehlerquellen, die typischerweise die durch die Entfernungsmehrdeutigkeiten verursachten Störungen verstärken. Das Verfahren wird am Boden implementiert, wobei die heruntergeladenen SAR-Daten als Eingabe dienen. Dadurch wird die zusätzliche Komplexität der Verarbeitung an Bord vermieden – ein häufiges Problem bei modernen Verfahren zur Unterdrückung von Entfernungsmehrdeutigkeiten.

Das Schlüsselkonzept, das in dieser Doktorarbeit untersucht wird, ist das Cocktailparty-Phänomen in mehrkanaligen SAR-Systemen mit mehreren Elevationsstrahlen. Folglich wird die blinde Quellentrennung (Blind Source Separation, BSS) als Technik eingesetzt, um dieses Cocktailparty-Problem im Mehrkanal-SAR zu lösen, wobei die Statistik der Eingabedaten genutzt wird. Ergänzt durch eine Optimierungsstrategie, unterdrückt die in dieser Arbeit vorgestellte Methode erfolgreich die Entfernungsmehrdeutigkeiten und überwindet so die Herausforderungen bei der Implementierung von BSS, die durch die statistischen Nachteile mehrdeutiger SAR-Daten entstehen. Die Arbeit stellt zudem eine Technik zur Behandlung homogener SAR-Signale vor, bei denen BSS tendenziell schlechtere Ergebnisse liefert.

Die in dieser Arbeit durchgeführten Simulationen beziehen sich auf zwei etablierte Arten von SAR-Systemen, die entweder planare Antennen oder Reflektorantennen verwenden und jeweils unterschiedliche Probleme mit Entfernungsmehrdeutigkeiten aufweisen. Darüber hinaus werden verschiedene Szenarien mit unterschiedlichen Homogenitätsgraden untersucht, von stark heterogenen bis hin zu extrem homogenen SAR-Bildern, um die Robustheit der vorgeschlagenen Methode zu validieren.

Abstract

Future spaceborne SAR systems will employ multichannel SAR architectures with multiple receive beams in elevation to map multiple swaths, enabling the simultaneous achievement of high azimuth resolution and wide swath coverage — objectives that are fundamentally unattainable in current state-of-the-art SAR systems. However, an inherent challenge in these systems is the occurrence of range ambiguities, that are a significant source of image degradation. Range ambiguities arise from unwanted radar echoes originating outside the imaged swath.

Current state-of-the-art techniques for suppressing range ambiguities heavily rely on the knowledge of the antenna pattern. Yet, accurately estimating this pattern poses challenges due to factors like digital channel errors, pattern calibration uncertainties, mispointing, and antenna deformations. Consequently, range ambiguities significantly increase, impacting the image quality.

This doctoral thesis introduces a novel range ambiguity suppression method independent of antenna pattern knowledge, thereby offering robustness against error sources that typically amplify the range ambiguity disturbance. The method will be implemented on-ground, utilizing downlinked SAR data as input, thereby avoiding the addition of complexity to on-board processing - a common issue in state-of-the-art range ambiguity suppression techniques.

The key concept explored in this doctoral thesis is the cocktail party phenomenon within multichannel SAR systems featuring multiple elevation beams. Consequently, blind source separation (BSS) is employed as a technique to address this cocktail party problem in multichannel SAR, relying on the statistics of the input data. Alongside an optimization approach, the method in this thesis successfully suppresses range ambiguities, overcoming challenges in implementing BSS due to statistical disadvantages inherent in range ambiguous SAR data. The thesis also includes a technique to handle homogeneous SAR signals, where BSS tends to perform poorly.

Simulations conducted in this thesis cover two established types of SAR systems based on either planar antennas or array-fed reflector antennas, each presenting different range ambiguity disturbances. Moreover, diverse scenes with varying levels of homogeneity, ranging from highly heterogeneous SAR images to extremely homogeneous ones, are investigated to validate the proposed method's robustness.

Contents

List of Symbols and Acronyms

Constants

π	The ratio of a circle's circumference to its diameter	3.14159265359
c	Speed of light in vacuum	$2.99792458 \times 10^8 [m/s]$
R_E	Mean Earth radius	$6371 [km]$

Mathematical Notations and Symbols

j	Imaginary unit
$\circledast$	Convolution
$(\cdot)^*$	Conjugate
$(\cdot)^T$	Transpose
$(\cdot)^H$	Conjugate transpose
$\in$	Element of
$\subset$	Subset of
$\lvert\lvert \cdot \rvert\rvert$	L^2-norm
$[\cdot]$	Iverson bracket serving as the indicator function
$\lfloor \cdot \rfloor$	Floor operator (lower integer)
$E\{\cdot\}$	Expectation value operator
$\mathbb{C}$	Set of complex numbers

Acronyms

AF	Array Factor
AMUSE	Algorithm for Multiple Unknown Signals Extraction
APC	Azimuth Phase Coding

BSS	Blind Source Separation
C-RABSS	Calibrated Range Ambiguity Suppression based on Blind Source Separation
CS	Chirp Scaling
CSA	Chirp Scaling Algorithm
CSK	Complex Signal Kurtosis
DBF	Digital Beamforming
DoA	Direction of Arrival
DEM	Digital Elevation Model
DLR	Deutsches Zentrum für Luft- und Raumfahrt
EF	Element Factor
EP	Equivalent Pattern
ERS	European Remote Sensing
ESA	European Space Agency
EVD	Eigen Value Decomposition
FFT	Fast Fourier Transform
FM	Frequency Modulation
HO	Higher-Order
HRWS	High-Resolution Wide-Swath
ICA	Independent Component Analysis
IFFT	Inverse Fast Fourier Transform
IRF	Impulse Response Function
IRW	Impulse Response Width
ISLR	Integrated Sidelobe Ratio
ITU	International Telecommunication Union
JADE	Joint Approximate Diagonalization of Eigen-matrices
JERS	Japanese Earth Resources Satellite
LCMV	Linear Constraint Minimum Variance (beamformer)
MFSP	Multifrequency Subpulse

MIMO	Multiple-Input Multiple-Output
MSE	Mean Squared Error
MVDR	Minimum Variance Distortionless Response
NASA	National Aeronautics and Space Administration
NESZ	Noise Equivalent Sigma Zero
PPC	Pulse Phase Coding
PRF	Pulse Repetition Frequency
PRI	Pulse Repetition Interval
PSLR	Peak Sidelobe Ratio
RADAR	Radio Detection and Ranging
RABSS	Range Ambiguity Suppression based on Blind Source Separation
RASR	Range Ambiguity-to-Signal Ratio
RC	Range Compressed
RCM	Range Cell Migration
RCMC	Range Cell Migration Correction
RF	Radio Frequency
Rx	Receive
SAR	Synthetic Aperture Radar
SCORE	Scan-on-Receive
SNR	Signal-to-Noise Ratio
SIMO	Single-Input Multiple-Output
SO	Second-Order
SOBI	Second-Order Blind Identification
SRTM	Shuttle Radar Topography Mission
SVD	Singular Value Decomposition
TDL	Tandem-L
TDX	TanDEM-X
TSX	TerraSAR-X
ToA	Time of Arrival

TOPS	Terrain Observation by Progressive Scans
TRM	Transmit-Receive Module
Tx	Transmit

Lower Case Letters

a	Element of mixing matrix
$\hat{a}$	Element of estimated mixing matrix
$\bar{a}$	Mean of mixing matrix
$\bar{\hat{a}}$	Mean of estimated mixing matrix
a_{scl}	Modified chirp scaling factor
$\mathbf{c}$	Constraint vector
d	Spacing between channels
d_r	Diameter of reflector antenna
e	Digital channel error
f_τ	Range frequency
f_0	Center frequency
f_s	Sampling frequency
f_t	Doppler frequency
$f_{t,max}$	Maximum unambiguous Doppler shift
g	Complex-value antenna pattern
g_{RX}	Complex-value Rx antenna pattern
g_{TX}	Complex-value Tx antenna pattern
g_{DBF}	Complex-value DBF antenna pattern
g_{nom}	Nominal (error-free) antenna pattern
g_{actual}	Actual antenna pattern
g_τ	Elevation antenna pattern
g_t	Azimuth antenna pattern
g''	SCORE equivalent pattern
$\mathbf{g}$	Array steering vectors
$h(t)$	Matched filter in time domain
h_{orbit}	Orbit height
k	Ambiguity order

k_r	Range chirp rate
k_x	Wavenumber in x-direction
k_y	Wavenumber in y-direction
k_{min}	Threshold for separation index
$l(i)$	Permutation order of i-th row
l_{fc}	Focal length of reflector antenna
m_{kl}	Elements of transformed matrix $\mathbf{M}$ with size $k \times l$
n	Noise
r	Correlation coefficient between estimated and actual mixing matrix
r_{ref}	Range reference in chirp scaling algorithm
$r_{0,scl}$	Inverse scaled location vector
$\mathbf{s}$	Original or useful signals / emitted voices
$\mathbf{s}'$	Original or useful signals in the range-compressed data
s'_w	Weighted range-compressed signal
$\mathbf{s}''$	Original or useful signals in the focused data / image
s_{idx}	Separation index
$s_r(t)$	Received signal in time domain
s_{TX}	Transmitted signal
$s_{out}(t)$	Compressed signal in time domain
s_{RA}	Range ambiguity signal
$\mathbf{s}_{WA}$	Out-of-swath ambiguity signals
$\hat{s}$	Estimated signal
t	Azimuth or slow time
$\mathbf{v}$	Stationary noise vector in the channel array
$\mathbf{w}$	Complex weight vector in the channel array
$\mathbf{x}$	Received signals or DBF signals
x'	Received signals in the range-compressed data
x''	Received signals in the focused data/image
y	Channel's received signal
$\mathbf{z}$	Whitened signal

Capital Letters

$\mathbf{A}$	Mixing matrix

$\hat{\mathbf{A}}$	Estimated mixing matrix
$\mathbf{A}_{PLA}$	Planar antenna mixing matrix
$\mathbf{A}_{STA}$	Stationary mixing matrix
$\mathbf{A}_{TDL}$	Reflector antenna mixing matrix
$\mathbf{A}_{LOW}$	Stationary low-value mixing matrix
A_d	Arbitrary value of the amplitude deformation of the reflector, located at its focal point
$\mathbf{B}$	Unmixing or separation matrix
$\hat{\mathbf{B}}$	Estimated separation matrix
$\mathbf{B}_{ref}$	Reference or calibrated separation matrix
B_t	Doppler bandwidth
$B_{t,proc}$	Processed Doppler bandwidth
B_τ	Chirp or range bandwidth
$B_{\tau,proc}$	Processed range bandwidth
D_r	Displacement between useful and range ambiguity signal
$\mathbf{D}$	Square matrix in EVD, whose columns are the eigenvectors
$\mathbf{E}_{mat}$	Estimation error of mixing matrix
$\mathbf{F}$	Transformed matrix in matrix-to-matrix transformation. Cumulant Matrix
$\mathbf{G}$	Matrix of complex-value antenna pattern
H_{az}	Phase function of the azimuth chirp in frequency
H_{rc}	Phase function of the range chirp in frequency
H_{rcm}	Phase function of bulk RCM
H_{cs}	Phase function of chirp scaling
$\mathbf{I}$	Identity matrix
K_a	Azimuth FM rate
L_a	Antenna length or aperture
L_s	Synthetic aperture
M	Number of receivers
$\mathbf{M}$	Matrix that is transformed by matrix-to-matrix transformation. Eigenmatrix
N	Number of sources or illuminated sub-swaths. Number of simultaneously received elevation beams
N_ρ	Number of quarter period deformations w.r.t. radius p
N_φ	Number of half period deformations w.r.t. angle φ
N_a	Number of azimuth samples

N_{act}	Number of active feed elements
N_{chel}	Number of digital channels in elevation
N_{dir}	Number of different directions in range
N_{elem}	Number of antenna elements in array grid
N_r	Number of range samples for each subswath
N_{sta}	Number of stacked azimuth lines
N_{sub}	Number of Doppler sub-bands
$\mathbf{N}_r$	Set of eigenmatrices to be diagonalized
$\mathbf{P}$	Permutation matrix
$\mathbf{Q}$	Matrix in JADE that need to be diagonalized
R	Slant range
$\mathbf{R}_{cov}$	Covariance matrix of the received signals at the array
R_0	Slant range distance to the target at its closest approach. Slant range of useful signal
R_{RA}	Slant range of range-ambiguous signal
$\mathbf{R}_v$	Channel covariance matrix of thermal noise
R_{max}	Maximum slant range of an unambiguous swath
R_{min}	Minimum slant range of an unambiguous swath
T_r	Pulse length
$\mathbf{U}$	Second rotation matrix in SVD
$\mathbf{V}$	First rotation matrix in SVD
V_g	Ground velocity
V_r	Effective velocity
V_s	Platform velocity
$\mathbf{W}$	Whitening matrix. Complex-valued weight matrix in channel array
W_g	Swath width extension to the ground

Greek Symbols

α	A factor of scaling of the image in the range direction
α_D	Doppler angle
τ	Range or fast time
τ_0	Range-time delay
$\beta(f_t)$	Azimuth modulation term
θ_0	Steering angle to the target of interest
θ_s	Look angle
θ_{bw}	Azimuth beamwidth
$\theta_{bw,s}$	Synthesized half-power beamwidth
θ_{max}	Swath maximum look angle
θ_{min}	Swath minimum look angle
θ_{tilt}	Elevation tilt angle w.r.t. nadir
λ	Wavelength
δ	Range impulse response
δ_a	Azimuth resolution in SAR
δ'_a	Azimuth resolution in traditional radar
$\delta_{r,pulse}$	Range resolution of a pulsed radar
$\Delta\varphi$	Residual phase term generated after range compression
Δz	Deformation of reflector antenna
φ	Deformation angle in reflector antenna
η	Incident angle
η_{SL}	Sidelobe constraint
$\theta(\tau)$	Off-boresight angle
ϑ	Pointing angle
ϑ_0	Main beam pointing angle
ϑ_{SL}	Sidelobe pointing angle
ϵ	Uncertainty magnitude of antenna pattern
$\mathcal{K}_z$	Fourth-order cumulant of $\mathbf{z}$
ϕ_s	The angle between the range elevation plane and the spacecraft orbital plane
ϕ_0	Azimuth angle of target of interest
ϕ_{uni}	Uncertainty phase of antenna pattern
ρ	Deformation radius in reflector antenna
ρ_c	Radius of reflector

ξ	Magnitude error of antenna pattern
ζ	Phase error of antenna pattern
σ	Backscatter coefficient
Σ	Stretching matrix in SVD
Λ	Diagonal matrix in EVD
ΔR	Amount of RCM to correct
ΔR_{max}	Amount of RCM to correct in the case of maximum RCM
ΔRCM	Amount of uncorrected RCM due to mismatch
μ	Moment of a function
μ'	Standardized moment of a function
$\mathcal{C}$	Cost function in JADE
$\mathcal{CSK}$	Complex Signal Kurtosis
$\mathcal{N}$	Set of cumulant matrices

Subscripts and Superscripts

RX	Receive
t	Azimuth or slow time
TX	Transmit
τ	Range or fast time
$'$	Range-compressed data
$''$	Focused data / image

1 Introduction

1.1 Background

The history of radar dates back to the late 19th - early 20th century when scientists and engineers began to explore the possibilities of using radio waves to detect objects. James Clerk Maxwell's groundbreaking theory in 1865 laid the foundation, proposing the existence of electromagnetic waves [1]. Just over two decades later, Heinrich Hertz confirmed their existence in 1888 and even observed their reflection off metal objects [2]. However, it was Christian Hülsmeyer in 1904 who took the concept a step further. His *Telemobiloscope* – a device for detecting distant metallic objects like ships, even in challenging conditions like darkness, fog, or rain – marked the birth of practical radar principles [3].

Despite the *Telemobiloscope*'s limited adoption due to technological constraints, radio communication thrived in the early 20th century. In 1897, Guglielmo Marconi's successful demonstration of wireless communication sparked global interest, fueling rapid advancements in radio frequency (RF) technology [4]. Motivated by mostly military applications in the 1930s, the development of practical radar systems gained momentum. In 1935, Sir Robert Watson-Watt and his team further refined the radar system, and their efforts led to the establishment of the Chain Home radar system in the UK [5]. It was a network of ground-based radar stations used for detecting incoming enemy aircraft during World War II.

In the 1940s, radar technology was miniaturized, allowing for installation in aircraft and thus marking the transition from ground-based radar to aerial-based radar. Airborne radar systems provided critical advantages during World War II [6]. Airborne radar enabled nighttime operations, navigation assistance, and detection of enemy aircraft. It greatly enhanced the capabilities of military aircraft. The development of airborne radar systems continued after the war, leading to advancements in target tracking, terrain mapping, and weather detection.

After World War II, radar technology continued to evolve. Magnetron tubes and other technological improvements led to smaller and more powerful radar systems [7]. In the 1950s, a new concept of aerial-based radar, known as synthetic aperture radar (SAR), was invented by Carl Wiley [8]. SAR uses the motion of the radar platform to create a virtual aperture, resulting in higher-resolution images [9]. In the late 1950s and early 1960s, experimental SAR flights were conducted to validate the concept of synthetic aperture imaging. These early flights involved mounting radar systems on aircraft and collecting radar data while flying over specific areas of interest. The collected data were processed using optical processing systems to create SAR images.

Since 1960s, efforts were made to develop SAR systems that could be deployed on satellites. In December 1964, the US Air Force launched a reconnaissance satellite named Quill, which provided the first images of Earth from space using SAR [10]. Project Quill was probably the first, but most of the results are lost. In 1978, coinciding with the era when digital computers attained the capability to process SAR data, National Aeronautics and Space Administration (NASA) launched the first civilian spaceborne SAR satellite SEASAT [11], which stimulated a number of further developments. In the 1990s, an innovation in planar SAR antenna technology was introduced with the use of slotted waveguides as basic antenna elements, allowing to transmit more power, adopted in the European ERS-1, ERS-2 [12], the Japanese JERS-1 [13], the US/Italian/German Shuttle missions SIR-C/X-SAR [14] and SRTM [15], and the Canadian Radarsat-1 [16]. These SAR missions demonstrated the feasibility of spaceborne SAR imaging, allowing global coverage.

In the 2000s, SAR technology has witnessed continuous advancements, with a major leap forward coming from the miniaturization of radio wave generators and the availability of Transmit/Receive (TR) modules. This advancement paved the way for a new generation of SAR satellites equipped with active phased array antennas, such as the European ENVISAT ASAR [17], the Japanese ALOS PALSAR [18], the Canadian Radarsat-2 [19], the Italian COSMO-SkyMed [20], and the German TerraSAR-X (with its add-on TanDEM-X) [21]. While ScanSAR mode for broader coverage was available in SRTM and Radarsat-1 using passive phase shifter, the ScanSAR mode utilizing active phased array offers higher flexibility and faster response time, providing rapid beam steering. Additionally, new operational imaging modes like high-resolution Spotlight mode, implemented on TerraSAR-X, TanDEM-X, and Radarsat-2, became available.

Today, SAR technology continues to evolve. NewSpace SAR is revolutionizing Earth observation with constellations of smaller, cheaper satellites [22]. Companies like ICEYE [23], Umbra Space [24], and Capella Space [25] are key players in this rapidly evolving field with agile missions, prioritizing frequent updates over the traditional SAR. While individual satellites may have limitations, the constellation design offers rapid revisits for timely monitoring (such as floods, weather), expanded coverage for broad trends (like deforestation, ship traffic), and potentially more affordable data, making SAR technology more accessible and dynamic.

1.2 Future Spaceborne SAR Systems

The development of spaceborne SAR is a collaborative effort involving multiple scientists and engineers. State-of-the-art spaceborne SAR missions represent an impressive endeavor that combines cutting-edge technology, advanced satellite systems, and sophisticated data processing techniques, ultimately revolutionizing Earth observation.

The driving requirement of state-of-the-art SAR missions is to achieve a high spatial resolution and to image a wide swath. Notably, the TerraSAR-X mission, launched in 2007, has played a pivotal role in advancing SAR imaging with its exceptional spatial resolution better than 1 meter for spotlight mode [21]. This remarkable level of detail enables the detection of fine-scale features, facilitates precise mapping of land surfaces, and supports diverse applications such as urban planning, environmental monitoring, and infrastructure management.

Furthermore, state-of-the-art SAR missions strive to provide wide swath coverage for efficient monitoring of vast areas. The Sentinel-1 mission, a prominent component of the European Union's Copernicus program, serves as an example of this capability. Through its various imaging modes Sentinel-1 achieves a swath width of up to 400 km [26]. This extensive coverage allows for rapid data acquisition and facilitates crucial applications such as disaster response, maritime surveillance, and land cover monitoring.

While state-of-the-art spaceborne SAR systems have made significant advancements, there exists still a fundamental trade-off between achieving high azimuth resolution and wide-swath coverage in SAR systems. Increasing the azimuth resolution typically requires longer synthetic aperture associated with a higher Doppler bandwidth, consequently demanding a higher pulse repetition frequency (PRF), thereby reducing the unambiguous swath width that can be covered within a given time frame. Conversely, widening the swath coverage requires wider antenna beams in elevation paired with a lower PRF and, consequently, reduced azimuth resolution.

Future spaceborne synthetic aperture radar (SAR) systems are poised to address the trade-off between high-resolution imaging and wide-swath coverage, enabling the achievement of both capabilities simultaneously. Mission proposals like Tandem-L [27], and missions such as NISAR [28] (which is going to be launched soon) have been developed to embody this capability by employing multiple receive beams in elevation to map a wider swath while maintaining a high PRF to preserve high azimuth resolution. To realize this capability, these missions utilize multiple digital channels in the receiver and employ digital beamforming (DBF) techniques. DBF enables the simultaneous formation of multiple elevation beams, a capability that cannot be achieved with other state-of-the-art SAR systems. These missions push the boundaries of SAR technology, paving the way for enhanced imaging capabilities and a broader range of applications in remote sensing and Earth observation.

1.3 Motivation

One of the main disturbances which can cause a reduced SAR performance are range ambiguities. Range ambiguities are defined as a disturbance due to the unwanted echo that comes from the outside of the intended image swath. Figure 1.1 shows how range ambiguities can affect an image, where the part of the imaged swath supposed to be ocean is disturbed by range ambiguities coming from the echo of the mountainous region on the left side. Typically, the unwanted echo of the mountains in the picture is due to the high level of the antenna pattern sidelobes.

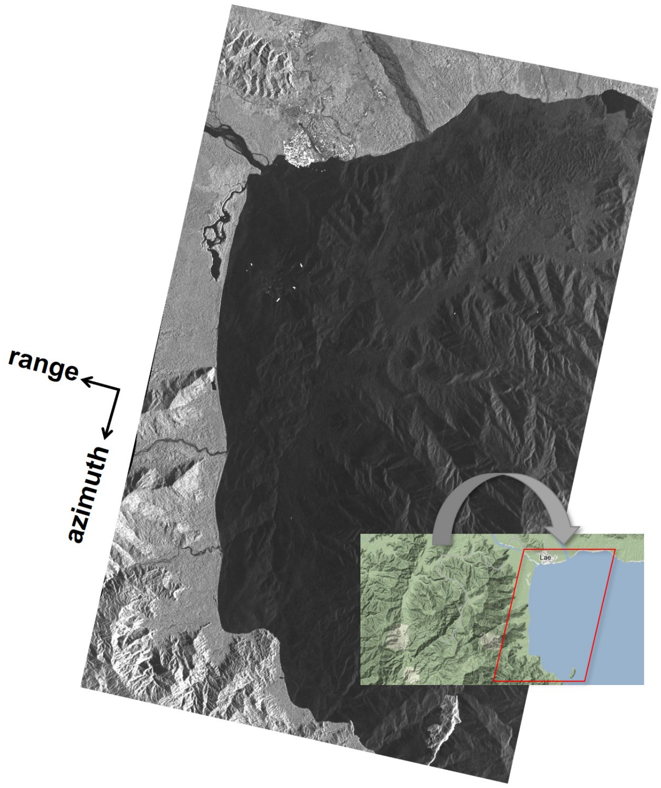

Figure 1.1: An example of range ambiguities in SAR, observed as a mountain-like appearance in the ocean, which originates from a mountain scene outside the intended SAR imaging area. The image is from [29].

In state-of-the-art SAR systems, which employ a single Tx/Rx beam, the range ambiguities are suppressed by both the Tx and Rx beams. However, in a future SAR system where multiple Rx beams are utilized, the range ambiguities due to sidelobes of the Rx beams are not attenuated by the Tx beam due to the wide illumination. As a result, the range ambiguities in future SAR systems requires greater attention than in state-of-the-art SAR systems where only a single Rx beam is used.

Some methods are suggested in the literature to suppress range ambiguities. Waveform variation methods like in [30] have been investigated using alternating up and down chirp waveforms, which ultimately spread the energy of ambiguous signals in the range dimension rather than eliminating them. Therefore, this technique is not applicable in a scene with extended targets [31]. An enhanced technique using a waveform diversity technique followed by a dual-focus post-processing step as proposed in [32], [33] allows the suppression of range ambiguities, but is only suitable for scenarios with very high range ambiguities, which are not common in real-world scenarios. Azimuth phase coding (APC) is a technique to reduce the range ambiguities rather than spread it [34]. This technique produces different azimuth frequency displacements between the spectrum of the desired echo and the undesired echo from a different ambiguous range region so that the undesired echoes can be suppressed through Doppler filtering. Accordingly, the amount of the ambiguous energy that can be removed depends on the Doppler oversampling rate. However, the Doppler oversampling rate is usually limited for wide swath coverage, which may seriously affect the suppression performance of APC. Another phase coding technique, named pulse phase coding (PPC) as proposed in [35], [36], also requires higher PRF for effective suppression of range ambiguities. The range phase coding proposed in [37], in combination with APC, can relax the requirement of the Doppler oversampling rate, but at the cost of an increased range oversampling rate. Furthermore, multi-frequency subpulse (MFSP) methods exploit the available radar signal bandwidth to increase the imaged swath extension, without the emergence of range ambiguities [38]. However, this comes at the cost of a reduced bandwidth, leading to a lower resolution. Therefore, when high resolution imaging is desired, the MFSP method may require a wide radar signal bandwidth. However, obtaining such a large bandwidth may not always be feasible due to limitations imposed by the International Telecommunication Union (ITU) or the instrument itself.

The established suppression techniques which are relevant for the case of multiple elevation beam receive SAR systems are classified as deterministic techniques, in the sense that they require the precise knowledge of the actual antenna pattern to be able to effectively suppress the ambiguities. Some examples are the minimum variance distortionless response (MVDR) [39], [40], and the linearly constrained minimum variance (LCMV) [41], [42] beam formers. Two challenges are associated with deterministic techniques. First, they increase the on-board processing complexity, as they are executed in real-time on the satellite. Second, they are susceptible to errors or mismatches present in the actual pattern. The actual pattern is something that is extremely difficult to estimate due to the presence of the errors. As regards the mentioned issue on the precise pattern knowledge, it is necessary to perform calibration to measure the actual pattern, which is very difficult to do in reality due to geometry constraints, for instance in a spaceborne L-band reflector system with an antenna diameter of 15 meters. Furthermore, real-time calibration is desirable because the error changes with time, e.g., due to the temperature deformation. The state-of-the-art calibration technique for the previously mentioned issue is to perform in-orbit calibration, i.e., the calibration is performed during the commissioning and operational phase as proposed in [43], [44], [45], which estimates the actual direct-radiating antenna pattern. However, this method requires a transparency mode, i.e., a particular calibration mode that needs to be performed over natural terrain with flat topography. Such scenes are not widely available over the Earth in the context of real-time calibration.

This thesis focuses on exploiting the cocktail party phenomenon, a key concept underpinning this work, within multichannel SAR systems featuring multiple elevation beams. Consequently, a method based on blind source separation (BSS) is proposed, serving as a technique to suppress range ambiguities without requiring precise antenna pattern knowledge. The method ensures robustness against various error types contributing to inaccuracies in the antenna pattern model. Besides its robustness against errors, the method is designed for on-ground implementation by utilizing downlinked SAR data as its input, thereby avoiding additional on-board processing complexity. Thus, the motivation behind this thesis lies in achieving a robust range ambiguity suppression method without increasing on-board processing complexity, which distinguishes it from current state-of-the-art techniques.

The idea to develop a method based on the BSS technique to suppress range ambiguities in SAR systems was initially presented in [46]. The first results, which are also part of the material in this thesis, were presented in [47], [48]. The comprehensive analysis and results of using BSS in the case of multichannel SAR systems, also part of this thesis, are presented in [49], [50], [51]. During the course of this thesis, a similar method using BSS was developed and published in [52], [53]. As shown later in Section 5.4, the method developed in [52], [53], which assumes a real-valued mixing matrix and contains a single value, does not lead to satisfactory results in practice [49]. The method developed in this thesis assumes a more realistic scenario using a complex-valued mixing matrix with dependencies along the range and Doppler directions, as applicable to the Tandem-L mission proposal [40]. The assumption of a complex-valued mixing matrix is essential, as the range ambiguities in multichannel SAR systems is closely related to the task of accurately estimating not only the amplitude but also the phase of the mixing matrix.

1.4 Scope and Structure

The organization of this work is structured as follows:

Chapter 2 explores SAR systems in relation to the issue of range ambiguities. It provides the necessary background by reviewing the evolution from conventional SAR to next generation SAR systems. This review includes an analysis of the key technological differences between the two systems, as well as the limitations and challenges associated with each. These factors serve as the driving motivation for this thesis.

In Chapter 3, the concept of the cocktail party problem in SAR is introduced as the central concept behind the thesis. It is followed by an exploration of blind source separation (BSS), as the primary technique for solving the problem, along with a numerical analysis of the limitations and challenges associated with implementing BSS for a simple case of SAR signal.

Chapter 4 presents a comprehensive concept and solution for addressing the range ambiguity disturbance in a multichannel SAR system. It aims to establish an understanding of how the method can be implemented as a robust approach to suppress range ambiguities without increasing onboard complexity, which becomes the main objective of this thesis.

In Chapter 5, the numerical analysis of the method is conducted using simulated multichannel SAR data as an input. To ensure the realism of the data, a simulation procedure is elaborated upon in this chapter, as there is currently no operational system available. The simulation encompasses three different systems: first, a system with a range- and Doppler-independent mixing matrix, which is artificial but necessary for establishing the method's relevance; second, a system with a planar direct-radiating antenna; third, an array-fed reflector system. These three systems correspond to different dependency of mixing matrices in range and Doppler. The method is implemented and analyzed in each of these systems. Additionally, a relatively heterogeneous scene is utilized in this chapter to specifically examine how the method performs for different types of SAR systems.

In Chapter 6, a calibration method is proposed to complement the previously presented method. This calibration method serves as a solution to overcome the limitation of the method when dealing with relatively homogeneous SAR images. The chapter demonstrates how the method presented in Chapter 4 performs for various types of scenes, ranging from extremely homogeneous to extremely heterogeneous scenes. The method, without calibration, exhibits limited performance only in heterogeneous scenes. Therefore, a complementary calibration method is necessary to enhance its performance in homogeneous scenes as well.

Chapter 7 serves as the concluding chapter of the thesis, offering a summary of the material discussed throughout and providing an outlook on potential areas for further research. In addition, Appendix A is included, covering relevant complementary topics related to the thesis.

The new contributions of this thesis are summarized in the following:

- analytical derivation of the cocktail party condition in the case of multichannel SAR systems with multiple elevation receive beams (Chapter 3);
- development of a method for the suppression of range ambiguities in multichannel SAR systems based on BSS for heterogeneous scenes, that does not rely on the knowledge of the antenna pattern and does not increase the onboard complexity (Chapter 4);
- development of a multiple elevation receive beams SAR simulator using TerraSAR-X data to demonstrate the validity of the proposed method (Chapter 5);
- validation of the proposed method in three different simulated scenarios: a system with a range- and Doppler-independent mixing matrix, a system with a Doppler-dependent mixing matrix (planar direct-radiating antenna architecture), and a system with a range- and Doppler-dependent mixing matrix (array-fed reflector antenna architecture) (Chapter 5);
- extension of the proposed method for any type of backscattering surface (Chapter 6).

2 SAR Systems

This chapter provides the necessary background to this thesis by examining the technological evolution from conventional SAR to multichannel SAR systems. The chapter starts by outlining the fundamental principles of conventional SAR systems and then delves into their inherent limitations, specifically related to the issue of range ambiguities. Section 2.2 then explores multichannel SAR systems and how they surpass the constraints of conventional SAR systems. The challenges associated with range ambiguities in multichannel SAR systems are further examined in Section 2.2.2, serving as the driving motivation behind the work in this thesis.

2.1 Conventional SAR Systems

2.1.1 Basic SAR Principle

In SAR, the motion of the antenna allows for the synthesis of a large virtual antenna, which enables a higher azimuth resolution than what could be achieved with a stationary physical antenna [9], [54]. This is known as a synthetic aperture.

Figure 2.1 shows the side-looking acquisition geometry of a spaceborne SAR instrument, where the platform with an antenna of length L_a moves along the azimuth direction while illuminating the swath. The synthetic aperture can be modeled as the effective length of the antenna's path while receiving the echo reflections of the transmitted electromagnetic waves from an object within the real antenna beamwidth. The equation that describes the length of the synthetic aperture is given by [9]

$$L_s = \frac{0.886 \cdot R_0 \cdot \lambda}{L_a} \cdot \frac{V_s}{V_g}, \tag{2.1}$$

where R_0 is the distance to the target at its closest approach; λ the free-space wavelength; V_s the platform velocity; V_g the ground velocity; and the 0.886 factor is due to the 3-dB width of the sinc function, which models the antenna pattern of a planar antenna with uniform aperture excitation. It is noted that in the case of a reflector antenna, this factor is different. Furthermore, the synthesized half-power beamwidth along the azimuth direction is given by [9]

$$\theta_{bw,s} = \frac{0.886 \cdot \lambda}{2 \cdot L_s}. \tag{2.2}$$

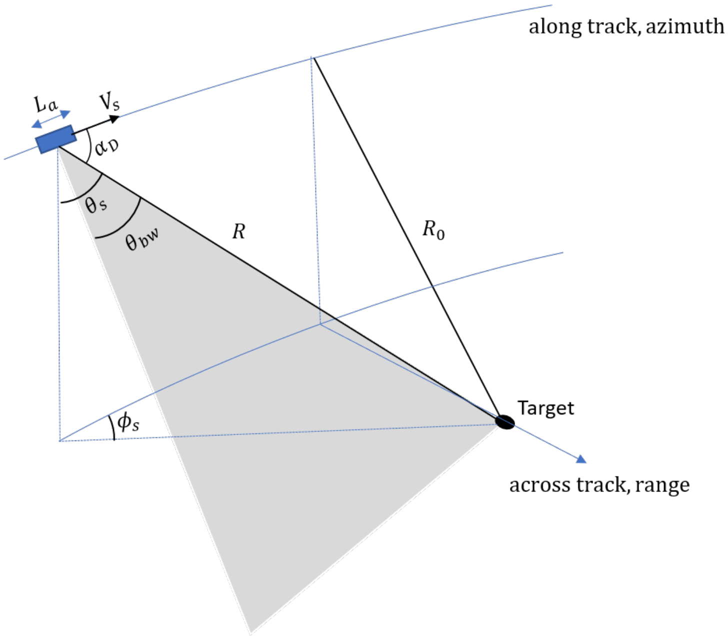

Figure 2.1: SAR data acquisition geometry, where V_s is the platform velocity; L_a the antenna length; α_D the Doppler angle; θ_s the look angle; θ_{bw} the real half-power antenna beamwidth; ϕ_s the angle between the range elevation plane and the spacecraft orbital plane; R the slant range; and R_0 the distance to the target at its closest approach.

Accordingly, the Doppler bandwidth is given by [9]

$$B_t = \frac{2 \cdot V_s}{\lambda} \cdot \theta_{bw}, \tag{2.3}$$

where θ_{bw} denotes the real half-power antenna beamwidth, and the azimuth resolution is given by [9]

$$\delta_a = \frac{0.886 \cdot V_g}{B_t}. \tag{2.4}$$

From the relationships between azimuth resolution, Doppler bandwidth, and antenna length, as shown in (2.2), (2.3), and (2.4) respectively, it is concluded that the azimuth resolution is inversely proportional to the Doppler bandwidth, while the Doppler bandwidth is also inversely proportional to the antenna length.

It is worth noting that while (2.3) represents the nominal Doppler bandwidth, the processed Doppler bandwidth in SAR processing is typically lower to mitigate azimuth ambiguities [55].

It is also useful to mention that the Doppler angle, α_D, is related to the look angle, θ_s and the angle between the range elevation plane and the spacecraft orbital plane, ϕ_s, as follows [56] :

$$\cos \alpha_D = \sin \theta_s \cdot \cos \phi_s. \tag{2.5}$$

On the other hand, the Doppler (or azimuth) frequency is expressed by [56]

$$f_t = \frac{2 \cdot V_s \cdot R_E}{\lambda} \cdot \frac{\alpha_D}{R}, \tag{2.6}$$

where R_E is the Earth radius; R the slant range distance.

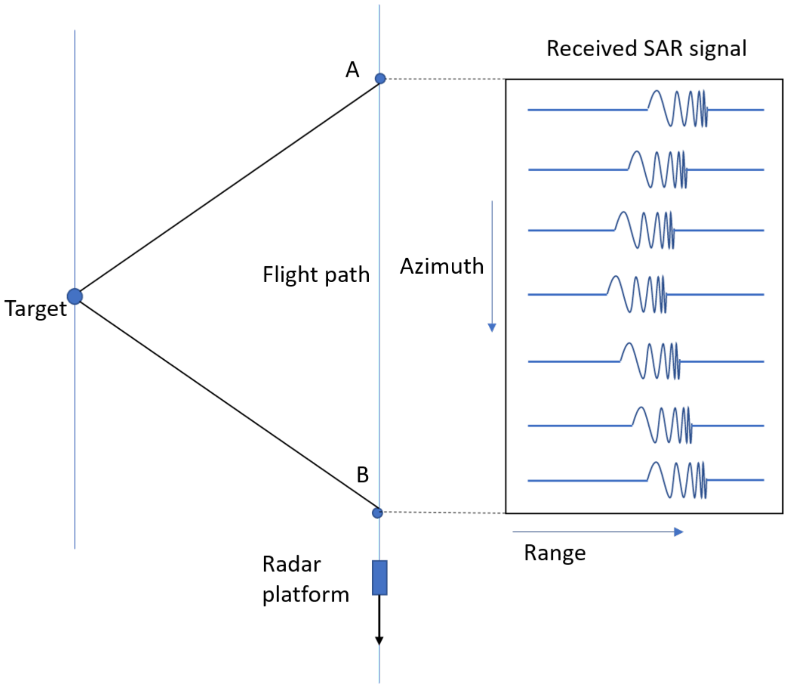

Figure 2.2: Representation of the received SAR data of a point target in the two-dimensional data memory. The target gets illuminated as the radar platform moves from point A to point B.

Due to the relative motion between the radar platform and the ground target, the slant range distance, R, to a target undergoes gradual changes over azimuth time, t, as described by the following equation [9]

$$R(t) = \sqrt{R_0^2 + V_s^2 \cdot t^2} \approx R_0 + \frac{V_s^2 \cdot t^2}{2 \cdot R_0}. \tag{2.7}$$

The approximation is valid for low squint and moderate synthetic aperture length, as the terms higher than the second order in the series expansion of the square root in (2.7) are very small.

The phenomenon of changing distance between the radar platform and a point target is known as range cell migration (RCM) [9], [54]. Figure 2.2 illustrates RCM for the acquired raw data of a point target, where the position of the radar echoes changes systematically in correspondence to the varying target distance. Furthermore, it is important to emphasize that throughout the remainder of this thesis, SAR data will be presented in a similar format as shown in Figure 2.2, with the horizontal axis denoting range and the vertical axis representing azimuth.

2.1.2 SAR Processing

Within a SAR system, upon reception of the receive (Rx) signal, the radar data remain in their raw data form, necessitating further processing to yield image data, often referred to as focused data [54]. One notable attribute of the received raw data is the previously discussed range cell migration (RCM) effect, which requires correction, because failure to adequately address RCM can lead to blurred target images, i.e., a worsening of the resolution [9].

Understanding RCM and RCM correction (RCMC) is crucial to comprehend how the method in this thesis deals with the range ambiguity disturbance, as discussed later in Chapter 4. Therefore, this section primarily focuses on SAR processing with respect to the RCMC. In fact, the distinctions among different SAR processing techniques, such as the range-Doppler algorithm, chirp scaling algorithm (CSA), omega-K, and SPECAN [9], [54], primarily revolve around their approaches for RCM correction (RCMC). In this thesis, the extended chirp scaling (ECS) algorithm [57] has been chosen as it is specifically designed to eliminate the need for an interpolator in RCM correction. ECS operates on the principle of chirp scaling, allowing the adjustment for range-variant RCM shifts through multiplication by phased weights, rather than relying on a time-domain interpolator.

The SAR processing using the ECS algorithm comprises the application of five major transfer functions as shown in Figure 2.3. These five functions are derived from [57]. First, the phase center of the raw signal, in the range time and azimuth frequency domain, is scaled in the range dimension using a chirp scaling function. This operation equalizes the range migration trajectory of every point target to that of a reference range, which is typically set to the mid range. The phase function of the chirp scaling in the range-Doppler domain is given by

$$H_{cs}(f_t,\tau) = \exp\left[j \cdot \pi \cdot k(f_t;r_{ref}) \cdot a_{scl}(f_t) \cdot \left(\tau - \frac{2 \cdot R(f_t;r_{ref})}{c}\right)^2\right], \tag{2.8}$$

where f_t denotes azimuth frequency; τ range time; $k(f_t;r_{ref})$ the modulation rate of the chirp signal of a range reference r_{ref}. $R(f_t;r_{ref})$ express the range migration in the range-Doppler domain, and $a_{scl}(f_t)$ is the modified chirp scaling factor, given by

$$a_{scl}(f_t) = a(f_t) + (1-\alpha) \cdot \frac{1+a(f_t)}{\alpha}, \tag{2.9}$$

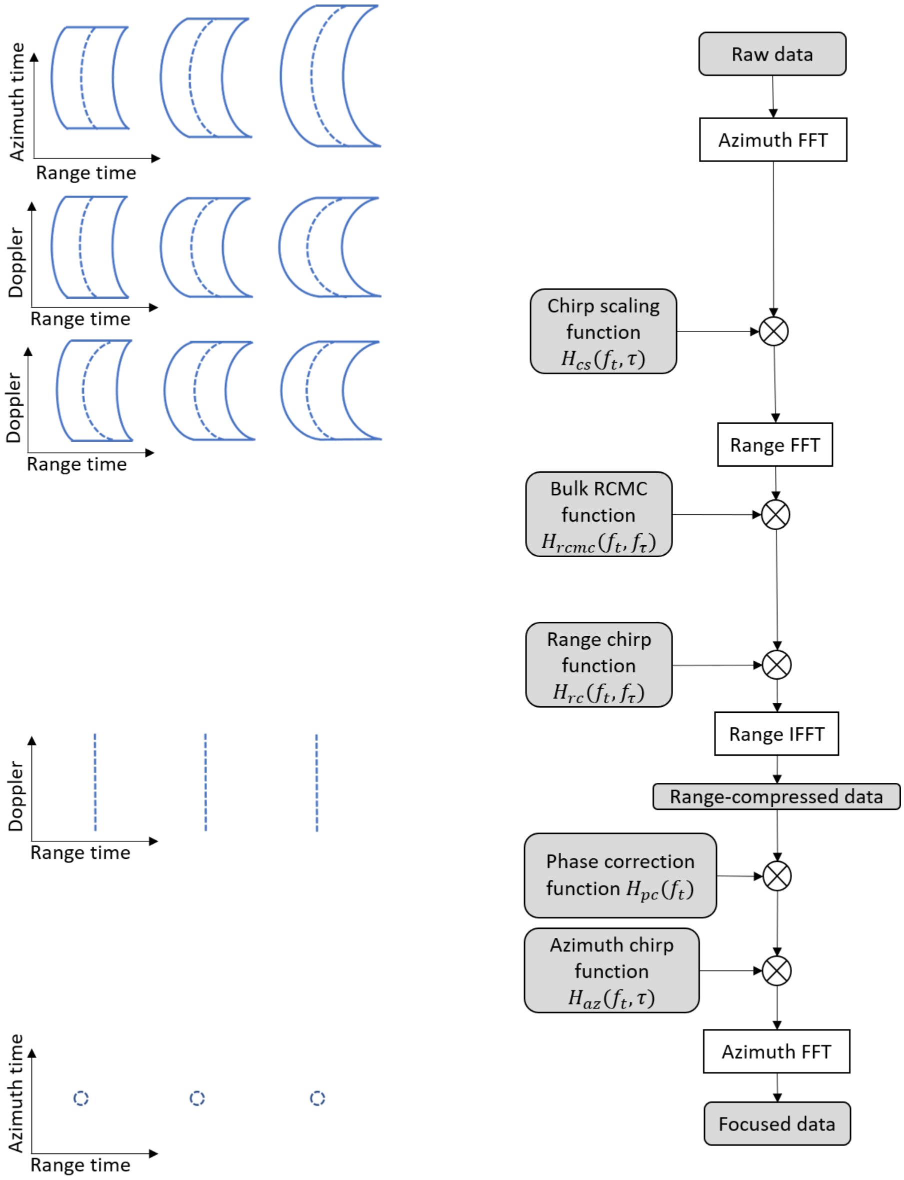

Figure 2.3: Block diagram of the SAR processing using the ECS algorithm. The SAR data signal representation in the range-time domain is shown on the left side for three point targets. The dotted lines in the signal representation correspond to the phase center of the signals in the range direction.

where α denotes a factor of scaling of the image in the range direction and $a(f_t)$ the normal chirp scaling factor, given by

$$a(f_t) = \frac{1}{\beta(f_t)} - 1, \tag{2.10}$$

where $\beta(f_t)$ is the azimuth modulation term, defined as

$$\beta(f_t) = \sqrt{1 - \left(\frac{f_t \cdot \lambda}{2 \cdot V_s}\right)^2}. \tag{2.11}$$

Second, the bulk RCM function is applied to remove the range migration trajectory, resulting in the removal of RCM. The phase function of bulk RCMC is given by

$$H_{rcmc}(f_t, f_\tau) = \exp\left[-j \cdot \frac{4 \cdot \pi \cdot r_{ref}}{c} \cdot a(f_t) \cdot f_\tau\right]. \tag{2.12}$$

Third, range compression is performed by multiplying the signal (in the range-Doppler domain) with the range chirp function, given by

$$H_{rc}(f_t, f_\tau) = \exp\left[j \cdot \pi \cdot \frac{1}{k(f_t; r_{ref} \cdot (1 + a_{scl}(f_t)))} \cdot f_\tau^2\right]. \tag{2.13}$$

This third step results in range-compressed signals with a residual phase term, given by

$$\Delta\varphi(f_t) = 4\pi \cdot \frac{k(f_t; r_{ref}) \cdot a_{scl}(f_t) \cdot (1 + a(f_t))}{c^2 \cdot (1 + a_{scl}(f_t))} \cdot (r_0 - r_{ref})^2, \tag{2.14}$$

which can be eliminated by multiplying the signal with a phase correction function in the fourth step. The phase of phase correction is given by

$$H_{pc}(f_t) = \exp[j \cdot \Delta\varphi]. \tag{2.15}$$

Finally, the azimuth compression is performed by multiplying the signal with the azimuth chirp function in the Doppler domain, given by

$$H_{az}(f_t, \tau) = \exp\left[j \cdot \frac{4 \cdot \pi \cdot r_{0,scl}}{\lambda} \cdot (\beta(f_t) - 1)\right], \tag{2.16}$$

where $r_{0,scl}$ denotes the inversely scaled range position.

The algorithm's five major steps work together to transform the raw data to image data, where the RCM distortion is removed, resulting in a high-quality SAR image.

2.1.3 The Trade-off Between Range and Azimuth Ambiguities

Range and azimuth ambiguities are often discussed together because they are interrelated in radar system design. In a SAR system, the distance to a target is determined by the delay of the received echo. The time delay and distance are related by the following equation [54]

$$R = \frac{c \cdot \tau}{2}, \tag{2.17}$$

where c is the propagation velocity of the electromagnetic's wave and τ represents the delay of the received echo. The factor of 2 accounts for the round-trip path of the signal.

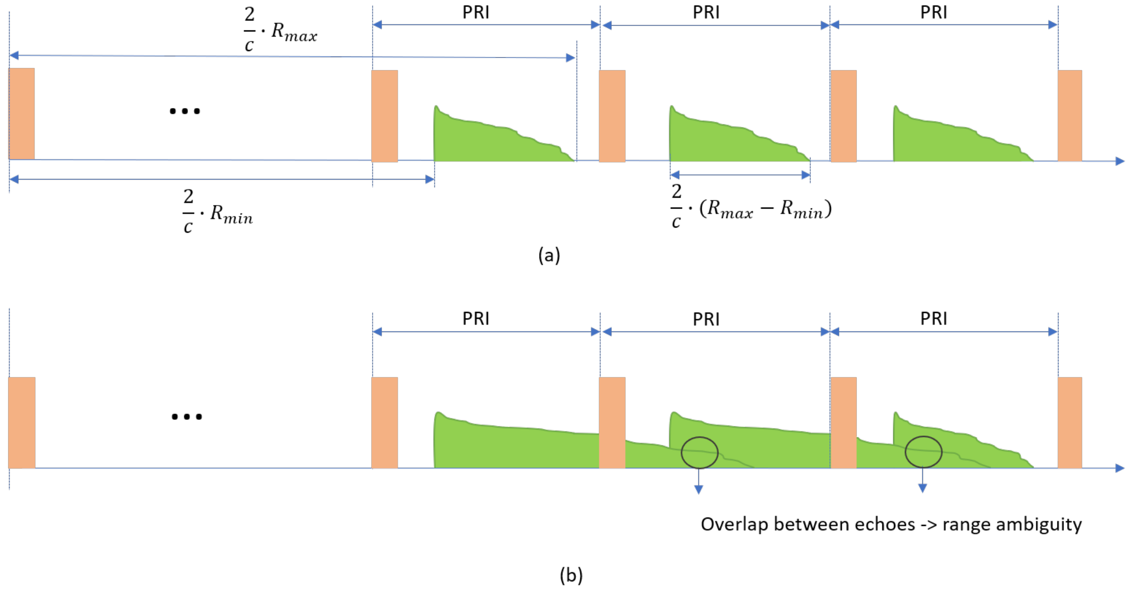

(a)

(b)

Figure 2.4: Visualization of the SAR timing through transmit pulse (brown) and return echo (green) without (a) and with (b) range ambiguities.

The time interval between transmitted pulses is referred to as the pulse repetition interval (PRI). As depicted in Figure 2.4(a), the echo from the first transmitted pulse shall be received within a certain receiving-time window. Consequently, the swath width in SAR must meet the following criterion [54]

$$R_{max} - R_{min} < c \cdot \frac{PRI}{2}, \tag{2.18}$$

where R_{max} and R_{min} denote the maximum and minimum slant range of the imaged swath, respectively. Consequently, the swath width extension the ground, by assuming flat Earth approximation, can be expressed as [54]

$$W_g < \frac{c}{2} \cdot \frac{PRI}{\sin \eta} = \frac{c}{2} \cdot \frac{1}{PRF \cdot \sin \eta}, \tag{2.19}$$

where η is the incident angle.

Receiving two, or more, simultaneous echos, indicated by the black circle illustrated in Figure 2.4(b), leads to range ambiguities, i.e., the radar is not able to determine the correct range from the echo delay. This challenge arises because the system cannot distinguish whether the received echo is associated with the first or second pulse. This phenomenon is commonly known as a range ambiguity.

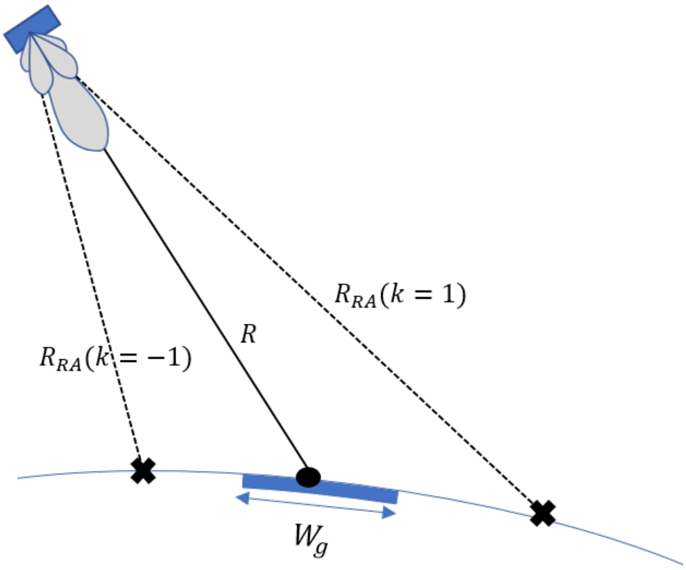

Figure 2.5: The side-looking SAR geometry illustrating the occurrence of range ambiguities. The intended target is indicated by a black dot, while the range-ambiguous targets are indicated by black crosses.

In other words, range ambiguities in SAR imaging occur when radar echoes from multiple pulses arrive at the receiver within the same PRI. Figure 2.5 illustrates the source of range ambiguities, where the echoes come not only from the intended target, but also from two range-ambiguous targets. The slant range of a range-ambiguous target is given by [54]

$$R_{RA} = R + \frac{k \cdot c \cdot PRI}{2}, \tag{2.20}$$

where R is the slant range of the intended unambiguous target, and k an integer that denotes the order of the ambiguity. The factor of $1/2$ accounts for the fact that the radar pulse must travel to the target and back to the receiver.

To circumvent range ambiguities, according to (2.18), $c \cdot PRI/2$ should exceed the intended swath width that is to be imaged. One way to achieve this is to increase the PRI. However, despite having a sufficiently long PRI, range ambiguities can occur due to the presence of sidelobes in the antenna pattern. As shown in Figure 2.5, these sidelobes illuminate the ambiguous target and can result in range ambiguities. Hence, it becomes crucial to carefully design an antenna pattern with minimal sidelobes to effectively mitigate the occurrence of range ambiguities. In a single-channel SAR system, achieving low sidelobes is typically done by designing antenna patterns (Tx and Rx) with high gain within the illuminated swath and low gain outside the swath. However, this becomes more challenging in the case of multichannel SAR systems with multiple elevation beams, as will be discussed in the next section.

In SAR imaging, as discussed in Section 2.1.1, the antenna beamwidth and the synthetic aperture's length determine the azimuth resolution. Achieving high azimuth resolution requires a larger Doppler bandwidth, as expressed in (2.4). Consequently, a larger Doppler bandwidth necessitates a higher azimuth sampling rate. In SAR, azimuth sampling is represented by the pulse repetition frequency (PRF) [9], meaning that a high PRF, i.e., low PRI as $PRF = 1/PRI$, is required when dealing with a large Doppler bandwidth, B_t. If the PRF is too low, aliasing can occur, known in SAR as azimuth ambiguities. Although there are techniques to reduce azimuth ambiguities in specific scenarios while keeping the PRF low [58], [59], [60], in general, the PRF must be high enough to prevent such ambiguities by ensuring that the Doppler shifts of the echoes from various azimuth positions do not overlap in the range-Doppler domain. This can be accomplished by raising the PRF, which reduces the time between successive radar pulses and increases the number of pulses used to create the synthetic aperture. Consequently, it is strictly required to have following condition [54]

$$PRF > B_t. \tag{2.21}$$

However, as previously noted, increasing the PRF can also result in range ambiguities, creating a fundamental trade-off between range ambiguities and azimuth ambiguities in conventional SAR systems.

2.2 Multichannel SAR Systems

In a multichannel SAR system, a channel refers to an independent pathway for transmitting/receiving radar signals. Each channel corresponds to a separate transmitter/receiver that illuminates/captures radar data. These channels can operate simultaneously. In this thesis, multichannel SAR systems specifically refer to monostatic systems that utilize multiple elevation channels for reception, allowing for multiple beams on receive [61]. In terms of system theory, such a SAR configuration would be classified as a single-input multiple-output (SIMO) system.

The most significant advantage of a multichannel SAR system is the ability to allow high azimuth resolution imaging and wide swath coverage of the target area [61].

However, multichannel SAR systems are more complex, requiring multiple channels, receivers, and signal processing units, with significantly higher data processing requirements than conventional SAR systems.

2.2.1 Signal Model

Digital beamforming (DBF) is a signal processing technique that is commonly suggested in multichannel SAR systems to form and steer a narrow-high-gain beam with low sidelobes [62], [63], [64], [65]. DBF in elevation involves the use of multiple elevation channels to receive the SAR signal. In such a multichannel SAR system, each elevation channel receives the same signal at slightly different time delay due to the different positions of the elevation apertures. These time differences are compensated for by a digital beamformer, which aligns the received signals in time and sums them together to form a single output signal.

The basic equation for digital beamforming in SAR is given by [66]

$$x(\tau) = \mathbf{w}^H(\tau)\,\mathbf{y}(\tau), \tag{2.22}$$

where x denotes an output signal; $\mathbf{y}$ the input signal vector from the multiple channels; and $\mathbf{w}$ the complex weight vector applied to each channel in the channel vector.

The flexibility to form multiple receive beams simultaneously is one of the greatest advantages of DBF on receive, and it is a major benefit of using a multichannel system over a single channel system. When multiple DBF beams are formed, equation (2.22) can be rephrased as

$$\mathbf{x}(\tau) = \mathbf{W}^H(\tau)\,\mathbf{y}(\tau), \tag{2.23}$$

where $\mathbf{x}$ denotes a set of output signals, and $\mathbf{W}$ the complex weight matrix.

In addition to digital beamforming in elevation, the SCan-On-REceive (SCORE) technique (also known as SweepSAR) [61], [67], is utilized to enhance the system's signal-to-noise ratio and reduce range ambiguities. This is achieved by steering receive beams in real-time to track the angle-of-arrival of the echoes as they move across the ground swath [68]. Figure 2.6 illustrates how the SCORE is done by applying time-variant weighting to the received echoes in each elevation channel. In a planar direct-radiating array antenna, all elevation channels are activated in order to form a narrow high-gain beam, while in an array-fed reflector antenna, only a small number of antennas are activated. During SCORE operation, the weights used to compute the beams are stored in a lookup table, and a scanning law is implemented by rapidly switching the weights based on the geometry. To ensure that the receiving beam center precisely points to the direction of the central position, the weighting vector and coefficient must be designed based on the central position of the pulse

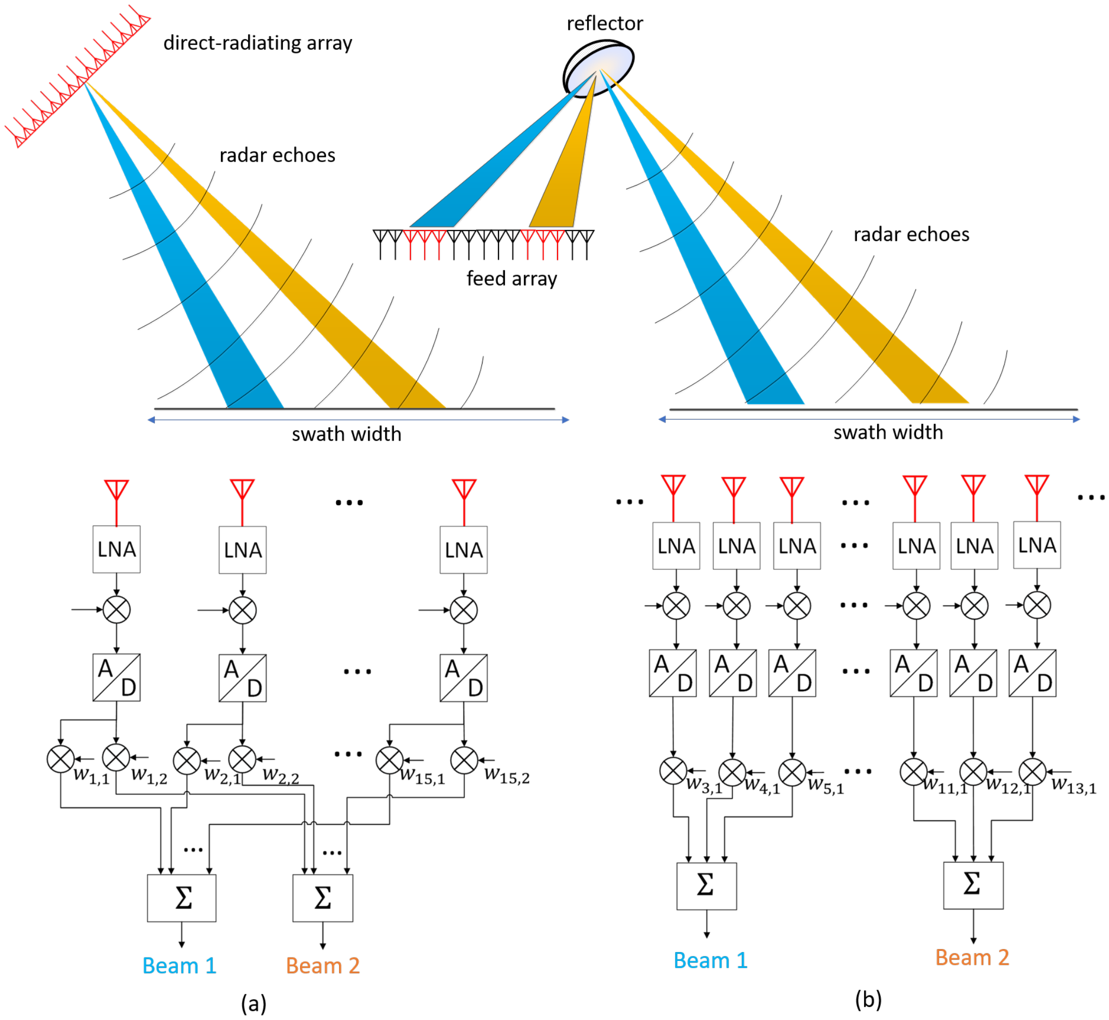

Figure 2.6: The illustration shows two simultaneous SCORE beams in (a) a planar direct-radiating array antenna and (b) an array-fed reflector antenna. The top figures display the SCORE beams, while the bottom figures show the schematic of DBF on receive. The activated feed elements are shown in red, while the non-activated elements are shown in black. The weighting elements are denoted by $\mathbf{w}_{ij}$, where i and j refer to the indices of active elements and formed beams, respectively.

extension on the ground. As the pulse center changes over time, the weighting vector also becomes time-variant. The weighting coefficient for the k-th channel can be determined using [69]

$$w_k(\tau) = \exp\left\{ j \cdot 2 \cdot \pi \cdot \frac{(k-1) \cdot d}{\lambda} \cdot \sin\left[\theta(\tau)\right] \right\}, \tag{2.24}$$

where $\theta(\tau)$ corresponds to the off-boresight angle associated with the corresponding pulse central position; k the activated channel; and d the spacing between the antenna elements.

The use of multiple elevation receive beams allows for a high-resolution wide-swath (HRWS) SAR system, but the issue of range ambiguities still persists, particularly due to the considerable level of sidelobes at the location of range ambiguities. Unlike in a conventional SAR system, where only a single Rx beam is used, the range ambiguities cannot be attenuated by the Tx pattern in a wide-swath SAR with multiple elevation beams. Figure 2.7 shows a comparison of the antenna pattern between a conventional (single-channel) SAR system and a multichannel SAR with multiple elevation Rx beams. In a conventional SAR system, the sidelobe level of the Rx beam is attenuated by a the narrow Tx beam. However, in a SAR with multiple elevation Rx beams, the sidelobe of the Rx beam is multiplied by the high-value of a wide Tx beam, resulting in a higher range ambiguity value.

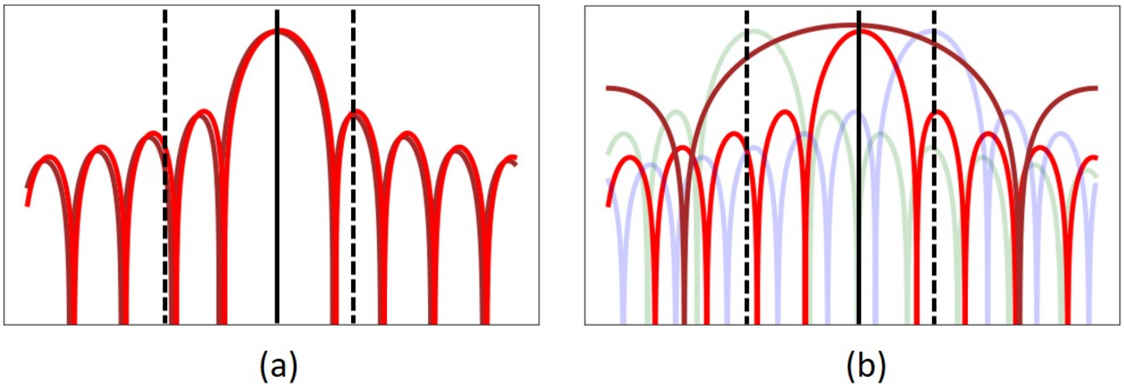

Figure 2.7: The figure provides a simplified illustration of the Tx and Rx elevation beams in two different SAR systems. In the conventional SAR system shown in (a), there is only one Tx beam (brown) and one Rx beam (red). In contrast, the multiple elevation beams SAR system shown in (b) has one Tx beam (brown) and multiple Rx beams (green, red, and blue), with the red Rx beam highlighted. The position of the useful signal of the red Rx beam and its corresponding range ambiguity signals are indicated by the solid and dotted lines, respectively. The x and y axis indicate elevation angle and antenna gain, respectively.

In order to achieve the best SAR image quality, indicated by high SNR and minimum range ambiguity disturbance, a variety of beamforming techniques are employed. Among these techniques, the minimum variance distortionless response (MVDR) [70] approach is a well-established method based on Capon's method [71]. The goal of this approach is to minimize the variance of the beamformer output. If the noise and the underlying desired signal are uncorrelated, as is typically the case, then the variance of the captured signals is the sum of the variances of the desired signal and the noise. Hence, the MVDR solution seeks to minimize this sum, thereby mitigating the effect of the noise. The MVDR approach can be mathematically expressed as follows

$$\begin{aligned} &\text{minimize } \mathbf{w}^H \mathbf{R}_v \mathbf{w}, \\ &\text{subject to } \mathbf{g}^H(\vartheta_0)\ \mathbf{w} = 1, \end{aligned} \tag{2.25}$$

where $\mathbf{w}$ denotes the complex weighting vector; $\mathbf{g}(\vartheta_0)$ the array steering vectors to the angle of interest ϑ_0; and $\mathbf{R}_v$ the channel covariance matrix of thermal noise, given by [70]

$$\mathbf{R}_v = E\{\mathbf{v}\mathbf{v}^H\}, \tag{2.26}$$

where the vector $\mathbf{v}$ represents the stationary noise from the different channels. The equation (2.25) is mainlobe-constrained, causing a beam pointing at ϑ_0. The solution is in closed form given by

$$\mathbf{w} = \frac{\mathbf{R}_v^{-1}\mathbf{g}(\vartheta_0)}{\mathbf{g}^H(\vartheta_0)\mathbf{R}_v^{-1}\mathbf{g}(\vartheta_0)} \tag{2.27}$$

The MVDR approach can be considered as a spatial matched filter that optimizes the SNR. However, to address the issue of range ambiguities, the MVDR technique should be modified to minimize the sidelobe level in the direction of range ambiguities. This modification of the MVDR approach is known as sidelobe-constrained MVDR [72]

$$\begin{aligned} &\text{minimize } \mathbf{w}^H \mathbf{R}_v \mathbf{w}, \\ &\text{subject to } \mathbf{g}^H(\vartheta_0)\mathbf{w} = 1, \\ &\qquad\qquad \left|\mathbf{g}^H(\vartheta_k)\mathbf{w}\right|^2 \leq \eta_{SL}, \vartheta_k \in \left[\vartheta_1\ \vartheta_2\ ...\right]. \end{aligned} \tag{2.28}$$

Unlike equation (2.25), equation (2.28) imposes an additional sidelobe constraint that results in small beam values below η_{SL} at ϑ_k, which corresponds to the angles where the most dominant range ambiguities are expected to be located.

Another beamformer that is similar to a sidelobe-constrained MVDR is the linear constraint minimum variance (LCMV) beamformer [70], which focuses on nullifying the sidelobe level associated with range ambiguities. As compared to the sidelobe-constrained MVDR, LCMV beamforming only contains sidelobe constraint, which nullifies the sidelobes across all angles where range ambiguities occur. This method optimizes sensitivity in the direction of interest while simultaneously suppressing range ambiguities from certain other directions, and is described in [70]. The optimization can be formulated as

$$\begin{aligned} &\text{minimize } \mathbf{w}^H \mathbf{R}_v \mathbf{w}, \\ &\text{subject to } \mathbf{G}^H \mathbf{w} = \mathbf{c}, \end{aligned} \tag{2.29}$$

with the minimization function being identical to the one of the MVDR beamformer. Here, the steering matrix $\mathbf{G}$ is given by

$$\mathbf{G} = \left[\mathbf{g}(\vartheta_1) \quad \mathbf{g}(\vartheta_2) \ \ \ldots \ \ \mathbf{g}(\vartheta_{N_{dir}})\right] \in \mathbb{C}^{N_{act} \times N_{dir}}, \tag{2.30}$$

The steering matrix $\mathbf{G}$ consists of the steering vectors with N_{act} active antenna elements for N_{dir} different directions. The constraint vector $\mathbf{c}$ can be in principle be chosen freely. For example, a meaningful constraint vector could take the form

$$\mathbf{c} = \left[1\,0 \ldots 0\right]^T \in \mathbb{C}^{N_{dir}}, \tag{2.31}$$

where the '1' corresponds to the direction of the signal of interest and zeros are placed in directions to be suppressed. Accordingly, the closed-form solution is given by

$$\mathbf{w} = \frac{\mathbf{R}_v^{-1}\mathbf{G}}{\mathbf{G}^H\mathbf{R}_v^{-1}\mathbf{G}}\mathbf{c}. \tag{2.32}$$

The LCMV beamformer is particularly suited for scenarios where range ambiguities are present since it is designed to suppress them from specific directions. Additionally, it can handle multiple constraints, which is an advantage over the MVDR beamformer that is restricted to a single constraint. On the other hand, the LCMV beamformer is more sensitive, i.e, less robust, to array imperfections like calibration errors and mutual coupling than the MVDR beamformer [65].

The three previously discussed techniques; the mainlobe-constrained MVDR beamformer (2.25), the sidelobe-constrained MVDR beamformer (2.28), and the LCMV beamformer (2.29), share a common requirement of accurate knowledge of the complex antenna pattern in order to have accurate complex weighting vectors, as seen in (2.27) and (2.32). Failure to obtain this information accurately can result in spatial mismatch, leading to a loss in SNR for the mainlobe-constrained MVDR beamformer, and an increase of the range ambiguities for both the sidelobe-constrained MVDR and LCMV beamformers. The challenges associated with obtaining accurate information on the complex antenna pattern will be discussed in the next section.

2.2.2 The Challenge of Pattern Mismatch

In this section, challenges associated with obtaining accurate information about complex antenna patterns are discussed, which makes it difficult to apply deterministic techniques like the DBF approach (such as MVDR and LCMV) to suppress range ambiguities.

Digital Channel Errors

Digital channel errors refer to the discrepancies or imperfections that may occur in the signal processing chain of a SAR system, which is particularly pronounced due to the utilization of multiple onboard digital channels and extensive processing in advanced SAR systems. These errors can arise due to various reasons, such as quantization errors, non-idealities in the analog-to-digital conversion process, and many more. The error model that is widely accepted is described as [73], [74]

$$e_i = (1 + \xi_i) \cdot e^{j\zeta_i}, \tag{2.33}$$

where ξ and ζ denote magnitude and phase errors, respectively, and the index i refers to the channel.

A received DBF signal, in the presence of errors that are introduced by multiplicative terms, can be expressed as [72]

$$x(\tau) = \sum_i \left[w_{RX,i}(\tau) \cdot e_i \cdot \sum_k y_{i,k}(\tau) \right], \tag{2.34}$$

where index i refers to the Rx channel; $w_{RX,i}$ to the complex-valued weight on the Rx channel i; and y to the received signal. A non-zero index k refers to a range-ambiguous signal, superimposed on the useful signal ($k = 0$). For simplicity, the additive white Gaussian noise associated with the channel is omitted.

During the investigation in [72], the influence of errors was analyzed for two types of antennas; planar phased array and array-fed reflector antennas; and using the MVDR technique for DBF processing. The investigation shows that the presence of digital channel errors can degrade the range ambiguity suppression performance by up to 10 dB for array-fed reflector antennas and up to 30 dB for planar antennas. The results show that the planar antenna is more susceptible to errors compared to the reflector antenna. However, it should be noted that the investigation only considered the following aspects: (i) one DBF signal (ii) without the use of a SCORE operation (iii) the errors are included only in the received channel and not in the transmit channel. Consequently, it was concluded that the degradation in the planar antenna was more severe due to the higher number of activated RX channels as compared to the reflector antenna.

When multiple DBF signals are taken into account, the number of activated Rx channels will eventually increase for the case of reflector antennas. Additionally, the SCORE operation will also result in more channels being activated as the Rx beams sweep the received echo. Furthermore, in the case of reflector antennas, all Tx channels are activated in order to transmit a wide beam, and for planar antennas, the phase-only tapering beam [75] also requires all Tx channels to be activated. Therefore, one could expect an ultimate deterioration of the range ambiguity performance in both planar and array-fed reflector systems when all Tx and Rx channels are activated.

Pattern Calibration Uncertainty

The antenna pattern calibration uncertainty is one of the error contributors in the SAR system [76]. This uncertainty is particularly severe for multichannel SAR antennas with large dimensions, such as those operating at P and L frequency bands; a system like Tandem-L has an antenna diameter of 15 m [40]. The near-field method is traditionally used for antenna pattern measurement in ground tests, but even with these measurements, the working state and environment of the satellite in orbit are different, leading to antenna pattern differences [77].

Pattern calibration uncertainty arises as the combined effect of measurement and residual calibration errors. The measured antenna pattern deviates from the ideal value due to errors in magnitude and phase. In particular, the DBF SAR operating in SCORE is vulnerable to pattern errors because the combination is done on-board the satellite and cannot be corrected later during on-ground processing. To overcome this, on-board calibration which is under investigation in [78] becomes the solution. Nevertheless, the investigation in [79] shows that accurate knowledge of the patterns is crucial, as pattern calibration uncertainty has the potential to severely degrade the expected performance.

Topographic Errors

To utilize the DBF technique effectively, it is necessary to have a precise information of the relationship between time of arrival (ToA) and direction of arrival (DoA) in order to steer the beam towards a specific direction and suppress the radar echoes in the direction of ambiguity. However, due to the presence of topography, it is difficult to obtain an accurate ToA and DoA relationship. Figure 2.8 illustrates how the actual ToA/DoA model can be considerably different from the assumed one.

The presence of topographic variations within the swath can cause mispointing. While the discussion of mispointing generally concerns the SCORE pattern loss [80], [81] - i.e., measure of the antenna gain loss due to topographic height such as mountains and relief - Figure 2.9 provides a simplified illustration of how mispointing occurs with regard to range ambiguities, such as when using the LCMV beamformer that positions nulls in the direction of the range ambiguities. This effect is more significant for range ambiguities than for other factors. For instance, an example

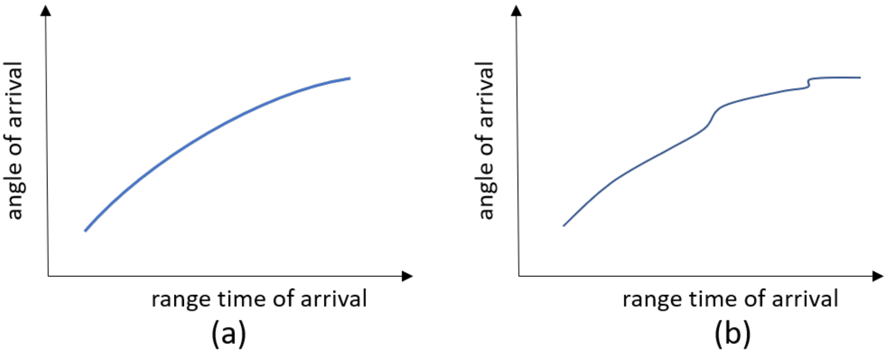

Figure 2.8: The relationship between time of arrival (ToA) and direction of arrival (DoA). In (a), the typical assumption used during processing is shown. In (b), unmodeled terrain height can lead in reality to deviations from this assumption.

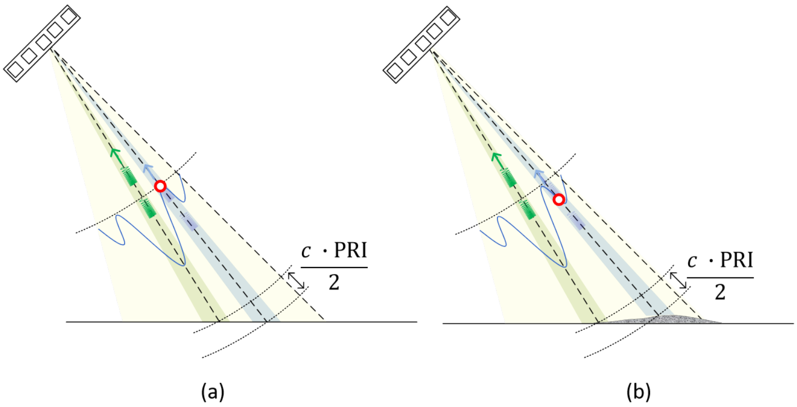

Figure 2.9: The impact of topography on mispointing in range ambiguity null-steering, as indicated by the red circle. In (a), when using DBF, the null is positioned in the direction of the range ambiguity. In (b), topographic distortion causes mispointing of the null.

in [46] shows that a height offset of 1.5 km raises the ambiguities to an unacceptable level of -17 dB.

It is important to note that even if null-steering takes into account the topography at the zero-Doppler position, there may still be topographic variations within the azimuth antenna footprint that cannot be accounted for through null-steering in elevation. Consequently, when accounting for the full Doppler spectrum, the overall effect of mispointing can become even more severe.

Deformation of the Reflector

The array-fed reflector antenna system is a promising antenna system for future HRWS SAR systems [39], owing to its ability to generate a narrow-high-gain Rx beam. This makes it more feasible to generate multiple Rx beams in elevation as compared to a planar array SAR system. However, achieving an accurate antenna pattern for high-gain low-sidelobe DBF signals poses some significant challenges in the reflector antenna system. One of them is the deformation of the antenna caused by thermoelastic instability as shown in Figure 2.10.

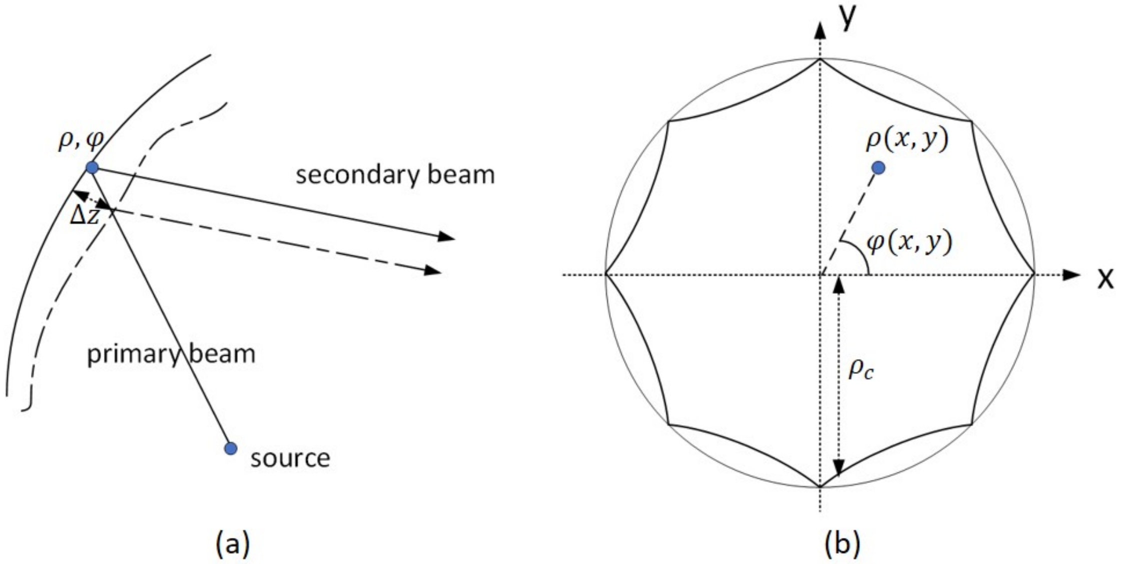

Figure 2.10: Illustration of a deformed reflector antenna in two views: (a) a side-looking view [82] showing both the undistorted and distorted beam using solid and dashed lines, respectively, and (b) a surface projection in the xy plane [83].

There are different models of deformations described in [83], [84]

$$\Delta z = A_d \sin\left(N_\rho \cdot \frac{\pi \cdot \rho}{2 \cdot \rho_c}\right) \cos\left(N_\varphi \cdot \frac{\varphi}{2}\right), \tag{2.35}$$

$$\Delta z = A_d \sin\left(N_\rho \cdot \frac{\pi \cdot \rho}{2 \cdot \rho_c}\right) \sin\left(N_\varphi \cdot \frac{\varphi}{2}\right), \tag{2.36}$$

where they are modeled as a periodic function dependent on several parameters; ρ_c denotes the radius of reflector; ρ the radius of deformed location; φ the angle of deformed location; N_ρ the number of quarter period deformations w.r.t. radius ρ; N_φ the number of half period deformations w.r.t. angle φ; A_d the arbitrary value of amplitude of deformation. The investigation in [83] shows that before DBF, the radiation pattern experiences (i) a drop in the main lobe (ii) a change in beamwidth, and (iii) an increase in the sidelobes. After DBF using MVDR, there is a stronger effect in gain and beamwidth, while the peak-sidelobe ratio (PSLR) is less affected.

However, the investigation in [83] only covers the main beam angle and does not consider range ambiguities. Accordingly, it is indicated in [83] that the impact on the sidelobes of the antenna pattern is more severe. Thus, it is clear that the shape of the radiation pattern and DBF pattern undergo significant changes, which suggest an increase in the range-ambiguity-to-signal ratio.

While the deformation models in (2.35) and (2.36) depend on both radius and angle, there also exist other models [83], [85], [82]

$$\Delta z = A_d \cdot \cos\left(N_\rho \cdot \frac{\pi \cdot \rho}{2 \cdot \rho_c}\right), \tag{2.37}$$

$$\Delta z = 0.05 \cdot \lambda \cdot \cos(N_\varphi \cdot \varphi). \tag{2.38}$$

The model in (2.37) only depends on radius, referred to as cosinusoidal in radius and invariant with angle [83], while the model in (2.38) is independent of the radius and affected only by the angle φ and wavelength λ, referred to as azimuthally-varying cosine deformation [85], [82]. Accordingly, the investigation in [85], [82] shows that when $N_\varphi = 5$, the sidelobe level in the radiation pattern significantly increases, while the main lobe is less affected, leading to an increase in range-ambiguity-to-signal ratio.

To sum up, the existing literature provides compelling evidence that antenna deformation can potentially lead to range ambiguity issues.

Remark on Pattern Mismatches

The previously discussed challenges are classified as non-deterministic errors. When these errors are considered together (i) it becomes apparent that obtaining an accurate antenna pattern is an extremely challenging task, (ii) range ambiguities are a crucial performance metric that are negatively impacted by antenna pattern inaccuracies. Additionally, deterministic errors such as pulse extension loss [86], [87] and pattern mismatches, caused by a limited set of weights over range and pulse bandwidth [79], shall be taken into account. While including both non-deterministic and deterministic errors, the presence of range ambiguities is expected to result in a decline in performance.

3 Blind Source Separation in SAR

This chapter provides an overview of the relation between range ambiguity suppression in multichannel SAR systems and a phenomenon known as the cocktail party problem. It also introduces the blind source separation (BSS) technique, a classical method developed in response to cocktail party problem, which is the central focus of this thesis. Section 3.1 presents a novel derivation of range ambiguity suppression in multichannel SAR in terms of cocktail party condition, followed by the introduction of BSS and its application to SAR signals in Section 3.2. Section 3.3 delves into the challenges encountered when implementing BSS for SAR signals, which are demonstrated through a numerical analysis considering factors such as the number of sources, the presence of out-of-swath ambiguous signals, and the value of the mixing matrix. Finally, Section 3.4 provides concluding remarks. Part of the material in this chapter has been published in [47], [49].

3.1 Cocktail Party Formulation in Multichannel SAR

3.1.1 Cocktail Party Problem

The cocktail party problem is a classic problem which occurs when multiple people talk at once during a social gathering, resulting in a mixture of different voices that each individual must distinguish [88], [89]. This phenomenon has been modeled in [90] as

$$\begin{gathered}\mathbf{x}(t) = \mathbf{A}\mathbf{s}(t),\\ \begin{bmatrix} x_1(t) \\ \vdots \\ x_M(t) \end{bmatrix} = \begin{bmatrix} a_{1,1} & \cdots & a_{1,N} \\ \vdots & \ddots & \vdots \\ a_{M,1} & \cdots & a_{M,N} \end{bmatrix} \begin{bmatrix} s_1(t) \\ \vdots \\ s_N(t) \end{bmatrix},\end{gathered} \tag{3.1}$$

where M is the number of listeners; N the number of people talking; $\mathbf{A}$ is the mixing matrix; $\mathbf{x}$ the vector of heard mixed voices; $\mathbf{s}$ the vector of simultaneously emitted voices. The so called "cocktail party problem" denotes then the task of extracting the useful source signals, i.e., the emitted voices, $\mathbf{s}$, from the received voices, $\mathbf{x}$, without knowing $\mathbf{A}$ (see Figure 3.1).

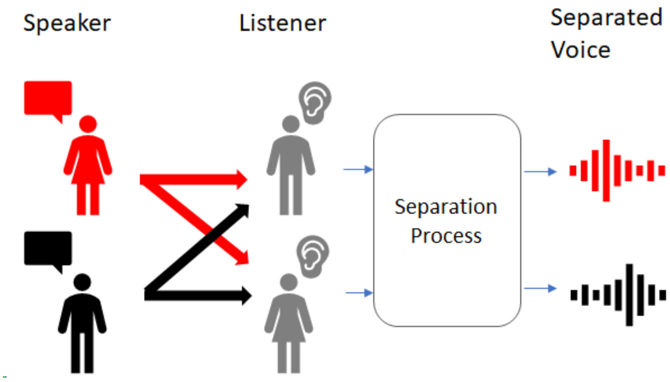

Figure 3.1: Illustration of the cocktail party problem.

It is worth to note that, when $M = N$, each emitted voice represents the useful signal for one listener and a disturbance for all other listeners. This property of the source signals is denoted as reciprocity. As shown in the next sections, it is of key importance in the multichannel SAR context.

Finally, it is important to mention that the cocktail party model in (3.1) tries to recover both the unknown signals $\mathbf{s}$ and the unknown mixing matrix $\mathbf{A}$ and relies solely on the knowledge of $\mathbf{x}$. Therefore, the components' magnitudes of either $\mathbf{A}$ or $\mathbf{s}$ cannot be uniquely determined, resulting in scaling uncertainties. Furthermore, the columns' order of $\mathbf{A}$ can be arranged arbitrarily, as changing the order of columns in $\mathbf{A}$ leads to equally valid source estimates, resulting in permutation uncertainties. These two uncertainties necessitate an additional constraint within the equation to attain a unique solution. Such a constraint is available in the case of SAR, as derived in the following sections.

3.1.2 Cocktail Party Problem in Multichannel SAR Systems

One of the crucial topics in this thesis is the close relation of the cocktail party problem with the range ambiguity suppression in multichannel SAR systems. This relation is established by the presence of multiple receivers for the radar echoes, which is in contrast to conventional SAR systems that rely on a single channel for echo reception.

Figure 3.2 depicts the operational mode of a multichannel SAR where a wide Tx beam is used to illuminate multiple subswaths that are simultaneously imaged by multiple Rx beams. Due to the high PRF relative to the overall swath extension,

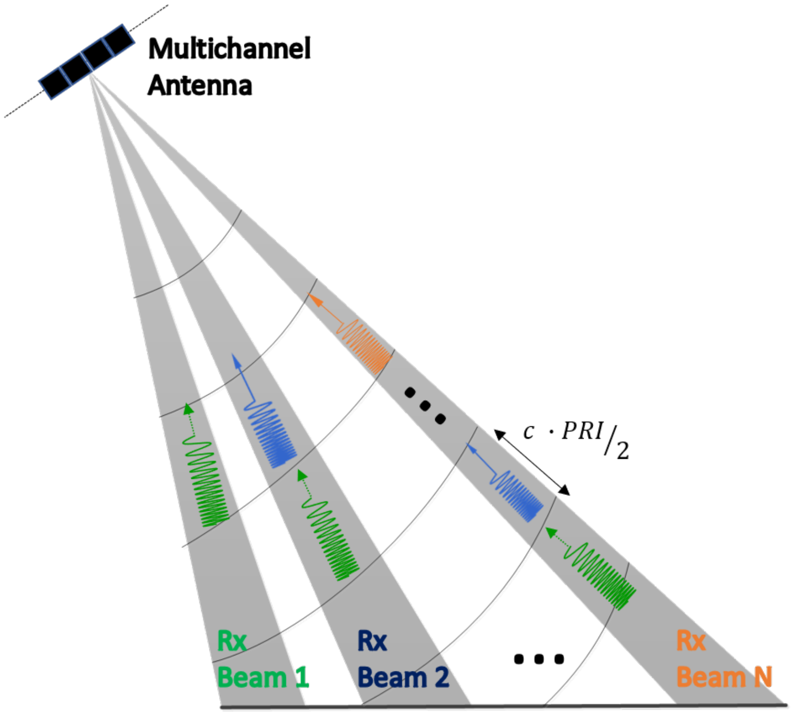

Figure 3.2: Multichannel SAR system that utilizes multiple elevation Rx beams. The system employs a wide Tx beam to cover a wide swath, while N Rx beams are formed to map N-subswaths.

strong range-ambiguous echoes are received from the imaged swath. Specifically, the received signal can be expressed as:

$$x_i = s_i + \sum_k s_{i,RA}(k), \tag{3.2}$$

where x_i denotes the signal received from the i-th Rx beam; s_i and s_{RA} the corresponding useful signal and range ambiguous signals, respectively, which are simultaneously received; and k the integer number indicating the order of the ambiguity.

The slant range of the range ambiguous target is given by

$$R_{RA} = R_0 + D_r(k), \tag{3.3}$$

where R_0 is the slant range of the useful target, and the ambiguity distance, i.e., the slant range displacement between useful signal and range ambiguous signal, is given by

$$D_r(k) = \frac{k \cdot c \cdot PRI}{2}. \tag{3.4}$$

It is worth to remark that the strong ambiguities are expected to originate exclusively from within the imaged swath. However, there are also other ambiguities that arise outside the imaged swath, known as out-of-swath ambiguities, which are assumed to be effectively suppressed by the Tx pattern [1]. As a consequence, as first mentioned in [46], a reciprocity property exists between the useful signals and the ambiguity signals. Accordingly, the ambiguity of a useful signal is always represented by a scaled version of another useful signal, where the scaling factor is given by a complex number.

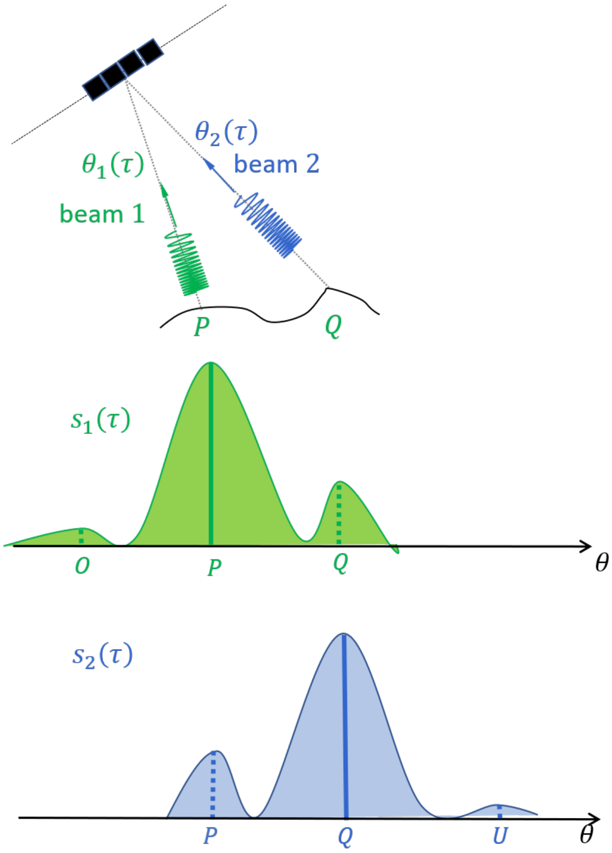

Figure 3.3: Zero-Doppler geometry showing two subswaths imaged simultaneously by two beams. In beam 1, P returns the useful signal and Q the strong ambiguity; in beam 2, Q returns the useful signal and P the strong ambiguity.

Regarding the reciprocity identification within multichannel SAR systems, let us consider the scenario in Figure 3.3, characterized by two Rx beams and four point

---

[1] The nadir echo, although technically considered a out-of-swath ambiguity as it originates from outside the imaged swath, can still have a significant magnitude comparable to or even stronger than strong ambiguities due to the specular reflection phenomenon. Nadir echoes can be effectively suppressed using techniques like those proposed in [91] and [92].

targets (O, P, Q, and U), separated by the distance of ambiguity. Based on (3.2), the two Rx signals can be expressed as:

$$\begin{aligned}
x_1(\tau, f_t) &= s_1(\tau, f_t) + \sum_k s_{1,RA}(\tau, f_t, k), \\
&= \sigma_{P(f_t)} \cdot g_1(\tau, f_t, P(f_t)) \cdot \mathrm{rect}\left(\tau - \frac{2 \cdot R_P(f_t)}{c}\right) \\
&\cdot \exp\left(-j \cdot \frac{4 \cdot \pi}{\lambda} \cdot R_P(f_t)\right) \cdot \exp\left(j \cdot \pi \cdot k_r \left[\tau - \frac{2 \cdot R_P(f_t)}{c}\right]^2\right) \\
&+ \sigma_{Q(f_t)} \cdot g_1(\tau, f_t, Q(f_t)) \cdot \mathrm{rect}\left(\tau - \frac{2 \cdot R_Q(f_t)}{c}\right) \\
&\cdot \exp\left(-j \cdot \frac{4 \cdot \pi}{\lambda} \cdot R_Q(f_t)\right) \cdot \exp\left(j \cdot \pi \cdot k_r \left[\tau - \frac{2 \cdot R_Q(f_t)}{c}\right]^2\right) \\
&+ \sigma_{O(f_t)} \cdot g_1(\tau, f_t, O(f_t)) \cdot \mathrm{rect}\left(\tau - \frac{2 \cdot R_O(f_t)}{c}\right) \\
&\cdot \exp\left(-j \cdot \frac{4 \cdot \pi}{\lambda} \cdot R_O(f_t)\right) \cdot \exp\left(j \cdot \pi \cdot k_r \left[\tau - \frac{2 \cdot R_O(f_t)}{c}\right]^2\right),
\end{aligned} \tag{3.5}$$

$$\begin{aligned}
x_2(\tau, f_t) &= s_2(\tau, f_t) + \sum_k s_{2,RA}(\tau, f_t, k), \\
&= \sigma_{Q(f_t)} \cdot g_2(\tau, f_t, Q(f_t)) \cdot \mathrm{rect}\left(\tau - \frac{2 \cdot R_Q(f_t)}{c}\right) \\
&\cdot \exp\left(-j \cdot \frac{4 \cdot \pi}{\lambda} \cdot R_Q(f_t)\right) \cdot \exp\left(j \cdot \pi \cdot k_r \left[\tau - \frac{2 \cdot R_Q(f_t)}{c}\right]^2\right) \\
&+ \sigma_{P(f_t)} \cdot g_2(\tau, f_t, P(f_t)) \cdot \mathrm{rect}\left(\tau - \frac{2 \cdot R_P(f_t)}{c}\right) \\
&\cdot \exp\left(-j \cdot \frac{4 \cdot \pi}{\lambda} \cdot R_P(f_t)\right) \cdot \exp\left(j \cdot \pi \cdot k_r \left[\tau - \frac{2 \cdot R_P(f_t)}{c}\right]^2\right) \\
&+ \sigma_{U(f_t)} \cdot g_2(\tau, f_t, U(f_t)) \cdot \mathrm{rect}\left(\tau - \frac{2 \cdot R_U(f_t)}{c}\right) \\
&\cdot \exp\left(-j \cdot \frac{4 \cdot \pi}{\lambda} \cdot R_U(f_t)\right) \cdot \exp\left(j \cdot \pi \cdot k_r \left[\tau - \frac{2 \cdot R_U(f_t)}{c}\right]^2\right),
\end{aligned} \tag{3.6}$$

where $g(\tau, f_t, Y(f_t))$ denotes the two-way antenna pattern, weighting the signal received from Doppler-dependent target $Y(f_t), Y \in \{O, P, Q, U\}$ [2]; σ_Y the complex

---

[2] In the following, for simplicity, it is assumed that the signal, received from a point target, is weighted by the pattern value at the target location, i.e., the SCORE beam steering during the pulse duration, particularly for long pulses, is neglected [87].

amplitude of the echo received from Y; R_Y the distance between the receiver and Y; and k_r and λ the transmitted chirp rate and the radar wavelength, respectively. It is noted that in the raw data, the Doppler frequency band is determined by the illumination time. However, the azimuth envelope is omitted in the equation for a simpler representation.

It is important to note that the derivation in (3.5) and (3.6) can be generalized to distributed targets. Specifically, while in the point target case $Y \in \{O, P, Q, U\}$ represent individual point targets, in the distributed target case $Y \in \{O, P, Q, U\}$ represent range bins. In the distributed target case, the received signal at a range bin consists of multiple scattering points. Furthermore, the target's dependency on Doppler, $Y(f_t)$, is due to the range cell migration (RCM) effect, which leads to different target's configuration within the same range bin but at different Doppler locations. This will be explained in detail in Section 4.2.1 (when discussing Figure 4.3).

The expression of the two-way antenna pattern, g, presented here is kept general. For specific types of antenna systems, such as a planar array antenna system, the antenna pattern g can be elaborated further by factoring it into azimuth and elevation antenna patterns denoted by

$$g = g_t \cdot g_\tau, \tag{3.7}$$

where g_t and g_τ denote azimuth and elevation antenna pattern, respectively.

The strong ambiguity signal, s_{SA}, comes from Q in (3.5), or P in (3.6); the out-of-swath ambiguity, s_{WA}, comes from O and U. It is then useful to compare the strong ambiguity, $s_{1,SA}$, in (3.5) to the useful signal, s_2 in (3.6):

$$\begin{aligned} s_{1,SA}(\tau, f_t) = \sigma_{Q(f_t)} \cdot g_1(\tau, f_t, Q(f_t)) \cdot \mathrm{rect}\left(\tau - \frac{2 \cdot R_Q(f_t)}{c}\right) \\ \cdot \exp\left(-j \cdot \frac{4 \cdot \pi}{\lambda} \cdot R_Q(f_t)\right) \cdot \exp\left(j \cdot \pi \cdot k_r \left[\tau - \frac{2 \cdot R_Q(f_t)}{c}\right]^2\right), \end{aligned} \tag{3.8}$$

$$\begin{aligned} s_2(\tau, f_t) = \sigma_{Q(f_t)} \cdot g_2(\tau, f_t, Q(f_t)) \cdot \mathrm{rect}\left(\tau - \frac{2 \cdot R_Q(f_t)}{c}\right) \\ \cdot \exp\left(-j \cdot \frac{4 \cdot \pi}{\lambda} \cdot R_Q(f_t)\right) \cdot \exp\left(j \cdot \pi \cdot k_r \left[\tau - \frac{2 \cdot R_Q(f_t)}{c}\right]^2\right). \end{aligned} \tag{3.9}$$

From (3.8) and (3.9), it can be seen that the two signals differ only by a complex constant, given by the relative antenna pattern level of g_1 and g_2 at the location Q.

This shows that the range ambiguity level is solely determined by the ratio between the sidelobe and mainlobe of the antenna patterns:

$$\begin{aligned} a_{12}(\tau, f_t) &= \frac{s_{1,SA}(\tau, f_t)}{s_2(\tau, f_t)}, \\ &= \frac{g_1(\tau, f_t, Q(f_t))}{g_2(\tau, f_t, Q(f_t))}, \end{aligned} \tag{3.10}$$

$$\begin{aligned} a_{21}(\tau, f_t) &= \frac{s_{2,SA}(\tau, f_t)}{s_1(\tau, f_t)}, \\ &= \frac{g_2(\tau, f_t, P(f_t))}{g_1(\tau, f_t, P(f_t))}, \end{aligned} \tag{3.11}$$

where a_{12} is the mixing ratio between the strong ambiguity signal $s_{1,SA}$ and the useful signal s_2, and a_{21} is the mixing ratio between the strong ambiguity signal $s_{2,SA}$ and the useful signal s_1.

Accordingly, (3.5) and (3.6) can be rewritten as follows:

$$\begin{aligned} x_1(\tau, f_t) = s_1(\tau, f_t) &+ a_{12}(\tau, f_t) \cdot s_2(\tau, f_t) \\ &+ s_{1,WA}(\tau, f_t), \end{aligned} \tag{3.12}$$

$$\begin{aligned} x_2(\tau, f_t) = s_2(\tau, f_t) &+ a_{21}(\tau, f_t) \cdot s_1(\tau, f_t) \\ &+ s_{2,WA}(\tau, f_t). \end{aligned} \tag{3.13}$$

Based on (3.5) to (3.13), the general case where N elevation Rx beams map N subswaths can be written as

$$\begin{gathered} \mathbf{x}(\tau, f_t) = \mathbf{A}(\tau, f_t)\mathbf{s}(\tau, f_t) + \mathbf{s}_{WA}(\tau, f_t) + \mathbf{n}, \\ \begin{bmatrix} x_1(\tau, f_t) \\ \vdots \\ x_N(\tau, f_t) \end{bmatrix} = \begin{bmatrix} 1 & \cdots & a_{1,N}(\tau, f_t) \\ \vdots & \ddots & \vdots \\ a_{N,1}(\tau, f_t) & \cdots & 1 \end{bmatrix} \begin{bmatrix} s_1(\tau, f_t) \\ \vdots \\ s_N(\tau, f_t) \end{bmatrix} + \begin{bmatrix} s_{1,WA}(\tau, f_t) \\ \vdots \\ s_{N,WA}(\tau, f_t) \end{bmatrix} + \begin{bmatrix} n_1 \\ \vdots \\ n_N \end{bmatrix}. \end{gathered} \tag{3.14}$$

Here, $\mathbf{n}$ accounts for additive Gaussian noise.

It is important to note that the received SAR signals, $\mathbf{x}$, the useful signals, $\mathbf{s}$, and the mixing matrix, $\mathbf{A}$, depend on range-time, τ, and Doppler frequency, f_t. In particular, $\mathbf{A}$ represents the relative value of the sidelobe to the mainlobe of the two-way pattern, as written in (3.10) and (3.11). Accordingly, the diagonal elements, which correspond to the useful signal, are unitary; while the off-diagonal elements, which correspond to the range ambiguities, are complex coefficients, with amplitude lower than 1.

The dependence of $\mathbf{A}$ on τ and f_t indicates that the cocktail party problem in a multichannel SAR system is more complicated than in the classical cocktail party problem (as described in Section 3.1.1). This complexity arises from the fact that the mixing characteristics between the useful signals keep changing for different τ and f_t, which means that the values are τ- and f_t-dependent. Depending on the type of antenna used, the off-diagonal values of $\mathbf{A}$ might have a strong variation versus τ and a moderate variation versus f_t, since the useful and ambiguous signal have a large angular separation in the range direction but are both located around zero-Doppler.

With reference to (3.14), the problem to be solved in the multichannel SAR context is to suppress the range ambiguities by extracting N useful signals, $\mathbf{s}$, from N received signals and mixed signals, $\mathbf{x}$. The similarity with the cocktail party problem, described in Section 3.1.1, is evident. In particular, also in the SAR case, the reciprocity property applies, and the mixing matrix is unknown. The main differences regard: (i) the presence of the out-of-swath ambiguous signals, $\mathbf{s}_{WA}$, in the SAR signal; (ii) the presence of the Gaussian noise, $\mathbf{n}$, outside the mixing process; (iii) the dependence of the SAR mixing matrix and signals on the range time and Doppler frequency.

While the mixing matrix, which is analytically derived from the antenna pattern, generally dependent on range time and Doppler, the extent of this dependence varies based on SAR systems and their operational mode. Furthermore, different characteristics of the mixing matrix lead to specific problems: a mixing matrix that is range- and Doppler-independent; a mixing matrix that is Doppler-independent but range-dependent; a mixing matrix dependent on both range and Doppler. This will be numerically analyzed in more detail in Chapter 5.

It is worth to remark that the noise does not provide any information about the mixing matrix. In fact, as shown in (3.14), it is introduced by each receive channel on the already combined useful signals, $\mathbf{s}$. Accordingly, an increasing noise level may make the extraction of the N useful signals more challenging, as explained in more detail in Section 3.3.5.

3.2 Higher-Order Blind Source Separation

The blind source separation (BSS) technique [90] is a signal processing technique used to separate a set of mixed signals into their individual source components without prior knowledge of the sources or the mixing process. In view of this, BSS is considered a non-deterministic technique because the original sources cannot be directly observed and therefore, the estimation of the source components relies on assumptions and statistical models.

Given a cocktail party problem as expressed in (3.1), the useful signal (wanted voice in the case of the cocktail party) may be given by solving (3.1) for $\mathbf{s}$ thus:

$$\mathbf{s} = \mathbf{B}\mathbf{x}, \tag{3.15}$$

where $\mathbf{B}$ is the separation matrix, and $\mathbf{x}$ is the vector with the mixed voices. Therefore, the task of estimating the original voice signals, given the mixed voices as the input, is tantamount to estimating the unmixing matrix, which is the matrix inverse of the mixing process. In the multichannel SAR context, the BSS separation matrix assumes the form

$$\mathbf{B} \approx \mathbf{A}^{-1}, \tag{3.16}$$

where the approximation derives from the model mismatch between (3.14) and (3.1), due to the presence of out-of-swath ambiguities and the additive noise.

The task of finding $\mathbf{B}$ is not possible to perform with conventional linear equation methods. This is due to the fact that only N variables (mixed voices) are known while the estimation of the unmixing matrix requires the estimation of N^2 unmixing matrix coefficients. Therefore, BSS uses a statistical technique based on statistical properties of the input to solve the problem. The established techniques of performing BSS can be categorized into two groups: second-order (SO) BSS such as the algorithm for multiple unknown signals extraction (AMUSE) [93], second-order blind identification (SOBI) [94], and higher-order (HO) BSS such as independent component analysis (ICA) [95], and joint approximation diagonalization of eigen-matrices (JADE) [96]. While SO BSS relies on the assumption that the useful signals are decorrelated, the HO BSS relies on a stronger assumption, which is the independence of the useful signals. In this thesis, higher-order BSS is utilized because it is expected to offer greater robustness against noise compared to second-order methods [97], [98], [99]. Additionally, the separation of the useful signals is expected to satisfy the independence assumption due to the large distance between the range ambiguities.

The idea behind the higher-order (HO) BSS algorithm is derived from the central limit theorem [100], which says that the sum of an infinitely large number of independent random variables will result in a Gaussian random variable. The concept of the central limit theorem is then adopted to the case of SAR. However, since SAR has limited number of sources, the received signal does not exactly follow a Gaussian distribution. Nevertheless, it still provides an important principle for the developed algorithm, where the received signal is more Gaussian compared to the useful signals due to the fact that sum of a finite number of independent random variables will result in a more Gaussian random variable than the original (useful) one. This principle of Gaussianity difference between the received signals and the useful signals is exploited to obtain the estimated useful signals [101]. Therefore, the

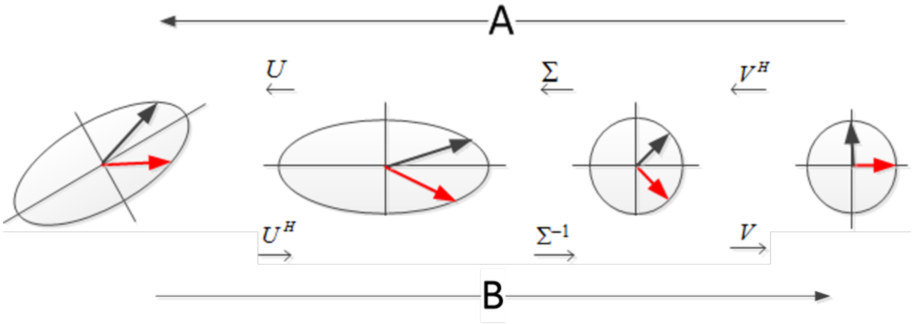

Figure 3.4: The three linear transformations involved in the singular value decomposition (SVD) of a matrix transformation [90], [102].

necessary assumption in higher-order BSS is that the independent sources need to be non-Gaussian.

In addition to the non-Gaussianity criteria, the success of both HO and SO BSS methods relies significantly on the structure of the mixing matrix. In the case of HO BSS with a very low off-diagonal mixing matrix, i.e., its off-diagonal values are very close to 0, the Gaussianity difference between the received signals and the useful signals is very small so that it is very hard for the BSS method to exploit the differences. This makes the method tend to perform worse in the case of a mixing matrix with very low off-diagonal elements. On the other hand, a mixing matrix with higher off-diagonal element values will lead to better separation performance if compared to the lower value one. This will be numerically analysed in Section 3.3.6.

As discussed in [90], [102], ICA is based on a singular value decomposition (SVD) of the mixing matrix $\mathbf{A}$. SVD is a method used in linear algebra to decompose the matrix $\mathbf{A}$ into several pieces. For any matrix, either square or rectangular, SVD states [90]:

$$\mathbf{A} = \mathbf{U}\Sigma\mathbf{V}^H, \tag{3.17}$$

where the mixing matrix $\mathbf{A}$, as shown in Figure 3.4, transforms the original sources into mixed sources by decomposition into three simpler linear transformations: a rotation $\mathbf{V}^H$, a stretch along axis Σ, and a second rotation $\mathbf{U}$. The rotation matrices $\mathbf{V}$ and $\mathbf{U}$ are unitary matrices, while Σ is a rectangular diagonal matrix with non-negative real numbers on the diagonal.

In the case of SAR, the matrix $\mathbf{A}$ is invertible due to the independence of its rows, which describe the strength of mixing for each beam. This independence ensures a nonzero determinant. Accordingly, the unmixing matrix $\mathbf{B}$ can be described as:

$$\mathbf{B} = \mathbf{A}^{-1} = \mathbf{V}\Sigma^{-1}\mathbf{U}^H, \tag{3.18}$$

which describes the transformation from mixed sources into original sources as shown in Figure 3.4.

Referring to the mixed signals, $\mathbf{x}$, and the useful signals, $\mathbf{s}$, as expressed in (3.1), the covariance matrix of the mixed signals is expressed as follows [101]:

$$\begin{aligned} E[\mathbf{x}\mathbf{x}^H] &= E[(\mathbf{A}\mathbf{s})(\mathbf{A}\mathbf{s})^H], \\ &= E[(\mathbf{U}\Sigma\mathbf{V}^H\mathbf{s})(\mathbf{U}\Sigma\mathbf{V}^H\mathbf{s})^H], \\ &= \mathbf{U}\Sigma\mathbf{V}^H E[\mathbf{s}\mathbf{s}^H]\mathbf{V}\Sigma\mathbf{U}^H. \end{aligned} \tag{3.19}$$

Assuming that $\mathbf{s}$ has zero mean and unit variance and the elements forming the vector $\mathbf{s}$ are independent from each other, it is obtained that $E[\mathbf{s}\mathbf{s}^H] = I$, where I denotes the identity matrix. Furthermore, due to the defining property of unitary matrix $\mathbf{V}^H{=}\mathbf{V}^{-1}$, (3.19) can be derived as [101]:

$$E[\mathbf{x}\mathbf{x}^H] = \mathbf{U}\Sigma^2\mathbf{U}^H. \tag{3.20}$$

On the other hand, linear algebra states that any hermitian matrix is unitarily diagonalizable by its eigenvectors, with real eigenvalues that are non-negative in the case of covariance matrices, giving [103]

$$E[\mathbf{x}\mathbf{x}^H] = \mathbf{D}\Lambda\mathbf{D}^H, \tag{3.21}$$

where $\mathbf{D}$ is a matrix whose columns are the eigenvectors of $E[\mathbf{x}\mathbf{x}^H]$ and Λ is a diagonal matrix whose diagonal elements are the real eigenvalues of $E[\mathbf{x}\mathbf{x}^H]$, which are also non-negative as the covariance matrix is also positive-semidefinite. By comparing (3.20) and (3.21), it is inferred that $\mathbf{U} = \mathbf{D}$ and $\Sigma = \Lambda^{1/2}$. Hence, (3.18) can be written as [103]:

$$\mathbf{B} = \mathbf{V}\Lambda^{-1/2}\mathbf{D}^H. \tag{3.22}$$

The step of obtaining the separation matrix $\mathbf{B}$ involves the preprocessing, which determines $\mathbf{D}$ and Λ, and ICA steps, which determines the unitary matrix $\mathbf{D}$. The post-processing step is also subsequently implemented to overcome the problem of scaling and permutation. These three steps will be discussed in the following sections.

3.2.1 Preprocessing

In the singular value decomposition (SVD) method, as described in (3.22), the preprocessing involves finding $\mathbf{D}^H$ and $\Lambda^{-1/2}$, which can be obtained through the eigenvalue decomposition of the covariance matrix of the mixed signals, as shown in (3.21). The preprocessing consists of two steps: whitening and centering.

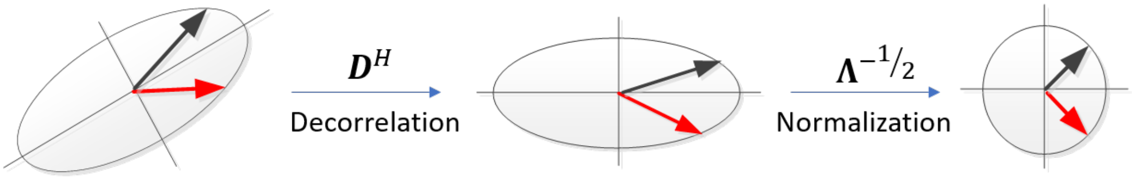

Figure 3.5: The whitening as a part of the preprocessing step. The data undergo decorrelation and normalization, resulting in a transformed data set that has equal variances along all dimensions and no linear correlations between dimensions.

The first step is whitening which is considered crucial in the preprocessing step as shown in Figure 3.5. This step ensures that the resulting data have unit variance and are uncorrelated. The whitening step is done by performing a principal component analysis (PCA), where the mixed signals undergo a rotation using the $\mathbf{D}^H$ matrix that aligns the eigenvectors of the covariance matrix of the mixed signals along the Cartesian basis, followed by normalizing the variances by multiplying with $\Lambda^{-1/2}$ such that the data have unit variance. The eigenvectors of the covariance matrix of the data are termed the principal components of the data. Projecting a data set onto the principal components removes linear correlations and provides a strategy for dimensional reduction. The whitening matrix is then given by [101]

$$\mathbf{W} = \Lambda^{-1/2}\mathbf{D}^H. \tag{3.23}$$

The second pre-processing step involves centering, which consists in subtracting the mean from each of the mixed signals. The centering is necessary due to the fact that the mixed signals in (3.19) should have a zero mean. By having zero mean signals, an identity covariance matrix of the useful signals can be achieved.

In summary, the whitening process transforms the mixed signals $\mathbf{x}$ into a new data vector $\mathbf{z}$, where each element has unit variance and the different elements are uncorrelated from each other.

$$\mathbf{z} = \mathbf{W}\mathbf{x}. \tag{3.24}$$

Independent component analysis (ICA) aims to find statistically independent components in the data. Whitening helps in achieving this goal by removing correlations between the components. In a whitened space, the components are only uncorrelated, not necessarily independent. ICA can then further extract independent components from this uncorrelated space, as described in the following section.

3.2.2 Independent Component Analysis by Higher-Order Cumulant Tensor

The objective of the ICA is to estimate a rotation matrix $\mathbf{V}$, as shown in Figure 3.6, such that, when applied to the whitening matrix $\mathbf{W}$, it maximizes the independence between the estimated sources [103].

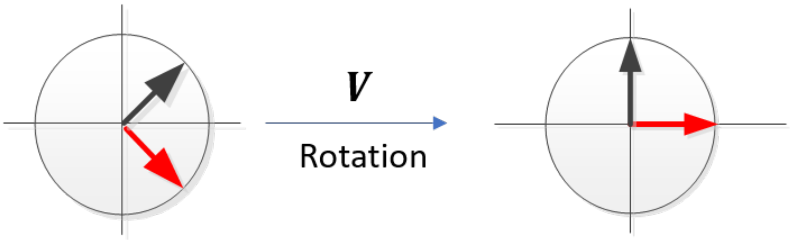

Figure 3.6: The rotation matrix in ICA, used to to maximize the independence between the signals.

One approach to accomplish this is to use a higher-order cumulant tensor [96], which can be viewed as a generalization of a matrix or linear operator. Cumulant tensors are, in turn, higher-order extensions of the covariance of $\mathbf{z}$, with the covariance matrix being the second-order cumulant tensor and the fourth-order cumulant tensor being defined by the fourth-order cumulants. The fourth-order cumulants of $\mathbf{z}$ are given by [104], [105]:

$$\begin{aligned}\mathcal{K}_z = {} & E[z_i z_j^* z_k^* z_l] - E[z_i z_j^*]E[z_l z_k^*] \\ & - E[z_i z_k^*]E[z_l z_j^*] - E[z_i z_l]E[z_j^* z_k^*],\end{aligned} \tag{3.25}$$

where $\mathbf{z}$ is the vector with the whitened signals as a result of the pre-processing step discussed in the previous section; indices $1 \leq i, j, k, l \leq N$ refer to the index of the whitened signals, with N denoting the total number of whitened signals.

The fourth-order cumulants can be regarded as a fourth-order tensor due to having four elements rather than the customary two. This fourth-order tensor essentially captures the statistical relationship between the sources, with the independence of the sources being linked to their non-Gaussian nature, due to the fact that statistical independence implies that all cross-cumulants vanish, while Gaussianity implies that all elements (also diagonal) vanish. In particular, when the sources are non-Gaussian and if the sources are independent, the off-diagonal entries of the fourth-order cumulant tensor will be vanish. To attain this independence, the rotation matrix $\mathbf{V}$ must be generated to diagonalize the fourth-order cumulant tensor. However, this fourth-order cumulant tensor is a complex N^4-dimensional tensor, which is a high-dimensional array, making it typically unlikely that it can be exactly diagonalized by $\mathbf{V}$. This is because the degrees of freedom in the fourth-order cumulant tensor scales as $O(N^4)$, which far exceeds the N^2 degrees of freedom available in the rotation matrix $\mathbf{V}$ [106]. This imbalance implies that it is generally impossible to eliminate all off-diagonal elements, as the transformation does not have enough freedom to fully diagonalize the tensor.

In order to overcome the complexity, an important step proposed in the joint approximation diagonalization of eigen-matrices (JADE) algorithm [96] involves implementing a linear transformation into the space of N^2-dimensional tensors, commonly referred to as matrices, rather than the N^4-dimensional tensor. The space of these matrices is a linear space of dimension $N \times N$, with the i, jth element of the matrix obtained through the transformation denoted as $\mathbf{F}_{ij}$, also known as a cumulant matrix, and defined as [103]

$$\mathbf{F}_{ij}(\mathbf{M}) = \sum_{kl} m_{kl} \mathcal{K}_z, \tag{3.26}$$

where m_{kl} are the elements of the matrix $\mathbf{M}$ that is transformed and indices $1 \leq k, l \leq N$ refer to the index of the whitened signals. It is important to note that the cumulant matrix is diagonalizable by a unitary matrix, which becomes the aim of the algorithm.

There is no strict guideline on how to choose $\mathbf{M}$. In [96], it is suggested that $\mathbf{M}$ should be the eigenmatrices of the cumulant tensor. The eigenmatrices are obtained by reshaping the cumulant tensor through a stacking procedure into a matrix. Subsequently, the eigenvalue decomposition (EVD) is performed to obtain N^2 eigenvalues and N^2 eigenvectors, where each eigenvector has a length of N^2. The eigenvector is then reshaped, using an unstacking procedure, to obtain N^2 eigenmatrices with shape $N \times N$. The selection of eigenmatrices as the value of $\mathbf{M}$ leads to a another representation of cumulant matrices, given by

$$\mathbf{F}(\mathbf{M}_r) = \lambda_r \mathbf{M}_r, \tag{3.27}$$

where $\left\{\lambda_r, \mathbf{M}_r\right\}$ is a set of eigenvalues and eigenmatrices, respectively, with $1 \leq r \leq N^2$.

Due to the independence between sources, there are $N(N-1)$ zero eigenvalues and N eigenvalues equal to the kurtosis of the sources [96]. This is, in fact, the great advantage of choosing the eigenmatrices of the cumulant tensor because it reduces the complexity from having N^2 matrices to only N matrices.

The diagonalization process refer to a process where matrix $\mathbf{V}$ is used to diagonalize a set of different matrices $\mathbf{F}(\mathbf{M}_r)$. The aim is to make the matrices $\mathbf{Q} = \mathbf{V}^H \mathbf{F}(\mathbf{M}_r) \mathbf{V}$

as diagonal as possible [103]. There are various methods to measure the diagonality of a matrix $\mathbf{Q}$, aiming to achieve a diagonal matrix wherein the sum of squares of off-diagonal elements attains the minimum value. One approach involves calculating this sum of squares of off-diagonal elements, expressed as $\sum_{k\neq l} q_{kl}^2$. Alternatively, it is expected that an orthogonal matrix $\mathbf{V}$ does not alter the total sum of squares of a cumulant matrix. Therefore, minimizing the sum of squares of off-diagonal elements is equivalent to maximizing the sum of squares of diagonal elements. To measure the diagonality of a matrix, JADE uses the following measure

$$C(\mathbf{V}, \mathcal{N}) = \sum_{r=1}^{N} \left\| \mathrm{diag}(\mathbf{V}^H \mathbf{N}_r \mathbf{V}) \right\|^2, \tag{3.28}$$

where $\mathbf{N}_r = \mathbf{F}(\mathbf{M}_r)$; $\|\cdot\|$ represents the L^2-norm; diag$(\cdot)$ is the vector constructed from the diagonal elements of the matrix argument; and $\mathcal{N} = \mathbf{N}_r | 1 \leq r \leq N$.

The term 'joint diagonalization' refers to the circumstance where a set of matrices $\mathbf{N}_r$ is diagonalized by a rotation matrix $\mathbf{V}$. However, exact joint diagonalization by the Jacobi technique [107] is often only possible when dealing with two matrices. If there is common structure among more than two matrices, then exact joint diagonalization may be challenging to achieve due to the increased complexity of the interdependencies between the matrices, making it unlikely that a single rotation matrix can satisfy the diagonalization conditions for all matrices simultaneously. In such cases, only approximate joint diagonalization is feasible. To achieve joint approximate diagonalization of a set of arbitrary $N \times N$ matrices $\mathbf{N}_r | 1 \leq r \leq N$ and to obtain the rotation matrix $\mathbf{V}$, the Jacobi technique needs to be extended to the case of several matrices, as presented in Appendix A.

3.2.3 Postprocessing

After completing the preprocessing and independent component analysis (ICA) steps, the separation matrix $\mathbf{B}$ can be obtained as the product of the whitening matrix $\mathbf{W}$ and the rotation matrix $\mathbf{V}$

$$\mathbf{B} = \mathbf{V}\mathbf{W}. \tag{3.29}$$

However, two fundamental issues encountered in blind source separation (BSS) are scaling and permutation uncertainty, which still persist even after the completion of the preprocessing and ICA steps. As a result, the solution of ICA in general not unique. The issue of scaling uncertainty happens because the amplitude of the sources cannot be uniquely determined from their observed output. Thus, there are multiple solutions for the source signals and the mixing matrix that can produce the same mixture. The issue of permutation uncertainty arises because the order of the sources in the mixture cannot be determined from the observations. In the context of SAR, this implies that the estimated useful signal cannot be identified as originating from a specific subswath. Therefore, there are multiple permutations of the same set of sources that can yield the same mixture. Post-processing is necessary to address these uncertainties and obtain the final solution. During the post-processing step, (3.15) can be rewritten as

$$\hat{\mathbf{s}} = \mathbf{P}\mathbf{B}\mathbf{x}, \tag{3.30}$$

where $\mathbf{P}$ is the permutation matrix, defined as

$$p_{ik} = \delta_{k,l(i)}, \tag{3.31}$$

where p is an element of the matrix; $l(i)$ the permutation order for the i-th row and $1 \leq i \leq N$; and δ_{kl} the Kronecker delta. The value $l(i)$ must vary from row to row and not repeat. For example, with $l(i) = 2, 3, 1$, the matrix is given by:

$$\mathbf{P}_{3\times 3} = \begin{bmatrix} 0 & 1 & 0 \\ 0 & 0 & 1 \\ 1 & 0 & 0 \end{bmatrix}. \tag{3.32}$$

When a permutation matrix is multiplied by another matrix, it results in the row permutation of the matrix to its right according to $l(i)$ or the column permutation of the matrix to its left. An example of this operation can be observed in

$$\begin{aligned} \mathbf{P}_{3\times 3} \cdot \mathbf{B}_{3\times 3} &= \begin{bmatrix} 0 & 1 & 0 \\ 0 & 0 & 1 \\ 1 & 0 & 0 \end{bmatrix} \cdot \begin{bmatrix} b_{11} & b_{12} & b_{13} \\ b_{21} & b_{22} & b_{23} \\ b_{31} & b_{32} & b_{33} \end{bmatrix}, \\ &= \begin{bmatrix} b_{21} & b_{22} & b_{23} \\ b_{31} & b_{32} & b_{33} \\ b_{11} & b_{12} & b_{13} \end{bmatrix}. \end{aligned} \tag{3.33}$$

There are two key pieces of information within the mixing matrix formulation in the case of SAR, which are important for solving the scaling and permutation uncertainties: (i) the mixing matrix $\mathbf{A}$ is a unit matrix where the diagonal elements are 1,i.e., $a_{ii} = 1$, as shown in (3.14) and (ii) the off-diagonal values are less than 1, i.e., $|a_{ij}| < 1$, for $i \neq j$. Based on the information (ii), the permutation order is obtained as follows:

$$l(i) = \arg\max_{j} |b_{i,j}|, \tag{3.34}$$

where $b_{i,j}$ is the element of matrix $\mathbf{B}$; and i and j denote row and column of the matrix element, respectively.

Furthermore, once the permutation matrix is obtained, and considering that the diagonal elements of the desired matrix are 1 (according to the cocktail party model in SAR as derived in (3.14)), the scaling uncertainty can be solved by normalizing the matrix such that diagonal elements are 1, by:

$$b_{i,j} = \frac{b_{i,j}}{b_{i,i}}, \tag{3.35}$$

where $b_{i,j}$ is the element of the permuted matrix $(\mathbf{P} \cdot \mathbf{B})$

It is worth recalling that higher-order ICA methods rely on the non-Gaussianity of the sources to achieve good performance. Moreover, there are other factors in SAR that may have an adverse effect on the performance, as will be demonstrated in the simulation in Chapter 5.

3.3 BSS Performance in the SAR Context

This section explores the factors influencing the performance of BSS in SAR signal processing. Initially designed to solve the cocktail party problem, the implementation of BSS has been extended to image processing, biomedical signal processing, communication systems, seismic signals, and various other domains [108], [109], [110], [111]. It is important to note that different fields possess distinct characteristics. Therefore, investigating potential aspects that might degrade the performance of BSS in the case of SAR is crucial.

3.3.1 Simulation Procedure

To properly investigate the factors that influence the performance of BSS in the SAR context, a numerical analysis of BSS is conducted on a realistic complex-valued SAR signal. Figure 3.7 shows how the SAR raw data, $\mathbf{s}$, and range-compressed data, $\mathbf{s}'$, are generated, by ignoring the range cell migration effect. The simulation commences by using a SAR image, in this case a TerraSAR-X image [112], as the input. The initial step involves generating range-compressed data by performing reverse SAR processing. This requires transforming the input SAR image into the range-time and azimuth frequency domain, which is then multiplied with the conjugate of the phase function of the azimuth chirp in the frequency, $H^{*}_{az}(f_t)$. Furthermore, to obtain the raw data, the range-compressed data in the frequency domain are multiplied with the conjugate of the phase function of the range chirp in the frequency domain,

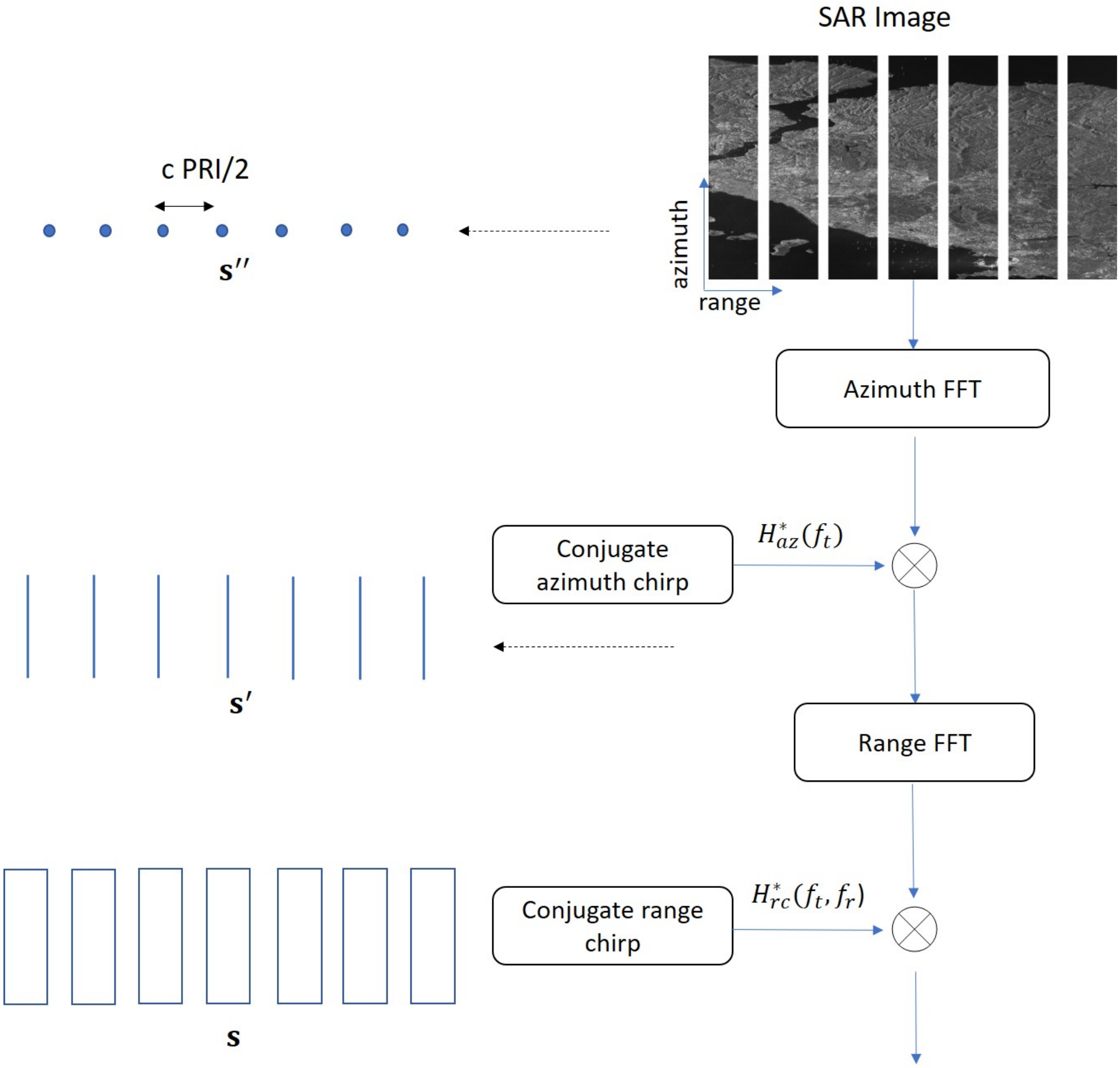

Figure 3.7: Flowchart illustrating the simplified process of generating range-compressed data $\mathbf{s}'$ and raw data $\mathbf{s}$, using SAR image $\mathbf{s}''$ from TerraSAR-X as the input. The diagram illustrates seven sub-swathes, with a range ambiguity distance of $c\,PRI/2$.

$H^*_{rc}(f_t, f_\tau)$. It is crucial to note that the TerraSAR-X parameters [112] are employed in generating both the azimuth and range chirps.

The BSS will be applied to SAR signals by considering SAR data from a single range bin and the entire azimuth line of the SAR signal. The focus of this section is on the characteristics of the SAR signal, and a simple, straightforward procedure will be used to obtain a range ambiguous SAR signal. More realistic multichannel SAR data, incorporating acquisitional aspects such as antenna pattern and range migration effect, will be simulated in Chapter 5. Accordingly, a range ambiguous SAR raw data signal, $\mathbf{x}$, is obtained by

$$\mathbf{x} = \mathbf{A}\mathbf{s}, \tag{3.36}$$

where $\mathbf{A}$ denotes the mixing matrix, and $\mathbf{s}$ the useful signal. To provide a basis for comparison with the range-ambiguous raw data, range-compressed data are also produced using a similar procedure;

$$\mathbf{x}' = \mathbf{A}\mathbf{s}', \tag{3.37}$$

where the symbol $'$ is used to denote the range-compressed data. Furthermore, the range-ambiguous image data are generated by the following simplified procedure:

$$\mathbf{x}'' = \mathbf{A}\mathbf{s}'', \tag{3.38}$$

where the symbol $''$ is used to denote the image data.

The values of the mixing matrix used in the simulation in this section are considered in a way that the RASR is higher in the far range compared to that in the near range. This is a typical characteristic of the antenna pattern in the SAR system, as the angular separation between the useful signal and the corresponding ambiguities decreases, resulting in a higher ambiguity level in the far range.

In addition to the type of data (range compressed and raw data), various factors such as the number of sources, N, out-of-swath ambiguity signals, $\mathbf{s}_{WA}$, signal-to-noise ratio, SNR, and the values of the mixing matrix, $\mathbf{A}$, are also investigated. The numerical analysis of each investigated factor will be presented in the remaining sections of this chapter. The BSS's performance is assessed based on the SAR signal quality using the range ambiguity-to-signal ratio (RASR), which is defined as [54]:

$$RASR(k) = \frac{\sum_{j=0}^{N_a-1} |x(k,j) - s(k,j)|^2}{\sum_{j=0}^{N_a-1} |s(k,j)|^2}, \tag{3.39}$$

where k denotes the range bin; j the azimuth sample index; N_a the number of azimuth samples; $x(k,j)$ the complex value of the range-ambiguous signal; and $s(k,j)$ the complex value of the useful signal. When evaluating the RASR after BSS, the range-ambiguous signal $\mathbf{x}$ is replaced by the ambiguity-suppressed image $\hat{\mathbf{s}}$. In some cases, the performance is assessed using the average RASR, given by

$$\overline{RASR} = \frac{1}{N_r} \sum_{k=0}^{N_r-1} RASR(k), \tag{3.40}$$

where N_r is the number of range samples.

In order to provide a more quantitative assessment of the Gaussianity of the SAR signal, the complex signal kurtosis ($\mathcal{CSK}$) is used as a metric. The $\mathcal{CSK}$ measures the deviation of a signal amplitude's probability distribution from a Gaussian distribution. For a complex signal s, the moment is defined as follows:

$$\mu_{l,m} = E\{(s - E\{s\})^l (s - E\{s\})^{*m}\}, \tag{3.41}$$

where $*$ is the complex conjugate. Indices l, m indicate the order of the moment. The standardized moments are defined by

$$\mu'_{l,m} = \frac{\mu_{l,m}}{\sigma^{l+m}}, \tag{3.42}$$

where the variance $\sigma^2 = \mu_{1,1}$. The complex signal kurtosis is defined as [113]:

$$\mathcal{CSK} = \mu'_{2,2} - 2 - \left|\mu'_{2,0}\right|^2 . \tag{3.43}$$

According to [114], a Gaussian distribution means a $\mathcal{CSK}$ value close to 0. In contrast, a higher absolute value of $\mathcal{CSK}$ indicates that the data are more non-Gaussian. There is no strict rule defining the threshold for data to be considered Gaussian or non-Gaussian. Later in Chapter 6, it is discussed that a value of $|\mathcal{CSK}|$ greater than 2.3 represents the threshold for non-Gaussianity.

3.3.2 Type of Data

The first analyzed factor concerns the types of SAR signal data. Accordingly, various types of SAR data exist, such as raw data, range compressed data, and image data. As stated earlier, the preliminary analysis in this chapter only takes into account one azimuth line of the SAR signal for each source, with adjacent sources separated by a distance of $c \cdot PRI/2$. In this particular case, three sources ($N = 3$) are considered, as illustrated in Figure 3.8, and the arbitrary mixing matrix $\mathbf{A}_3$ is chosen:

$$\mathbf{A}_3 = \begin{bmatrix} 1 & 0.12 + 0.12j & 0.18 + 0.15j \\ 0.39 + 0.27j & 1 & 0.27 + 0.12j \\ 0.3 + 0.15j & 0.39 + 0.27j & 1 \end{bmatrix} . \tag{3.44}$$

The BSS method is then utilized on all three range-ambiguous signals $\mathbf{x}$, $\mathbf{x}'$, and $\mathbf{x}''$. The results, as shown in Figure 3.9, indicate that the BSS approach is significantly more effective in focused data when compared to raw and range-compressed data. This is due to the fact that the image data possess significantly higher non-Gaussianity properties, which is a result of the compression process especially along azimuth, as demonstrated in Table 3.1. As compared to the focused data, the raw data in the time domain are formed by a linear combination of the scene's backscattering in the antenna field of view. Since the radar's instantaneous field of view

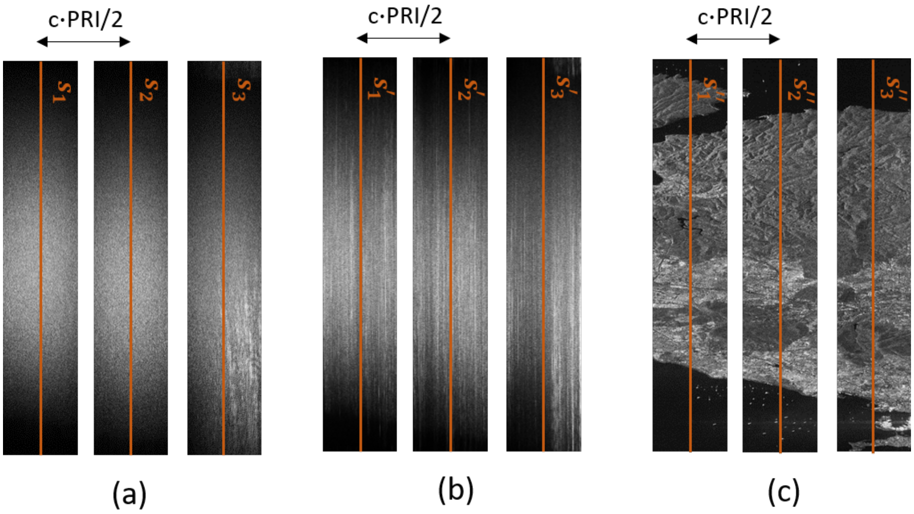

Figure 3.8: An unambiguous SAR signal, where (a) shows the raw signals, $\mathbf{s}$, (b) shows the range-compressed signals , $\mathbf{s}'$, and (c) shows the fully-focused signals, $\mathbf{s}''$.

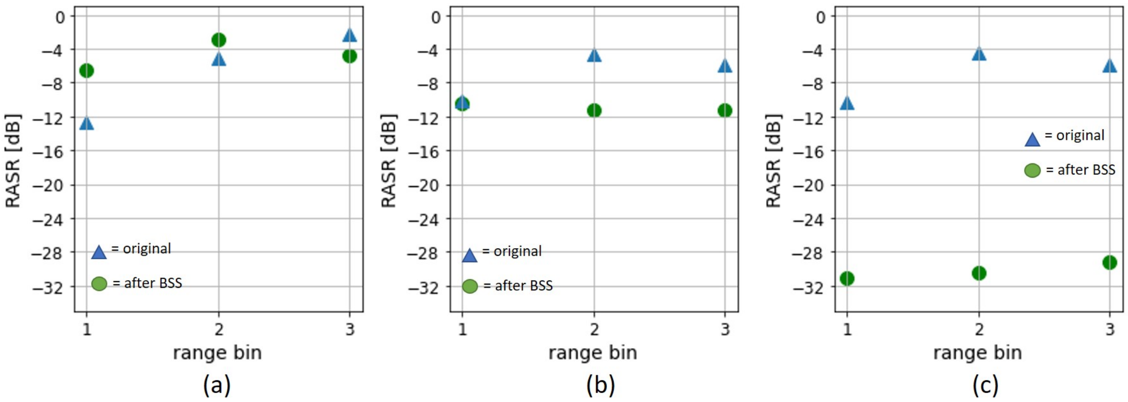

Figure 3.9: RASR performance of BSS in (a) raw signals, (b) range-compressed signals, and (c) fully focused signals. In (b), the RASR values in range bin 1, before and after the BSS method, is superimposed.

is extensive in both range and azimuth, the superposition comprises significant contributions, ultimately leading to a raw signal with higher levels of Gaussianity than the focused data [115].

Based on the aforementioned Gaussianity factor, it can be concluded that the implementation of BSS on image data is more effective than on raw and range-compressed data. However, it is crucial to note that Gaussianity is the only factor considered in this preliminary and simplified analysis. When the actual SAR acquisition geometry is taken into account, which includes the azimuth compression process, another challenge arises when implementing BSS on image data. This will be discussed further in Chapter 4. Despite this, the remaining portion of this section will consider range-compressed data as the input.

Table 3.1: Complex Signal Kurtosis for SAR data in Figure 3.8.

Type of Data	Range Bin		
	1	2	3
Raw data ($\mathbf{s}$)	1.89	1.68	1.66
Range-compressed data ($\mathbf{s}$')	2.44	1.75	1.56
Image data ($\mathbf{s}$")	24.3	16.2	150.1

3.3.3 Number of Sources

The next analysis pertains to the impact of the number of sources, N, on the BSS performance. The number of sources is linked to the number of sub-swaths in a practical multichannel SAR setting. In this case, $N = 3, 5, 7$ are examined. The corresponding signals for different values of N are illustrated in Figure 3.10.

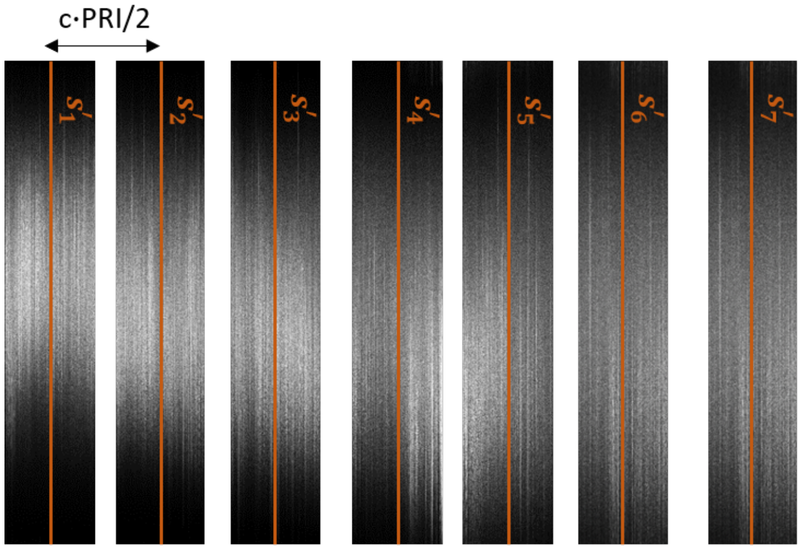

Figure 3.10: Seven ambiguity-free range-compressed signals denoted as $\mathbf{s}'_1$ through $\mathbf{s}'_7$. Three distinct scenarios are examined. In the first scenario, when the number of sources is $N = 3$, the signals utilized are $\mathbf{s}'_3$ through $\mathbf{s}'_5$. In the second scenario, with $N = 5$, the signals employed are $\mathbf{s}'_2$ through $\mathbf{s}'_6$. In the third scenario, where $N = 7$, all seven signals are utilized, namely $\mathbf{s}'_1$ through $\mathbf{s}'_7$.

To ensure a fair assessment of all cases, the mixing matrix's values must be calculated in a manner that result in comparable RASR values across all cases. Therefore, despite the different number of sources, all should correspond to similar average

RASR values. When $N = 3$, the mixing matrix, $\mathbf{A}_3$, as presented in (3.44) is utilized. For $N = 5$, the mixing matrix $\mathbf{A}_5$ is designed as:

$$\mathbf{A}_5 = \begin{bmatrix} 1 & 0.18+0.09j & 0.12+0.09j & 0.06+0.03j & 0.03+0.03j \\ 0.18+0.18j & 1 & 0.15+0.12j & 0.12+0.09j & 0.09+0.09j \\ 0.21+0.18j & 0.24+0.18j & 1 & 0.18+0.09j & 0.12+0.09j] \\ 0.15+0.12j & 0.21+0.09j & 0.24+0.18j & 1 & 0.09+0.24j \\ 0.18+0.12j & 0.24+0.21j & 0.24+0.24j & 0.34+0.34j & 1 \end{bmatrix}, \tag{3.45}$$

and for $N = 7$, the mixing matrix $\mathbf{A}_7$ is designed as:

$$\mathbf{A}_7 = \begin{bmatrix} 1 & 0.2+0.1j & 0.13+0.11j & 0.08+0.05j & 0.03+0.04j & 0.02+0.02j & 0.015+0.01j \\ 0.2+0.2j & 1 & 0.1+0.1j & 0.13+0.11j & 0.18+0.15j & 0.12+0.11j & 0.10+0.08j \\ 0.23+0.21j & 0.3+0.2j & 1 & 0.2+0.1j & 0.15+0.09j & 0.11+0.04j & 0.09+0.02j \\ 0.17+0.15j & 0.23+0.11j & 0.3+0.2j & 1 & 0.1+0.3j & 0.1+0.24j & 0.07+0.21j \\ 0.22+0.15j & 0.27+0.25j & 0.3+0.3j & 0.4+0.4j & 1 & 0.3+0.3j & 0.23+0.25j \\ 0.15+0.20j & 0.22+0.22j & 0.25+0.27j & 0.31+0.28j & 0.4+0.4j & 1 & 0.37+0.36j \\ 0.14+0.10j & 0.24+0.2j & 0.2+0.3j & 0.25+0.27j & 0.3+0.31j & 0.37+0.38j & 1 \end{bmatrix}. \tag{3.46}$$

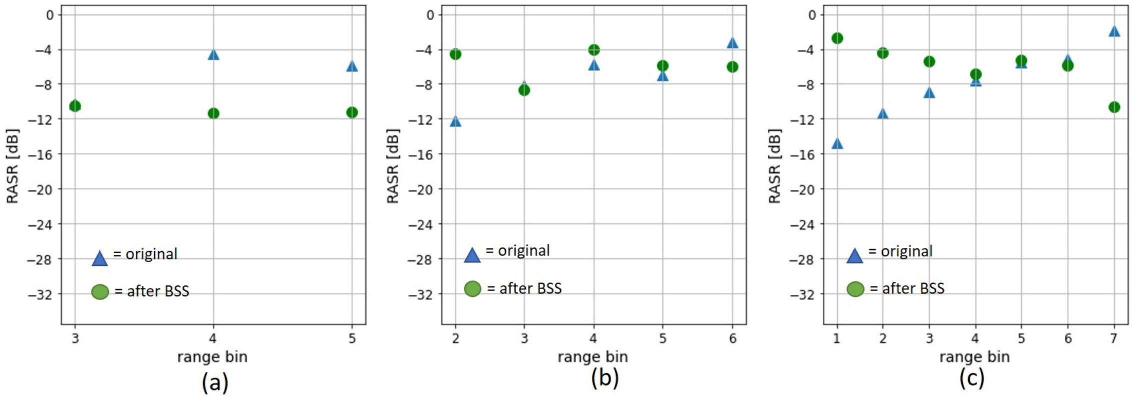

(a) (b) (c)

Figure 3.11: RASR performance of BSS in (a) $N = 3$ (b) $N = 5$ (c) $N = 7$. In (a), the RASR value in range bin 3, before and after BSS, are superimposed.

Figure 3.11 displays the RASR performance of the BSS method for different numbers of sources. This figure reveals the inadequacies of conventional BSS methods when applied to practical situations. Specifically, the results indicate that BSS methods perform better in cases with fewer source signals than with a higher numbers of sources, as it becomes increasingly difficult to separate the sources as the number of sources increases. When there are fewer sources, the mixing matrix has fewer dimensions, and consequently, the number of independent components that need to be extracted is also smaller. In contrast, when the number of sources is high, the mixing matrix becomes more complex, and there are more independent components that need to be extracted, making the separation task more challenging. Therefore, in cases with fewer sources, the BSS methods can achieve a higher separation accuracy, while in cases with more sources, a larger number of input samples, i.e., a longer SAR signal observations, is required to improve the estimation of the higher-order statistics. For the remainder of this chapter, the case of $N = 5$ source signals is considered.

3.3.4 Out-of-Swath Ambiguity Signal

This section analyzes the presence of the out-of-swath ambiguity signals. Remember that according to the discussion in Section 3.1.1, in its simplest form, the cocktail party problem can be expressed as follows:

$$\mathbf{x}' = \mathbf{A}\mathbf{s}', \tag{3.47}$$

where $\mathbf{x}'$ is a vector with the range-compressed mixed signals; $\mathbf{A}$ is the mixing matrix; and $\mathbf{s}'$ is the vector with the range-compressed source signals.

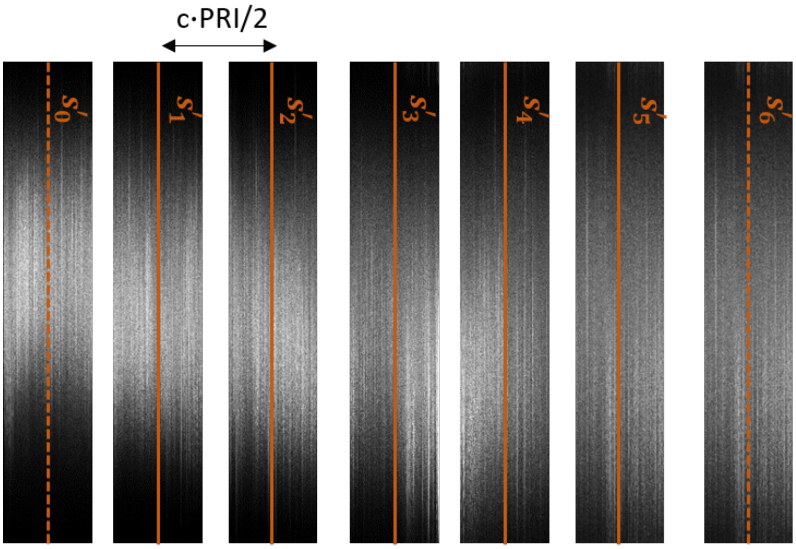

Figure 3.12: Simulated ambiguity-free range compressed signals for the case of $N = 5$, where $s_1 - s_5$ (solid lines) are the inside-swath signals and s_0, s_6 (dotted lines) are the out-of-swath ambiguity signals.

In the case of a multichannel SAR system, as discussed in Section 3.1.2, the cocktail party equation involves out-of-swath range-ambiguity signals, denoted by $\mathbf{s}'_{WA}$, which arise from outside the intended swath. To analyze the impact of $\mathbf{s}'_{WA}$ on the performance, the noise, $\mathbf{n}$, is excluded in this section. Therefore, the cocktail party equation can be expressed as

$$\mathbf{x}' = \mathbf{A}\mathbf{s}' + \mathbf{s}'_{WA}. \tag{3.48}$$

Figure 3.12 shows five range-compressed useful signal sources, denoted as $s'_1 - s'_5$, are simulated, and they are mixed by the mixing matrix $\mathbf{A}_5$ as specified in (3.45). Additionally, $\mathbf{s}'_{WA}$ is simulated by weighting the signal originating from outside the intended swath, in this case s'_0 and s'_6, and is subsequently added to the equation as described in (3.48). Specifically, the simulated value of $\mathbf{s}'_{WA}$ is

$$\begin{bmatrix} s'_{1,WA}(\tau_1) \\ s'_{2,WA}(\tau_1) \\ s'_{3,WA}(\tau_1) \\ s'_{4,WA}(\tau_1) \\ s'_{5,WA}(\tau_1) \end{bmatrix} = \begin{bmatrix} (0.09+0.06j)s'_0(\tau_1) + (0.03+0.03j)s'_6(\tau_1) \\ (0.06+0.12j)s'_0(\tau_1) + (0.09+0.09j)s'_6(\tau_1) \\ (0.15+0.06j)s'_0(\tau_1) + (0.09+0.03j)s'_6(\tau_1) \\ (0.15+0.12j)s'_0(\tau_1) + (0.24+0.15j)s'_6(\tau_1) \\ (0.15+0.12j)s'_0(\tau_1) + (0.42+0.42j)s'_6(\tau_1) \end{bmatrix}. \tag{3.49}$$

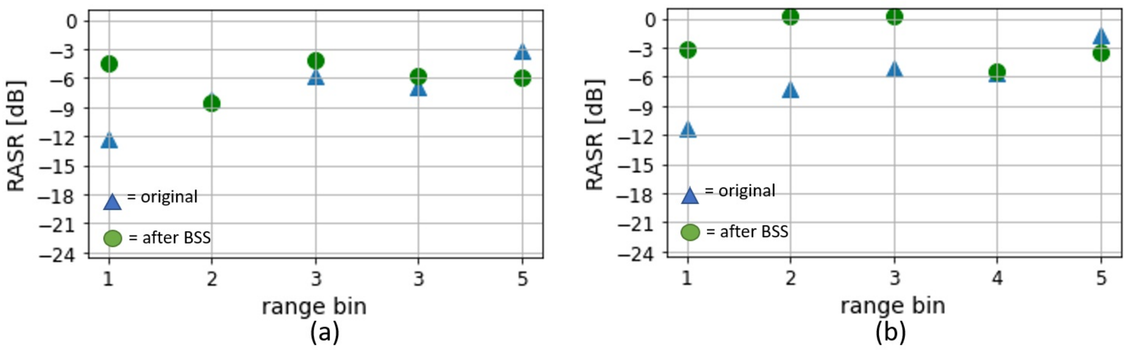

(a) (b)

Figure 3.13: RASR performance of range compressed data with $N = 5$, in the absence (a) and presence (b) of out-of-swath range-ambiguity signals, denoted as $\mathbf{s}'_{WA}$.

Figure 3.13 shows the impact of out-of-swath ambiguity signals on the performance of the BSS method. This figure highlights the limitations of conventional BSS implementations in practical scenarios. Specifically, the presence of $\mathbf{s}'_{WA}$ considerably degrades the RASR performance compared to the absence of $\mathbf{s}'_{WA}$. This is due to the fact that the out-of-swath ambiguity signals, in the context of SAR, can be considered as non-Gaussian noise. Accordingly, non-Gaussian noise can cause the BSS algorithm to mistake the noise for a source signal or misidentify the source signals themselves. Moreover, the statistical structure of non-Gaussian noise can differ substantially from Gaussian noise, leading to unique patterns in the mixed signals that are challenging for the separation algorithm to detect and isolate.

3.3.5 Semi-White Gaussian Noise

The original model of the cocktail party problem, as presented in Section 3.1.1, where the BSS method is designed to solve such a problem, excludes the contribution of noise. However, in the case of SAR, noise is introduced by each received channel onto the already combined useful signals, $\mathbf{s}$, as shown in (3.14). The discussion in [97] indicates that the presence of noise, particularly Gaussian noise, influences the performance of BSS, as the mixing matrix does not provide information about the noise. Additionally, Gaussian noise also affects the Gaussianity of the signals.

The choice of Gaussian noise as the noise model in this analysis is based on its widespread acceptance within the radar field [116]. Specifically, semi-white Gaussian noise is selected. Semi-white Gaussian noise represents a random signal or interference that conforms to a Gaussian distribution but possesses a variance that varies across frequencies, distinguishing it from pure white Gaussian noise [117]. The selection of semi-white Gaussian noise is attributed to the application of the BSS method on the SAR downlinked received signal, which undergoes bandpass filtering, resulting in noise that is bandlimited and present within the received signal.

The impact of noise, n, is assessed by simulating various SNR levels, where the relationship between noise and SNR is given by:

$$\sigma_n = \frac{\sigma_{x'}}{\sqrt{10^{\left(\frac{\mathrm{SNR}}{10}\right)}}}, \tag{3.50}$$

where σ_n and $\sigma_{x'}$ denote the standard deviations of the noise, n, and the input signal, x', respectively.

The simulation consists of $N = 5$ with s'_1 to s'_5 as illustrated in Figure 3.13, the mixing matrix A_5 with values as specified in (3.45), and $\mathbf{s}'_{WA}$ is excluded. The SNR levels are varied between 5-15 dB. Figure 3.14 illustrates the impact of different levels of SNR on the performance of the BSS method. The results demonstrate that lower SNR, i.e., higher noise levels, have performance that is considerably similar to that of higher SNR. As discussed in [118], [97], [98], [99], this is due to the fact that cumulant-based BSS techniques like JADE are not influenced by additive Gaussian noise, as the cumulants are invariant to it. This is, in fact, an advantage of using HO BSS compared to SO BSS, where in SO BSS, the presence of noise considerably degrades the performance.

The poor performance of BSS in Figure 3.14, as indicated in Section 3.3.2, is due to the limited number of samples and could be improved by providing a larger number of input samples, which will be discussed in Chapter 4.

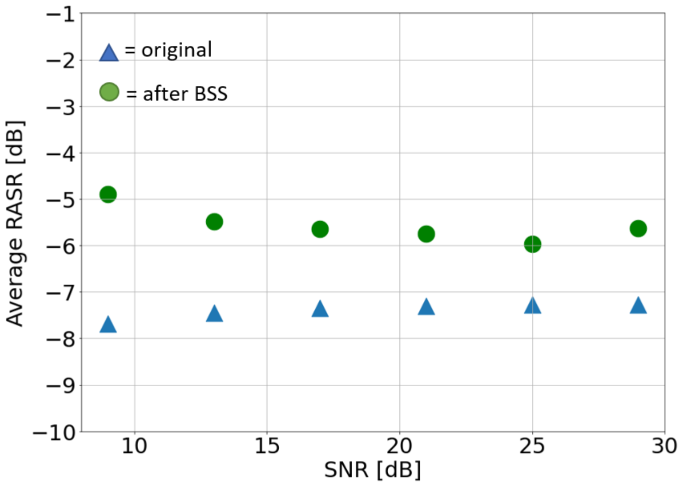

Figure 3.14: RASR performance for different SNR value.

3.3.6 Mixing Matrix Value

This section investigates the impact of the mixing matrix values on the BSS performance. The absolute value of the mixing matrix plays a crucial role in the BSS as it determines the relationship between the observed mixed signals and the underlying source signals. In the context of range ambiguities within multiple elevation beam SAR systems, the mixing matrix has unit diagonal elements as modeled in (3.14). Therefore, the value of the mixing matrix is primarily determined by its off-diagonal elements.

In the previous sections, the considered mixing matrix is associated with an average original RASR value of approximately -7.5 dB (see Figure 3.14). However, this value may not be representative for SAR, especially when the DBF and SCORE technique is already employed and thus results in lower, i.e., better, RASR values. To investigate the effect of the mixing matrix's values, a simulation is conducted with $N = 5$ using the simulated signals in Figure 3.12. However, to focus solely on the effect of the mixing matrix's values, the simulation excluded both the noise $\mathbf{n}$ and out-of-swath ambiguity signals $\mathbf{s}_{WA}$ and only includes $s'_1 - s'_5$. Furthermore, in order to provide a performance comparison, lower off-diagonal values are introduced in the mixing matrix

$$\mathbf{A}_{5,\text{low}} = \begin{bmatrix} 1 & 0.06+0.03j & 0.04+0.03j & 0.02+0.01j & 0.01+0.01j \\ 0.06+0.06j & 1 & 0.05+0.04j & 0.04+0.03j & 0.03+0.03j \\ 0.07+0.06j & 0.08+0.06j & 1 & 0.06+0.03j & 0.04+0.03j \\ 0.05+0.04j & 0.07+0.03j & 0.08+0.06j & 1 & 0.03+0.08j \\ 0.06+0.04j & 0.08+0.07j & 0.08+0.08j & 0.11+0.11j & 1 \end{bmatrix}. \tag{3.51}$$

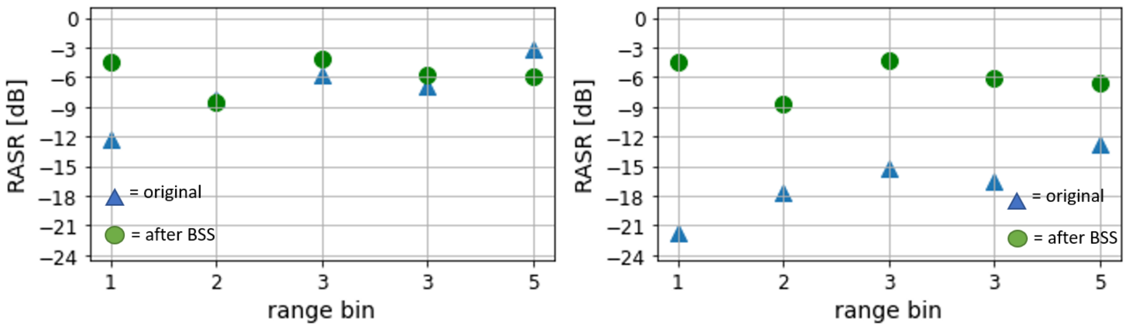

(a) (b)

Figure 3.15: RASR for the case of range-compressed data with $N = 5$ for (a) high-value mixing matrix $\mathbf{A}_5$ and (b) low value mixing matrix $\mathbf{A}_{5,low}$.

Figure 3.15 presents the comparison of the BSS method using two different SAR signals: one obtained from a mixing matrix with high off-diagonal values, $\mathbf{A}_5$, and another from a mixing matrix with low off-diagonal values, $\mathbf{A}_{5,low}$. This figure indicates that conventional BSS implementation does not deliver satisfactory results in real-world applications. Specifically, the result shows that using a lower off-diagonal values mixing matrix leads to more challenging outcomes. Specifically, the provided $A_{5,low}$ produces a RASR performance that is worse even after applying the BSS method compared to the original mixed signals. This is due to the fact that in the case of a low off-diagonal values mixing matrix, the Gaussianity of the mixed signals are highly similar to the source signals themselves. Therefore, the higher-order BSS algorithm's ability to exploit non-Gaussianity differences between the mixed and source signals becomes less effective. In order to improve the sensitivity, a larger number of input samples should be provided, which will be discussed in Chapter 4.

3.4 Conclusions

The application of the cocktail party phenomenon in multichannel SAR systems, which employ multiple elevation beams, offers the potential to utilize methods based on BSS to suppress range ambiguities. The remarkable aspect of this method is that it does not require any prior knowledge of the antenna pattern. Due to the independence of SAR signals and the robustness against noise, a higher-order BSS method is proposed. Unlike the traditional cocktail party problem, that encounters scaling and permutation uncertainties resulting in non-unique solutions, a unique solution can be achieved when dealing with the cocktail party problem in multichannel SAR. This provides a comparative advantage for applying BSS in multichannel SAR, as compared to other fields such as audio signal processing, image processing, biomedical signal processing, communication systems, and many others.

The numerical investigation of BSS in SAR reveals its potential in suppressing range ambiguities. However, the significantly degraded performance caused by various factors typically present in SAR must be carefully considered. These factors include the defocused data (raw and range-compressed data), number of sources, presence of out-of-swath ambiguity signals, and magnitude of the off-diagonal elements of the mixing matrix. When these factors are combined, implementing BSS alone does not longer effectively suppresses range ambiguities. In opposite, the conventional implementation of the BSS approach leads to an increase of the range ambiguities. Therefore, additional approaches must be proposed to provide a more robust technique, as discussed in the next sections. Furthermore, other factors such as range cell migration and reciprocity issues in the focused image, will also be considered in the following chapter.

4 Range Ambiguity Suppression Method

The BSS method has been verified in principle as a promising technique to suppress range ambiguities in multichannel SAR systems, as explained in Chapter 3. This is mainly due to the cocktail party phenomenon present in multichannel SAR systems where multiple elevation Rx beams are utilized. However, as previously analyzed, achieving good RASR performance is extremely challenging. This chapter proposes a range ambiguity suppression method that utilizes the blind source separation technique, here denoted as Range Ambiguity Suppression based on Blind Source Separation (RABSS). Section 4.1 explains the suggested two-stage strategy for effectively suppressing range ambiguities within multichannel SAR systems. The following section 4.2 elaborates, in detail, on the RABSS method which is implemented on the ground. The chapter concludes with final remarks in Section 4.3. Part of the material in this chapter has been published in [49].

4.1 Two-Stage Strategy

There are some suggested techniques to suppress range ambiguities in SAR, as discussed in Section 1.3 including their limitations. Nevertheless, the idea of employing a hybrid technique to suppress range ambiguities in spaceborne SAR systems with multiple elevation beams was first proposed in [46]. In this method, initially, scan-on-receive (SCORE) using the DBF technique is implemented on-board. Subsequently, range ambiguities are suppressed through the joint processing of signals collected by multiple elevation beams. This two-stage strategy is chosen because the on-board implementation of the DBF technique typically involves a trade-off between SNR and range ambiguities suppression, as discussed in Section 2.2.1. For instance, the mainlobe-constrained minimum variance distortionless response (MVDR) [39], [40], offers robust SNR even in the presence of errors that cause pattern mismatch, but this comes at the expense of range ambiguity performance. In contrast, sidelobe-constrained MVDR and linearly constrained minimum variance (LCMV) [41], [42], are designed to provide good range ambiguity suppression but at the cost of degrading the SNR. It is possible to combine MVDR and LCMV beamforming techniques, but this increases the complexity of the on-board hardware. Additionally, the presence of errors, especially non-deterministic errors as discussed in Section 2.2.2, remains an extremely challenging task in the context of range ambiguity suppression. Accordingly, DBF can be performed a posteriori on the ground as proposed in [119], [120], by downlinking the signals from all antenna elements. However, this will considerably increase the downlink capacity requirement.

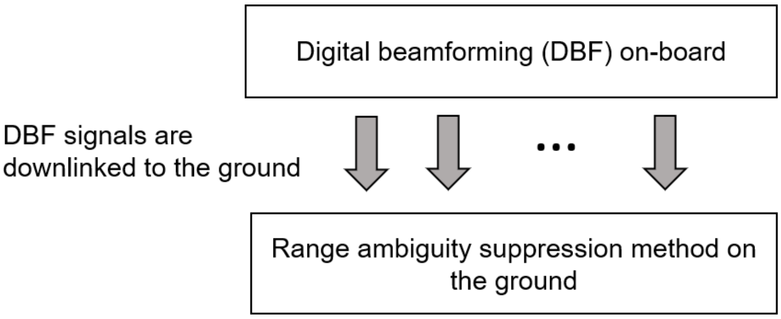

Figure 4.1: The simplified version of the two-stage strategy proposed for suppressing range ambiguity.

The two-stage strategy proposed in this thesis, illustrated in Figure 4.1, is expected to offer three main advantages. First, it reduces the on-board complexity required for effective range ambiguity suppression. Achieving perfect null steering on board typically requires complex hardware and also affects the system design, with the antenna height needing to be sufficiently high to achieve good null-steering. Second, a more effective and robust range ambiguity suppression is expected with this method, as it relies on downlinked data that accounts for all errors contributing to performance degradation, including non-deterministic errors that are difficult to overcome a priori. While deterministic errors may be anticipated and corrected with adjustments to the DBF setting on board, non-deterministic errors present a greater challenge. Third, the on-ground processing does not require a specific operational mode to be effective and can work under normal operational mode. This is an important advantage as many techniques require the SAR system to go into a specific calibration mode to measure the antenna pattern.

These expected advantages highlight the potential benefits of the proposed method, in which on-ground range ambiguity suppression technique will be further explained in subsequent sections and validated in Chapter 5.

4.2 Range Ambiguity Suppression On Ground

4.2.1 SAR Range Compressed Data

In the context of SAR, the various types of ground objects exhibit different level of Gaussianity [54]. Since the range ambiguity suppression method uses higher-order BSS as its main algorithm, these differences in Gaussianity are expected to affect the effectiveness of the method. In addition to Gaussianity, reciprocity also plays an important role to the success of applying the BSS technique as discussed in Section 3.1. Therefore, the proper selection of the type of data in a multichannel SAR system is the key to the success of applying the BSS technique. The different types of SAR data in the context of the Gaussianity and reciprocity properties will be discussed in this section.

Gaussianity is often not an issue if BSS is applied to a fully focused SAR image. In fact, focused SAR images can be divided into homogeneous, heterogeneous, and extremely heterogeneous regions, as described in [121], [122]. Heterogeneity directly implies non-Gaussianity, meaning that many regions in the fully focused SAR image have non-Gaussian statistics. However, the useful and the range-ambiguous signal are no longer reciprocal after the azimuth compression step due to the different azimuth frequency modulation (FM) rates between the useful and the range-ambiguous signal. The azimuth FM rate can be expressed as a function of slant range, as follows [9]:

$$K_a(R) = \frac{2 \cdot V_r^2}{\lambda \cdot R}, \tag{4.1}$$

where K_a denotes azimuth FM rate; λ is the wavelength; R is the minimum slant range as derived in (3.3); and V_r is the effective radar velocity, given by [9]

$$V_r \approx \sqrt{V_s \cdot V_g}, \tag{4.2}$$

where V_s and V_g are the platform and ground velocities, respectively.

Recalling the cocktail party problem illustrated by point target $Y \in \{O, P, Q, U\}$ as discussed in Section 3.1, the range-ambiguous and useful signal, as in (3.8) and (3.9) respectively, can, after azimuth compression, be written as follows for the target Q:

$$\begin{aligned} s''_{1,SA}(\tau, f_t) = \sigma_Q \cdot g''_1(\tau, f_t, Q) \cdot \operatorname{sinc}\left[B_\tau \left(\tau - \frac{2 \cdot (R_Q + \Delta RCM(f_t))}{c}\right)\right] \\ \cdot \exp\left(-j \cdot \frac{4 \cdot \pi}{\lambda} \cdot R_Q\right) \cdot \exp\left(-j \cdot \frac{\pi \cdot \lambda \cdot D_r \cdot f_t^2}{2 \cdot V_r^2}\right), \end{aligned} \tag{4.3}$$

$$
\begin{aligned}
s''_2(\tau, f_t) = \sigma_Q \cdot g''_2(\tau, f_t, Q) \cdot \operatorname{sinc}\left[B_\tau \left(\tau - \frac{2 \cdot R_Q}{c}\right)\right] \\
\cdot \exp\left(-j \cdot \frac{4 \cdot \pi}{\lambda} \cdot R_Q\right),
\end{aligned}
\tag{4.4}
$$

where D_r is the range distance of the ambiguity, here computed for $k = 1$; $\operatorname{sinc}[B_\tau(\cdot)]$ the range impulse response after range focusing; and the symbol $''$ is used to denote the signal after azimuth compression. According to (4.3) and (4.4), the strong ambiguity signal, $s''_{1,SA}$, is smeared along the azimuth due to the additional phase component and thus no longer reciprocal to the useful signal, s''_2. Additionally, the smearing also happens along the range due to the incorrect RCM correction, expressed by the residual range cell migration denoted to as ΔRCM in the range envelope, as shown later in (4.9). Due to this mismatch condition, the implementation in the focused image is no longer feasible as it violates the reciprocity between different signals at the ambiguity distance described in equation (3.14).

The reciprocity between signals, separated by the ambiguity distance, is still preserved in the range compressed domain:

$$
\begin{aligned}
s'_{1,SA}(\tau, f_t) = \sigma_Q \cdot g'_1(\tau, f_t, Q(f_t)) \cdot \operatorname{sinc}\left[B_\tau \left(\tau - \frac{2 \cdot R_Q(f_t)}{c}\right)\right] \\
\cdot \exp\left(-j \cdot \frac{4 \cdot \pi \cdot R_Q}{\lambda}\right) \cdot \exp\left(j \cdot \pi \cdot \frac{f_t^2}{K_a(R_Q)}\right),
\end{aligned}
\tag{4.5}
$$

$$
\begin{aligned}
s'_2(\tau, f_t) = \sigma_Q \cdot g'_2(\tau, f_t, Q(f_t)) \cdot \operatorname{sinc}\left[B_\tau \left(\tau - \frac{2 \cdot R_Q(f_t)}{c}\right)\right] \\
\cdot \exp\left(-j \cdot \frac{4 \cdot \pi \cdot R_Q}{\lambda}\right) \cdot \exp\left(j \cdot \pi \cdot \frac{f_t^2}{K_a(R_Q)}\right),
\end{aligned}
\tag{4.6}
$$

where the apostrophe $'$ is used to denote the range compressed domain, and $Q(f_t)$ represents Doppler-dependent target. In fact, (4.5) and (4.6) differ only by a complex constant:

$$
a'_{12}(\tau, f_t) = \frac{s'_{1,SA}}{s'_2} = \frac{g'_1(\tau, f_t, Q(f_t))}{g'_2(\tau, f_t, Q(f_t))}. \tag{4.7}
$$

Regarding statistics, the compression process makes range-compressed data more non-Gaussian than raw data. The range-compressed data have a higher deviation from Gaussianity compared to the raw data, due to the range compression, which amplifies the contrast differences among ground objects along the range direction. Therefore, applying BSS in the range-compressed domain is preferable to using raw data (due to the Gaussianity issue), as numerically analyzed in Section 3.3.2, or fully focused data (due to the mismatch with the reciprocity condition in the cocktail party equation).

However, there is a problem with range-compressed data that have already undergone range cell migration correction (RCMC), which is non-reciprocal between signals at the range ambiguity distance in the non-zero Doppler region. The range envelope of the range ambiguities is still a function of Doppler frequency due to incorrect range cell migration correction, while for the main signals it is already independent of Doppler frequency. This difference arises due to the different range migration profile between the desirable signal and the range ambiguity, which causes a mismatch during the chirp scaling process. This leads to a mismatch in the cocktail party equation, as illustrated in Figure 4.2. The uncorrected range cell migration of the range-ambiguous signal is called residual RCM.

Furthermore, the amount of total RCM to correct is derived in [9] and given by:

$$\Delta R(f_t, R) = \frac{\lambda^2 \cdot f_t^2 \cdot R}{8 \cdot V_r^2}, \tag{4.8}$$

where V_r is the effective radar velocity; R the minimum slant range to the imaged target. Since range ambiguities and useful signal are separated by distance $D_r(k)$ as written in (3.3), the residual RCM due to mismatch in the slant range is given by:

$$\Delta RCM(f_t) = \frac{\lambda^2 \cdot f_t^2 \cdot D_r(k)}{8 \cdot V_r}. \tag{4.9}$$

The case of the maximum RCM value happens when $f_{t,max} = B_t/2$, where B_t is the azimuth or Doppler bandwidth given by

$$B_t = V_r/\delta_{az}, \tag{4.10}$$

where δ_{az} denotes the azimuth resolution. Therefore, the total amount of RCM to correct is given the maximum amount of residual RCM

$$\Delta RCM_{max} = \frac{\lambda^2 \cdot D_r(k)}{32 \cdot \delta_{az}^2}. \tag{4.11}$$

As seen from (4.11), the primary parameters that determine the amount of the uncorrected residual RCM are the wavelength and the azimuth resolution (which is typically related to the physical size of the antenna). These two parameters are often related to each other, meaning that the longer wavelengths require larger antennas.

Table 4.1 presents a comparison between uncorrected RCM in X-band and L-band SAR systems. In X-band SAR, a computed $\Delta RCM_{max} = 0.6\,\delta_r$ is minimally affected by residual RCM. However, the issue is more pronounced in L-band systems with $\Delta RCM_{max} = 4.3\,\delta_r$. It is noted that the amount of residual RCM is measured relative to the range resolution cell, δ_r.

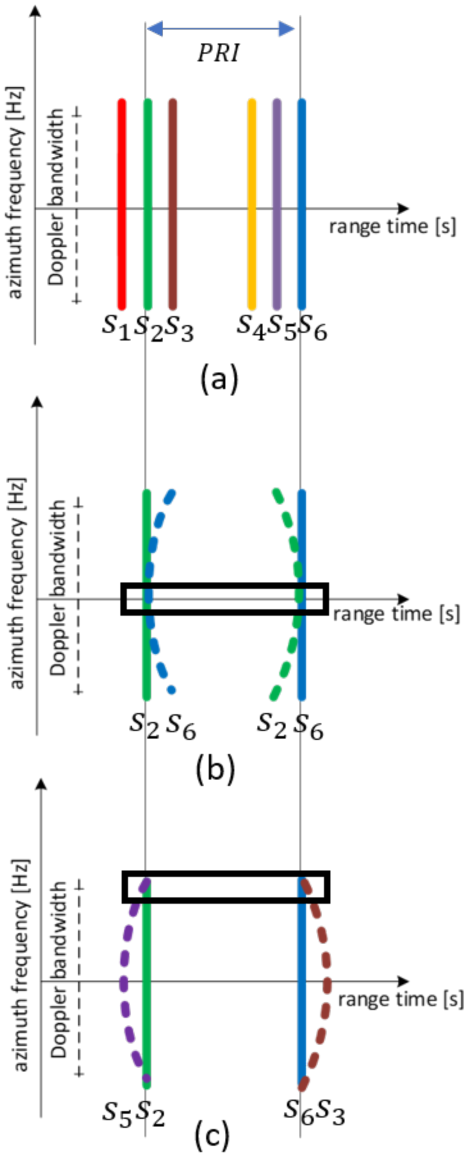

Figure 4.2: Violation of signal reciprocity after RCM correction. The useful and range ambiguous signals are denoted by solid and dotted curves, respectively. Left and right signals separated by the range ambiguity time PRI are indicated by the vertical lines. (a) six useful signals s_1-s_6 after RCM correction; (b) range ambiguity in zero Doppler (area inside the black box), the received signal is composed by $s_2 + s_6$; (c) range ambiguity in non-zero Doppler (area inside the black box), on the left the received signal is $s_5 + s_2$, while on the right, the received signal is $s_6 + s_3$.

To maintain reciprocity between signals, the range cell migration effect must be allowed to exist. Figure 4.3 shows multiple signals to illustrate reciprocity, where adjacent signals in the same beam are separated by a range resolution cell. The illustration in Figure 4.3 also clarifies the definition of a Doppler-dependant target, $Y(f_t), Y \in \{O, P, Q, U\}$, in Section 3.1.2. Here, for the same range bin, the reciprocal

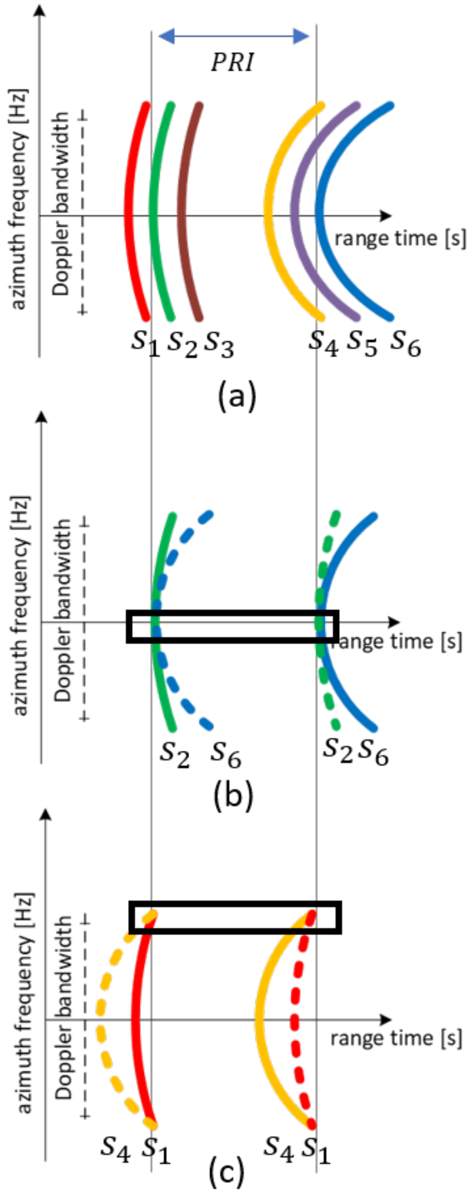

Figure 4.3: Reciprocity before RCM correction. Left and right signals separated by range ambiguity time PRI are indicated by the vertical lines. The useful and range ambiguous signals are denoted by solid and dotted curves, respectively. (a) six useful signals s_1-s_6 before RCM correction; (b) range ambiguity in zero Doppler (area inside the black box), received signal composed by $s_2 + s_6$; (c) range ambiguity in non-zero Doppler (area inside the black box), received signal is composed by $s_4 + s_1$.

signals are different for different Doppler locations. The different pairs of reciprocity along the Doppler direction lead to different mixing ratios, such as a_{26} between s_2

Table 4.1: Amount of uncorrected RCM in the referenced X- and L-band spaceborne SAR systems

Parameter	X-band	L-band
Wavelength λ	3 cm	23 cm
Antenna length L	4.8 m	15 m
PRF	3300 Hz	2700 Hz
Ambiguity order k	4	4
Azimuth resolution δ_a	2.4 m	7.5 m
Range resolution δ_r	1.5 m	1.5 m
Max. residual RCM ΔRCM_{max}	0.6 δ_r	4.3 δ_r

and s_6 at zero Doppler and a_{14} between s_1 and s_4 at non-zero Doppler [1]. Due to the changing mixing ratio values along the Doppler frequency, which result from different pairs of reciprocity, an optimization approach called azimuth sub-band decomposition is necessary and will be discussed in the following section.

4.2.2 Stacking Approach

The implementation of BSS alone, without additional optimization strategies, is not expected to lead to satisfactory RASR performance. This constraint primarily arises from accurate estimation of fourth-order cumulants when dealing with the limited sample data [123]. It is worth highlighting that the effectiveness of BSS strongly depends on accurate estimation of the fourth-order cumulants. Therefore, it becomes essential to employ suitable approaches, such as the stacking approach in this case.

As discussed in Section 3.2, the source signal needs to be non-Gaussian, where its Gaussianity is measured by fourth-order cumulants, in order for HO BSS to perform well. Therefore, the accurate estimation of source signals also means the accurate estimation of fourth-order cumulants. In order accurately estimate the fourth-order cumulants, a greater number of samples is necessary, especially when the data tend to have a Gaussian distribution [123]. Furthermore, it is shown later in Chapter 5 that the non-Gaussian characteristic of the range-compressed data is not very pronounced (as compared to the image data). Consequently, accumulating as many

---

[1] The main purpose of Figure 4.2 and Figure 4.3 is to visually assess the signal's reciprocity principle, which is of significant importance for the BSS technique. To ensure a fair assessment, a comparison is conducted using the same range-bin reference for both Figure 4.2 and Figure 4.3, despite the fact that the signals in Figure 4.2(c) and Figure 4.3(c) are different due to the presence of the RCM effect.

samples as feasible becomes preferable when anticipating data that lack strong non-Gaussian traits.

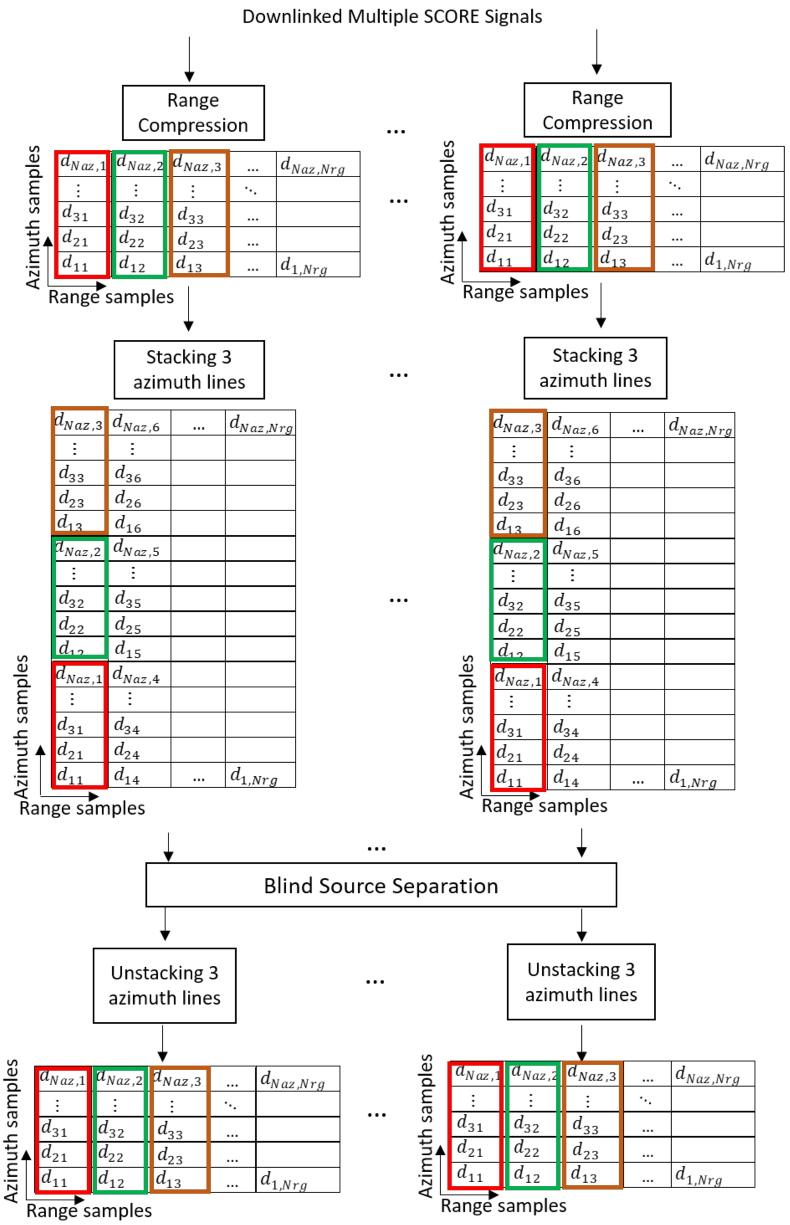

Figure 4.4: An example of the stacking approach for the number of stacked azimuth lines $N_{sta} = 3$.

In the case of a short acquisition SAR data, the stacking approach, which aggregates correlated time-series data, holds significant importance as it provides a larger number of samples. Stated differently, the Stacking approach serves as a suitable approach for acquiring supplementary samples from the constrained azimuthal extension. The operation involves concatenating along azimuth multiple segments of correlated time-series of the data to create a longer time-series data. The stacking is performed as follows:

$$D_{N_a \times N_r} \rightarrow D_{N_{sta} N_a \times N_r / N_{sta}}, \tag{4.12}$$

where $D_{N_a \times N_r}$ represents the input data.The approach involves stacking N_{sta} azimuth lines, such that N_r/N_{sta} is an integer number, and moving the entire azimuth line rather than only one range sample. Note that when $N_{sta} = 1$, an azimuth line corresponds to a range sample. For a better illustration, an example of the stacking procedure is presented in Figure 4.4.

It is worth noting that the estimated mixing matrix $\hat{\mathbf{A}}$ should have N_r different values, since the mixing matrix $\mathbf{A}$ is dependent on the range. However, reducing the input range samples to N_r/N_{sta} means that the estimated mixing matrix $\hat{\mathbf{A}}$ only has N_r/N_{sta} different values, resulting in an underestimation of the solution. This implies that the number of unique values in $\hat{\mathbf{A}}$ along the range is less than the dimension of the actual matrix $\mathbf{A}$. Thus, as the number of stacked azimuth lines N_{sta} increases, the problem of underestimation of the solution becomes more severe, and this can potentially degrade the performance.

The optimal number of stacked azimuth lines, N_{sta}, must be determined through empirical evaluation as it involves a trade-off between the contradictory requirements previously discussed. On one hand, increasing N_{sta} can enhance the robustness of the BSS method, while on the other hand, a lower N_{sta} is preferred to avoid an underestimated solution. The details of this empirical analysis will be presented in Chapter 5, which covers simulation and analysis.

4.2.3 Azimuth Sub-band Decomposition Approach

The estimation of the mixing matrix $\mathbf{A}$ is complicated by the fact that its value is non-stationary along the Doppler direction, i.e., Doppler dependent, as expressed in (3.14). Additionally, the presence of range cell migration leads to different reciprocity configurations along the Doppler direction, as discussed in the previous sections. Therefore, it is necessary to find a suitable solution that takes these factors into account. The main idea behind the azimuth sub-band decomposition approach is to decompose the signals into several Doppler sub-bands and apply the BSS to each sub-band signal. This approach allows for a Doppler-dependent solution to the problem of estimating the mixing matrix. Additionally, by breaking down the data into smaller sub-bands, it becomes possible to isolate the varying range cell migrations and reciprocity issues and apply BSS to each sub-band, which improves the overall accuracy of the solution.

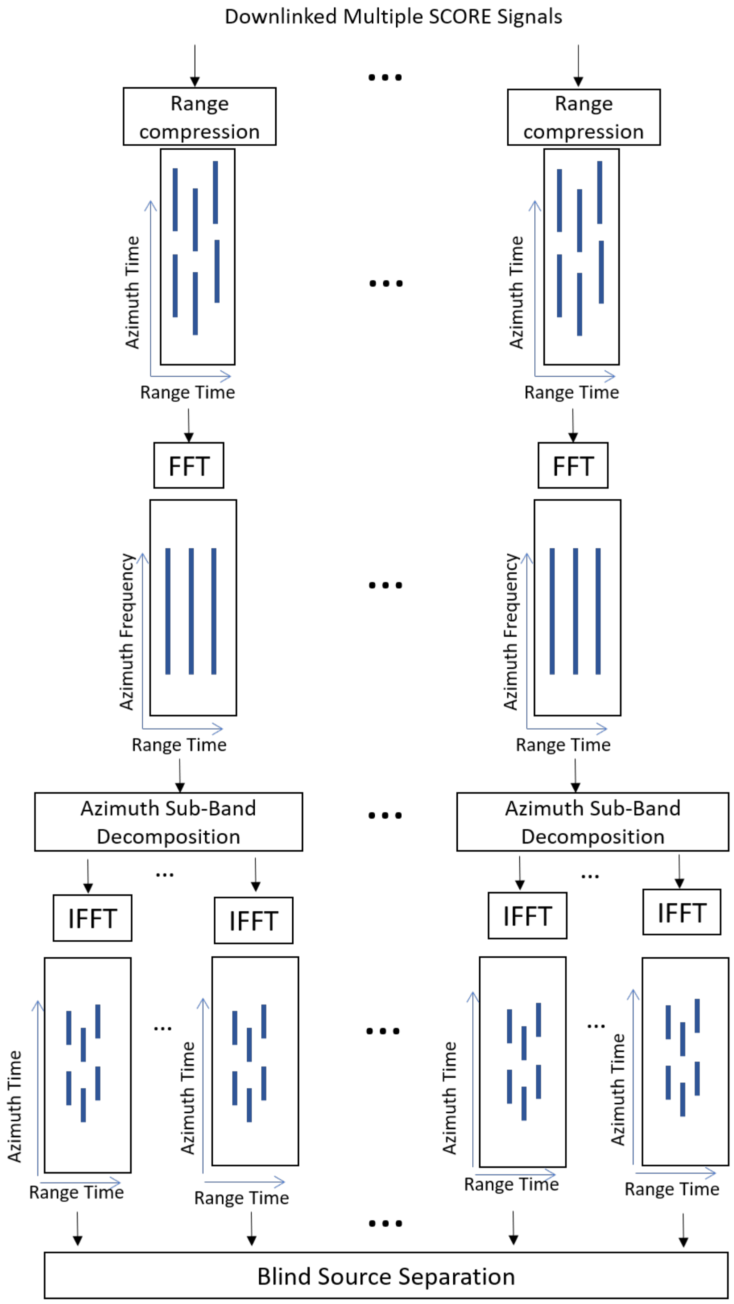

Figure 4.5: Flowchart of the azimuth sub-band decomposition approach.

In the higher-order BSS, the non-Gaussianity of the source signals is exploited to separate the mixed signals. In general, the non-Gaussianity of a signal is higher in the time domain than in the frequency domain. This is because the time domain representation of a signal captures the temporal dynamics of the signal, which can result in non-Gaussian distributions due to the presence of transients, edges, and other non-stationary features. In contrast, the frequency domain representation of a signal provides a more stationary representation of the signal by separating the signal into frequency components. This can result in a smoother distribution that is closer to Gaussian. Therefore, after decomposing the data into several Doppler sub-bands, the data need to be transformed back into the time domain before the BSS method is applied. After the BSS method is applied, the sub-bands will be combined again to obtain the full Doppler band. The overall step for this approach can be seen in Figure 4.5.

Performing azimuth sub-band decomposition can negatively impact the performance of BSS because the sub-band data has a reduced bandwidth compared to the original data, leading to an increase in Gaussianity. The impact of the reduced bandwidth on the Gaussianity level is numerically presented in Section 5.2. Therefore, there is a trade-off between the benefit of having a Doppler-dependent solution that takes into account the Doppler-dependency of mixing matrix and range cell migrations, and the degradation in performance caused by reduced bandwidth. Therefore, the number of considered Doppler sub-bands, N_{sub}, must be optimized through empirical analysis, taking into account the contradicting requirements previously discussed: on one hand, N_{sub} shall be high to account for the Doppler-dependent variations and RCM as mentioned earlier; on the other hand, N_{sub} must be low to maintain the high bandwidth. The empirical analysis to determine the optimal N_{sub} will be presented in the simulation and analysis chapter (Chapter 5).

Finally, it is worth mentioning that while azimuth sub-band decomposition has a trade-off impact, range sub-band decomposition has only a negative impact, i.e., an increase in Gaussianity due to the reduced bandwidth. Therefore, the range sub-band decomposition approach is not proposed in this thesis.

4.3 Remarks

The approaches discussed in the previous section have led to the proposal of a full processing step of the RABSS method, which is depicted in Figure 4.6. To begin with, it is recommended that the BSS algorithm be applied to the range compressed data rather than the raw data or fully focused data. This is because the range compressed data have a stronger non-Gaussian distribution than the raw data, making them better suited for BSS. Furthermore, fully focused data are not considered suitable for BSS due to the reciprocity issue, where the range ambiguity is smeared in the focused data.

It is crucial to apply the proposed method before the RCM correction due to its effect on the Doppler shift and range ambiguity of the data. As a result, the BSS algorithm should be applied to the data before RCM correction is performed. It is worth noting that the SAR processing used in this paper is the extended chirp scaling (ECS) algorithm [57], where RCM correction is typically performed in the raw data. Therefore, since the BSS algorithm is applied in the range-compressed data without RCM correction to maintain the reciprocity properties, the chirp scaling and

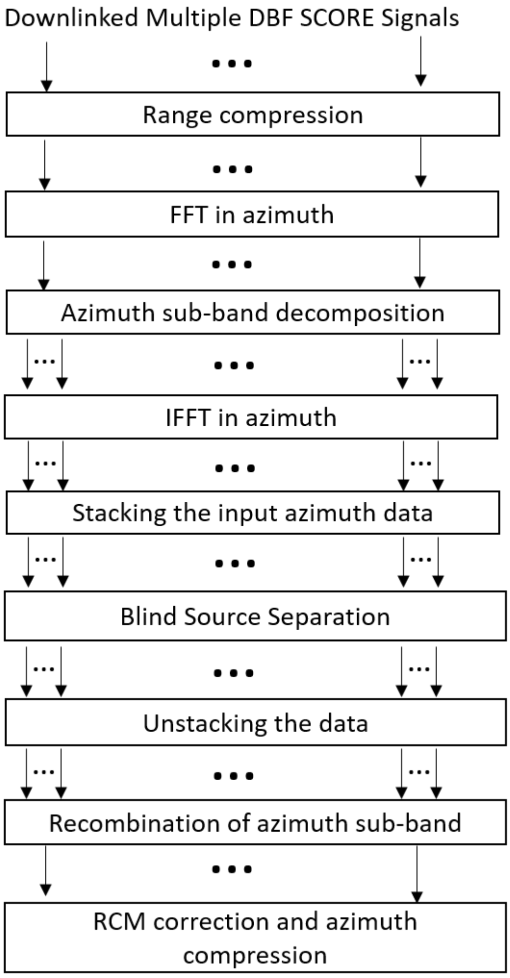

Figure 4.6: Flowchart of the Range Ambiguity Suppression based on Blind Source Separation (RABSS) method.

bulk RCM correction steps, as suggested by the ECS algorithm described in Section 2.1.2, are excluded when generating range-compressed data used as the input of BSS. However, in a system where there is no residual RCM or it is negligible, i.e., there is no reciprocity issue after RCM correction, the chirp scaling and bulk RCM correction can be applied before the BSS algorithm is applied.

The sub-band decomposition is performed to overcome the Doppler-dependent range ambiguity. This helps to separate sources with different Doppler shifts. Following the sub-band decomposition, the data are transformed into the time domain since this is the selected domain. Furthermore, to improve performance, the data undergo a stacking approach step where a number of azimuth lines are stacked together. Finally, recombination of azimuth sub-bands is performed to recover the full bandwidth of the data. This results in a comprehensive processing method that can be used for effective source separation in SAR images.

The RABSS method illustrated in Figure 4.6 does not specify the optimal number of azimuth lines that need to be stacked, denoted by N_{sta}, or the number of Doppler sub-bands that need to be formed, denoted by N_{sub}. This is because these parameters depend on the specific SAR system and require empirical analysis to be determined. It is important to note that different SAR systems correspond to different mixing matrix characteristic. For instance, the optimal values for a planar antenna SAR system, resulting in a range-dependent mixing matrix, will likely differ from those for an array-fed reflector antenna SAR system, leading to a range- and Doppler-dependent mixing matrix. Therefore, in addition to presenting simulations of the proposed method for a multichannel SAR system, the next sections will also demonstrate the empirical analysis for different SAR systems, specifically for planar and array-fed reflector antennas. This will allow for a more comprehensive understanding of how to optimize the RABSS method for a range of different SAR systems.

5 Simulation and Analysis

The goal of this chapter is to provide simulation examples which illustrate the application of the Range Ambiguity Suppression based on Blind Source Separation (RABSS) method for different antenna systems. As of now, operational spaceborne SAR systems do not utilize multiple elevation Rx beams. The NASA/ISRO NISAR mission, with a planned launch date in 2025, will be the first spaceborne SAR system to use multiple elevation Rx beams. Accordingly, it is essential to develop a realistic simulation of a multichannel SAR system that incorporates multiple Rx beams to generate a HRWS SAR image. It is important to note that the proposed method is designed to operate on heterogeneous scenes rather than point targets. The reason for implementing the RABSS method on heterogeneous scenes is rooted in its nature of exploiting the statistics of the input signals. The system simulator will be presented in detail in Section 5.1, describing the simulation steps used to generate HRWS data, in this case as a result of multiple elevation Rx beams.

Considering the existence of various SAR systems, each corresponding to a distinct antenna pattern model used for data acquisition, the RABSS method will be applied. Section 5.2 will implement the RABSS method in a simulated multichannel SAR system with a mixing matrix whose values are separable in both range-time and Doppler frequency. In real SAR systems, this is an oversimplified assumption even when a fixed beam, i.e., no scan-on-receive (SCORE), is implemented, because the model in the fixed beam SAR system still results in a mixing matrix with range dependency. However, the analysis of this simple mixing matrix model is necessary to establish a fundamental empirical understanding of the proposed method.

In the following sections, the RABSS method will be applied to multichannel SAR systems with SCORE. Section 5.3 will present the implementation in a multichannel SAR system that uses a planar antenna. Such a system typically has a range-dependent mixing matrix due to the SCORE implementation. This will be followed by the implementation in an array-fed reflector multichannel SAR system with SCORE in Section 5.4. Due to the fact that the antenna patterns in an array-fed reflector are non-separable in azimuth and elevation, the mixing matrix's values are not only range-dependent but also Doppler-dependent. Lastly, Section 5.5 will draw conclusions and provide final remarks on the chapter's findings. Part of the material in this chapter has been published in [48], [49].

5.1 Simulation Procedure

The aim of the simulator is to simulate range-ambiguous multichannel SAR data resulting from multiple Rx beams acquisition using the digital beamforming (DBF) technique. As the thesis primarily focuses on a data-based method, it is crucial to ensure accurate representation of the received data. Range ambiguities primarily arise due to the sidelobes of the antenna pattern, which contains 2-D information represented not only along range but also along the Doppler frequency. The main challenge lies in combining the 2-D pattern and SAR data to produce 2-D range-ambiguous SAR data, which will be presented in this section.

The simulator utilized in this thesis takes a SAR image as input. Specifically, the simulator takes an X-band image from the TerraSAR-X mission [112] as the backscatter, and the output are L-band range-ambiguous raw data. Consequently, all the chirp signals (range and azimuth) involved in this simulator follow the L-band properties.

As TerraSAR-X operates as a single-beam SAR, simulating HRWS SAR system which utilizes multiple elevation beams, while introducing range ambiguity, proves to be a challenging task. Therefore, the primary focus of this simulator is to develop a reliable process that can effectively generate HRWS data while maintaining geometric accuracy, despite using a single-beam SAR image as input.

The second challenge arises from the range cell migration (RCM) as the radar moves in relation to the target [9]. Specifically, the elevation angle undergoes slight changes during the synthetic aperture time (or as a function of Doppler frequency), resulting in a target observation pattern that has two varying parameters (range and azimuth). Incorporating the range cell migration effect into the range ambiguity concept proves to be a tricky task, particularly when considering that the DBF pattern must also be incorporated.

The algorithm utilized for reverse processing the SAR data in this thesis is the extended chirp scaling (ECS) algorithm [57], as presented in Section 2.1.2. The ECS algorithm is selected due to its more accurate RCM correction (RCMC) compared to other algorithms. The simulation, as shown in Figure 5.1, commences by using a SAR image as the input. The initial step involves generating range-compressed data by performing reverse SAR processing. This requires transforming the input SAR image into the range-time and azimuth frequency domains, which is then multiplied with the conjugate of the phase function of azimuth chirp in frequency, as defined in (2.16), $H_{az}^{*}(f_t)$.

It is worth to remark that in the real acquisition process, the DBF weights are applied to the raw data of the received channels. However, for the sake of verifying the accuracy of the estimated mixing matrix, which is derived from the DBF pattern, the DBF pattern is generated independently of the raw data in this simulation. The

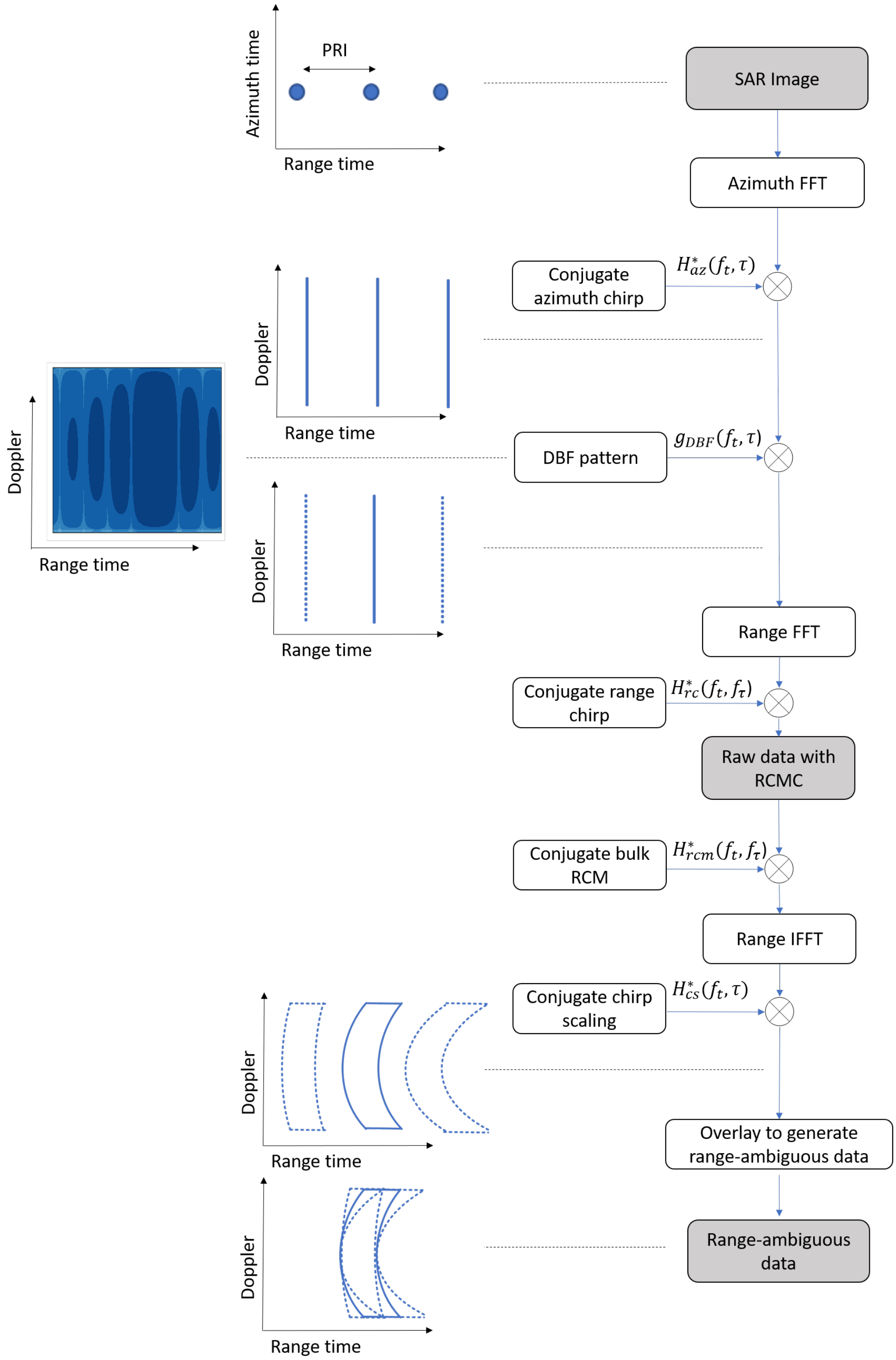

Figure 5.1: Flowchart illustrating the process of generating range-ambiguous raw data for a single swath (right), including the target's response representation (left). On the left, the useful target and the range-ambiguous target are represented by solid and dashed curves, respectively.

process of incorporating the DBF pattern into the simulated data is considered an approximation in this simulation, as it does not account for the curved-Earth effect and instead assumes a flat-Earth geometry. Furthermore, the incorporation of the DBF pattern into the range-compressed data is due to the fact that the RABSS method, which also aims to estimate the mixing matrix, is applied to the range-compressed data. Consequently, pulse extension effect is neglected here.

In general, pulse extension deserves further investigation regarding its impact on range ambiguity. However, in cases where beamforming in elevation is designed to provide nulls in the direction of range-ambiguous signals (i.e., null steering), pulse extension results in higher level of the intensity of the received ambiguities, thus worsening range ambiguity suppression, as discussed in [41]. Furthermore, the joint effect of pulse extension and topographic errors, in the case of null steering, may degrade range ambiguity suppression performance, as indicated in [124]. Despite this, high range ambiguity is favorable for the RABSS method, as BSS works better in cases of high range ambiguity, as discussed in Section 3.3.6. Thus, for RABSS method, consideration of pulse extension loss in the case of null steering would actually be expected to result in greater range ambiguity suppression.

Regarding the simulation for the multiple-elevation DBF beam, since there will be three different scenarios - planar antenna with fixed beams, planar antenna with SCORE, array-fed reflector antenna with SCORE - and each scenario has a different procedure for generating multiple-elevation DBF beams, the simulation to generate the DBF antenna will be explained at the beginning of each section.

After obtaining the range-compressed data and multiple-elevation DBF beams, the next step in the simulation process incorporates the DBF antenna pattern into the SAR data, resulting in weighted DBF SAR data, given by

$$s'_w(\tau, f_t) = g_{DBF}(\tau, f_t) \cdot s'(\tau, f_t), \tag{5.1}$$

where $s'(\tau, f_t)$ denotes range-compressed data and $g_{DBF}(\tau, f_t)$ the complex-value DBF pattern.

In the process of generating the range ambiguous signal for the simulator, it is essential to carefully consider the effect of RCM on the signal. This requires simulating the proper footprint of the signal in the range and azimuth direction. The function $s'_w(\tau, f_t)$ does not yet account for the effect of RCM. Since the SAR processing algorithm used in this simulator is the ECS, RCM processing is done on the raw data.

To obtain the raw data, the range-compressed data in the frequency domain are multiplied with the conjugate of the phase function of the range chirp in frequency, as defined in (2.13), $H^*_{rc}(f_t, f_\tau)$. After obtaining the raw data, the next step is to introduce the effect of RCM. This can be done by multiplying the data with the conjugate of the phase function of bulk RCM, as defined in (2.12), $H^*_{rcm}(f_t, f_\tau)$, and afterwards, multiplying the data in the range-Doppler domain with the conjugate of the phase function of the chirp scaling, as defined in (2.8), $H^*_{cs}(f_t, \tau)$.

Finally, the range ambiguous signal in the range-Doppler domain is obtained as

$$x(\tau, f_t) = \sum_k s_k(\tau, f_t, \theta_k), \tag{5.2}$$

where the summation index k refers to range ambiguity signals ($k \neq 0$), superimposing the useful signal ($k = 0$); the range time interval is $0 < \tau < T_r$ where T_r is the pulse length; and the azimuth frequency is f_t where $-PRF/2 < f_t < PRF/2$.

5.2 Range- and Doppler-Independent Mixing Matrix

The analysis of a scenario with a range- and Doppler-independent mixing matrix, despite unrealistic in a real SAR system, is essential to establish a fundamental empirical understanding of the RABSS method. This includes not only blind source separation but also the proposed optimization strategies, such as stacking azimuth lines and azimuth sub-band decomposition. This is due to the fact that, as demonstrated in Section 3.3, relying solely on BSS to overcome the range ambiguities issue in SAR is ineffective due to several previously discussed factors. Therefore, the optimization technique needs to be investigated, irrespective of the dependency of the mixing matrix on range-time and Doppler.

Table 5.1 presents the parameters of the reference system, which are identical to Tandem-L [40] with some parameter differences to emphasize the effect of range ambiguity. Furthermore, the SAR input data are generated using the simulator, which includes a range-compressed and range-ambiguous raw data module as described in the previous section. When discussing the geometry of the simulated HRWS data concerning the simulation parameters in Table 5.1, it is worth pointing out that in the ideal case, the HRWS SAR image would contain a significantly higher number of samples compared to the SAR input image used in this simulation, which in this case is the TerraSAR-X image. In range, the width of each subswath is determined by $c \cdot PRI/2 - c \cdot T_r$, where $c \cdot T_r$ refers to the blind range caused by Tx activity. The resulting width for each subswath is 46 km. To avoid border effects during the generation of raw data for the corresponding image, the width of each subswath is further extended by the pulse duration on both the left and right sides, resulting in a total width of 67 km, including the extensions. In this simulator, due to the limited availability of SAR image data, only a 7.1 km segment for each subswath,

Table 5.1: Simulation parameters of generated SAR data.

Parameter	Symbol	Value
Orbit height	h_{orbit}	628 km
Swath minimum / maximum look angle	$\theta_{min}/\theta_{max}$	26.3 / 46.9 deg
Platform velocity	V_s	7542 m/s
Elevation tilt angle w.r.t. nadir	θ_{tilt}	36 deg
Center frequency	f_0	1.26 GHz
Pulse repetition frequency	PRF	2700 Hz
Sampling frequency	f_s	45.6 MHz
Chirp bandwidth	B_τ	38 MHz
Pulse duration	T_r	30 μs
Number of simultaneous elevation beams	N	5
Elevation beamforming algorithm	-	n.a.
Processed Doppler bandwidth	$B_{t,proc}$	1348 MHz
Signal-to-noise ratio	SNR	10 dB
Range resolution	δ_r	4 m
Azimuth resolution	δ_a	5 m
Maximum RCM value	ΔR_{max}	16 δ_r

excluding the extension, is simulated. This approach is taken to address the geometrical constraints in achieving the geometry of the intended multiple swaths of the L-band SAR system. Finally, it is essential to note that each subswath is simulated and processed individually. Therefore, there will be a range discontinuity between sub-swaths since only a smaller segment of each subswath is simulated.

In azimuth, the simulated system exhibits an azimuth oversampling ratio (PRF/B_t) of 2 to avoid Doppler ambiguity. It is noted that a system like Tandem-L [40] has a higher oversampling ratio of 2.3 (for dual-pol) due to the use of a staggered PRI, which requires higher sampling for the recovery of missing samples.

The value of the mixing matrix $\mathbf{A}_{HIGH}$ in the case of a range- and Doppler-independent mixing matrix is selected in a way that its off-diagonal elements' values are relatively high as compared to the diagonal elements. It is important to note that, as outlined in Section 3.1, the mixing matrix is derived from the DBF antenna pattern.

$$\mathbf{A}_{HIGH}(\tau, f_t) = \begin{bmatrix} 1 & 0.3+0.3j & 0.23+0.11j & 0.17+0.15j & 0.2+0.1j \\ 0.2+0.2j & 1 & 0.32+0.21j & 0.23+0.1j & 0.18+0.15j \\ 0.23+0.21j & 0.3+0.2j & 1 & 0.2+0.1j & 0.15+0.09j] \\ 0.17+0.15j & 0.23+0.11j & 0.3+0.2j & 1 & 0.1+0.3j \\ 0.2+0.1j & 0.17+0.15j & 0.23+0.11j & 0.3+0.2j & 1 \end{bmatrix}. \tag{5.3}$$

As seen in (5.3), the values of $\mathbf{A}_{HIGH}$ are independent of both range time and Doppler frequency. Figure 5.2 illustrates the two-dimensional representation of the mixing matrix.

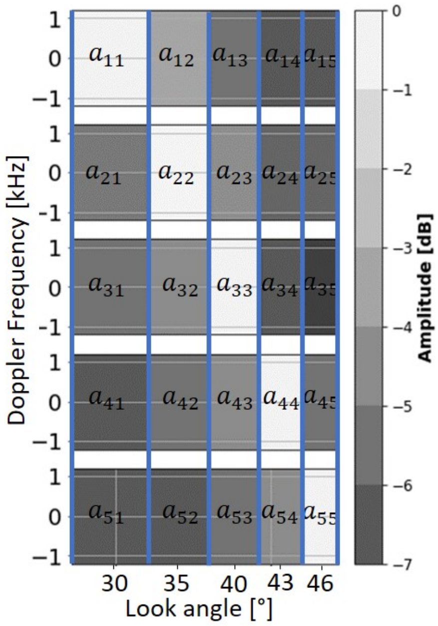

Figure 5.2: Mixing matrix, $\mathbf{A}_{HIGH}$, which contains a range-and Doppler-independent value within each swath. The blue vertical lines indicate the boundary between the simulated swath segments.

Figure 5.3 shows the SAR data at different stages of reverse processing represented as raw data, range-compressed data with curvature (before RCMC), range-compressed data without curvature (after RCMC), and focused data. These representations are provided as examples to illustrate that the various types of data will be discussed, aiming to analyze the issues of Gaussianity and reciprocity concerning the performance of the BSS method.

It is noted that the Gaussianity level is measured by the complex signal kurtosis (CSK), as defined in Section 3.3.1, and the obtained CSK results are reported in Table 5.2. Furthermore, various SAR data types are simulated, with a specific index assigned to each data type, as shown in Table 5.2. It can be seen that the RCM correction makes the data, both raw (III) and range-compressed (V), more Gaussian as compared to when RCM is not corrected (IV and VI). This is due to the fact that the presence of curvatures increase the heterogeneity of the data. Furthermore, due to the compression process, raw data (III and IV) are more Gaussian than the range-compressed data (V and VI), while the focused SAR image is significantly more non-Gaussian (VII). Additionally, the range-compressed data in the Doppler domain (II)

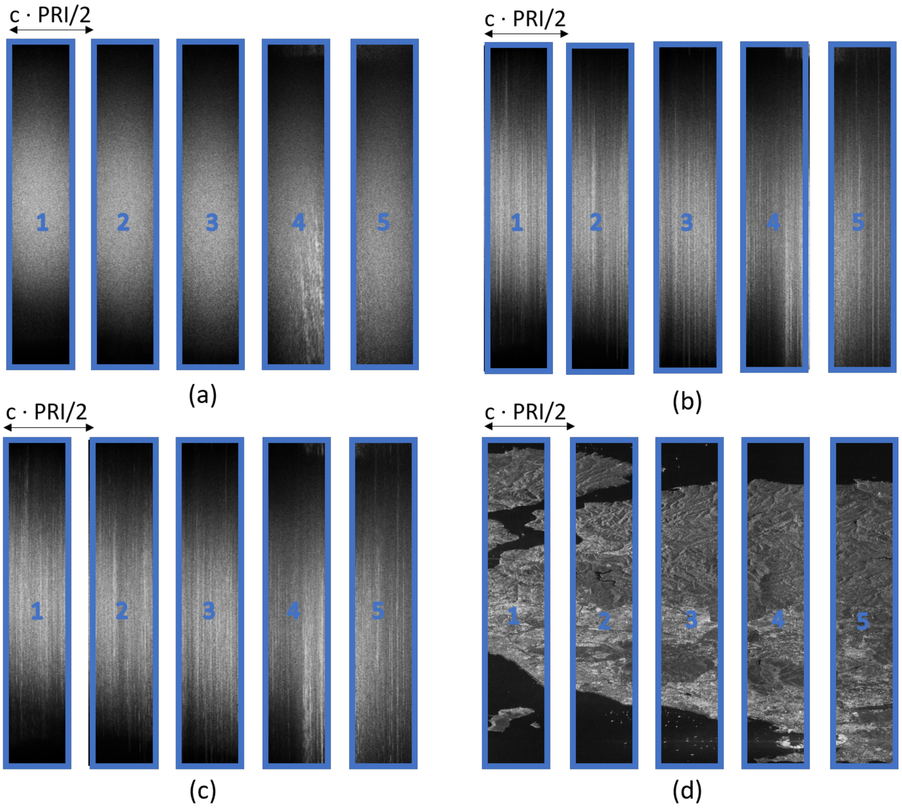

Figure 5.3: Simulated L-band SAR data from TerraSAR-X [112] image for five range segments in range (horizontal) and azimuth (vertical). (a) raw data; (b) range compressed data without curvature; (c) range compressed data with curvature; (d) focused SAR image.

are considerably more Gaussian than the range-compressed data in the azimuth-time domain (V) due to the fact that the time-domain representation of a signal captures the temporal dynamics of the signal, which can result in non-Gaussian distributions due to the presence of transients, edges, and other non-stationary features. The Doppler bandwidth reduction lead to a more Gaussian data, as shown by the lower CSK value of the range-compressed data with reduced Doppler bandwidth (VIII).

Figure 5.4 demonstrates the performance of the BSS method in a case of mixing with $\mathbf{A}_{HIGH}$ across various data types: simulated received raw data (with (IV) and without curvature (III)), range-compressed data (with (VI) and without curvature (V)), range-compressed data in the range-Doppler domain (II), and the focused SAR image (VII). Specifically, it shows the RASR calculated using (3.39) for the simulated SAR image after applying the BSS method, comparing it with the RASR of the received simulated SAR image.

From Figure 5.4(a)-(d), it is evident that the BSS method performs better on (raw and range-compressed) data with curvature (IV and VI) than on data without curvature (III and V). Notably, the BSS method fails when applied to the focused SAR

Table 5.2: Table of index and complex signal kurtosis (CSK) for different kinds of SAR data.

Index	Type of SAR Data	Domain	CSK
I	Raw data with curvature	Range-time, Doppler	0.43
II	Range compressed with curvature	Range-time, Doppler	0.83
III	Raw data without curvature	Time	1.0
IV	Raw data with curvature	Time	1.6
V	Range compressed without curvature	Time	1.71
VI	Range compressed with curvature	Time	1.96
VII	Fully focused data	Time	8.41
VIII	Range compressed with 30% Doppler bandwidth, with curvature	Time	1.15

image (VII), depicted in Figure 5.4(f). This failure is attributed to the violation of reciprocity after curvature correction and azimuth focusing, as discussed in Chapter 4.

To understand the combined impact of reciprocity and Gaussianity on BSS performance, it is helpful to relate Figure 5.4 with Table 5.2. Figure 5.4(b) and (c) highlight that reciprocity might have a more significant effect than Gaussianity. Although the raw data with curvature (IV, in Figure 5.4(b)) exhibit higher Gaussianity compared to the range-compressed data without curvature (VI, in Figure 5.4 (c)), indicated by the lower CSK value in Table 5.2 (1.6 vs 1.71), the applied BSS method still results in better RASR suppression. However, with curvature, the BSS method achieves better performance on the range-compressed data (VI) rather than on the raw data (IV), as depicted in Figure 5.4 (b) and (d). This difference can be attributed to the lower Gaussianity of the range-compressed data compared to the raw data (CSK of 1.96 vs 1.6).

Figure 5.4 (e) illustrates a degradation in performance in the range-Doppler domain (II) due to the high Gaussianity level (CSK = 0.83) compared to the time domain (VI) (see Table 5.2). Overall, Figure 5.4 suggests that the best RASR suppression is achieved from the range-compressed data with curvature (VI). From now, the performance analysis for the remaining part of the thesis refers specifically to the range-compressed data with curvature (VI).

It is worth noting that the results presented in Figure 5.4 were obtained from simulations using A_{HIGH}, which produced an average RASR value of -6.4 dB. However, this may not be a realistic scenario in cases where on-board DBF processing is employed to suppress range ambiguities. In such a scenario, the RASR value is typically

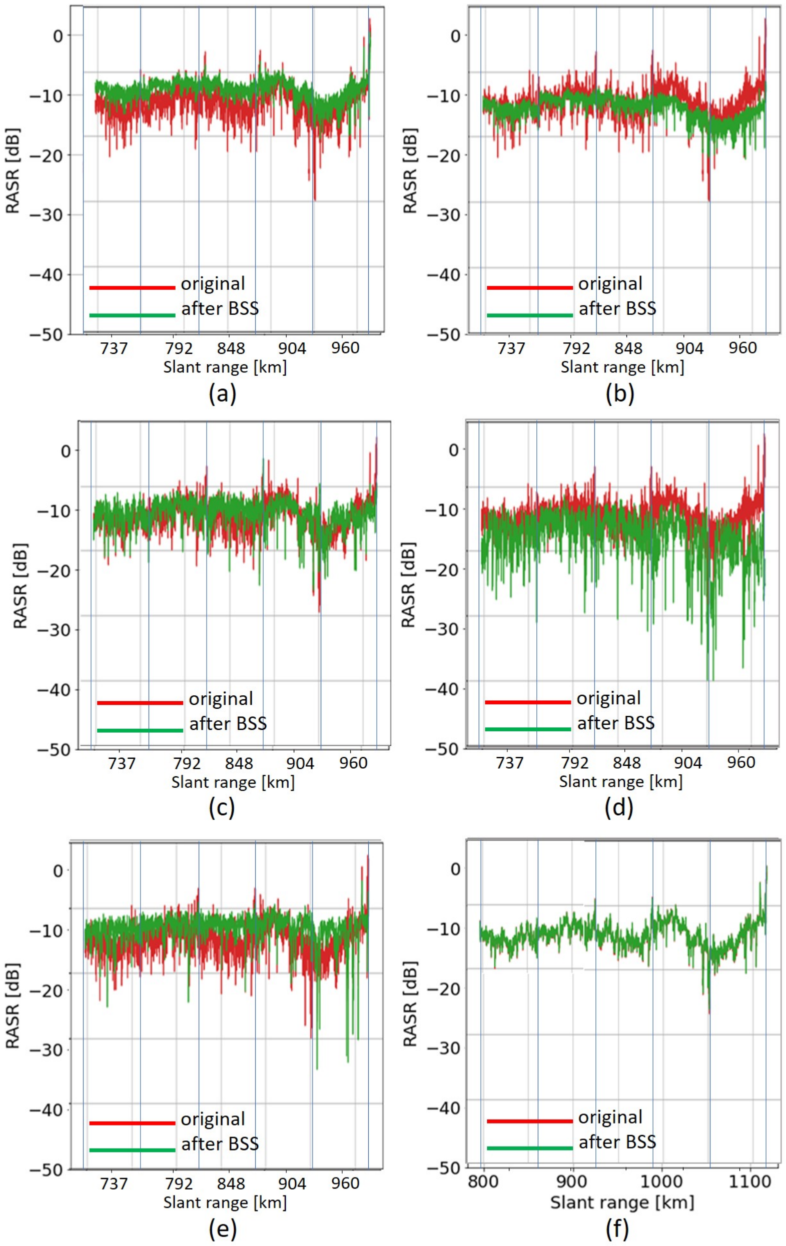

Figure 5.4: RASR performance for input SAR data simulated using $\mathbf{A}_{HIGH}$. The BSS is applied to different SAR data domains: (a) raw data without curvature (III, CSK=1.0); (b) raw data with curvature (IV, CSK=1.6); (c) range compressed data without curvature (V, CSK=1.71); (d) range compressed data with curvature (VI, CSK=1.96); (e) Range compressed in range-Doppler domain with curvature (II, CSK=0.83); (f) focused SAR image (VII, CSK=8.41). The blue vertical lines indicate the boundary between the simulated swath segments. The red curve shows the RASR for the original simulated SAR image; the green curve shows the RASR for the ambiguity-suppressed image (after applying the BSS method). In (f), the red curve is covered by the green curve.

significantly lower than -6.4 dB. Thus, the next simulation is conducted using lower off-diagonal values in the mixing matrix, as given by:

$$\mathbf{A}_{LOW}(\tau, f_t) = \begin{bmatrix} 1 & 0.06+0.03j & 0.04+0.03j & 0.02+0.01j & 0.01+0.01j \\ 0.06+0.06j & 1 & 0.05+0.04j & 0.04+0.03j & 0.03+0.03j \\ 0.07+0.06j & 0.08+0.06j & 1 & 0.06+0.03j & 0.04+0.03j \\ 0.05+0.04j & 0.07+0.03j & 0.08+0.06j & 1 & 0.03+0.08j \\ 0.06+0.04j & 0.08+0.07j & 0.08+0.08j & 0.11+0.11j & 1 \end{bmatrix}. \tag{5.4}$$

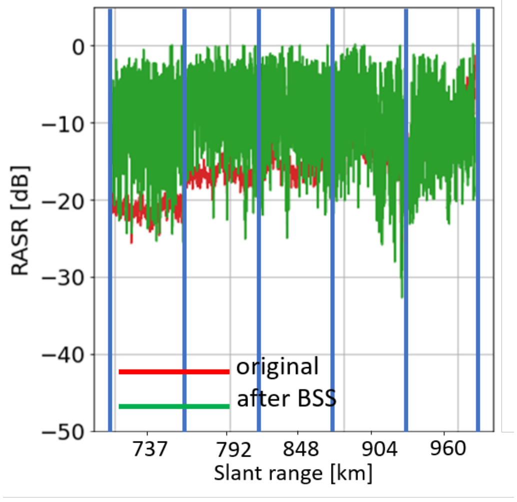

Figure 5.5: RASR performance for input SAR data simulated using $\mathbf{A}_{LOW}$. The BSS method is applied to range-compressed data with RCM. The blue vertical lines indicate the boundary between the simulated swath segments. The red curve shows the RASR for the original simulated SAR image; the green curve the RASR for the ambiguity-suppressed image after applying the BSS method.

The mixing matrix $\mathbf{A}_{LOW}$ defined in equation (5.4) corresponds to a more realistic average RASR value of -15.5 dB in cases where on-board DBF processing is used to help suppressing range ambiguities. Figure 5.5 shows that a pure application of BSS does not effectively suppress range ambiguities with a lower SAR mixing matrix. This result confirms the numerical analysis presented in Section 3.3.6, where a much lower mixing matrix value is found to severely degrade the performance of BSS. It also highlights the need for optimization strategies to complement BSS in suppressing range ambiguities.

The next numerical analysis pertains to optimization strategies, encompassing the stacking azimuth lines approach and azimuth sub-band decomposition. Figure 5.6 displays the RASR performance resulting from the implementation of the stacking approach using varying numbers of stacked azimuth lines: $N_{sta} = 0, 30, 100, \text{and } 900$. Furthermore, Figure 5.7 profiles the average RASR performance for different numbers of stacked azimuth lines, showing a clear improvement introduced by the

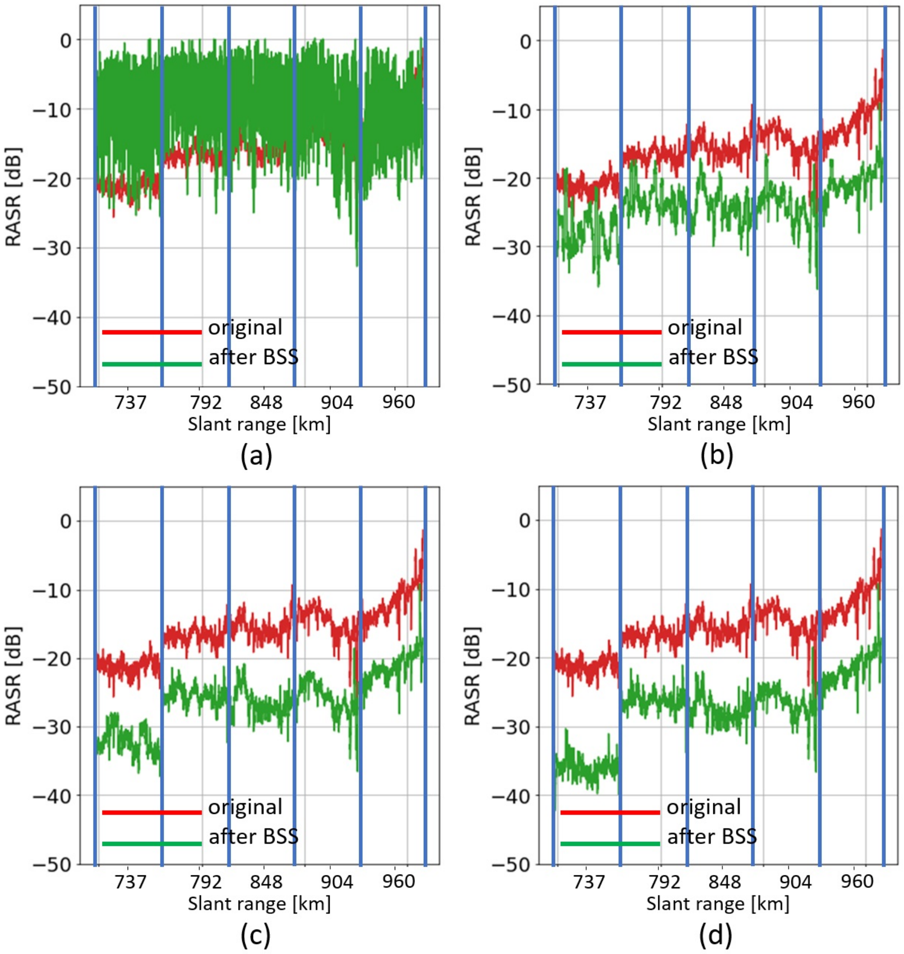

Figure 5.6: Assessment of stacking approach by RASR performance. The BSS is applied in the range compressed data for the case of $\mathbf{A}_{LOW}$ with the stacking approach included. The number of stacked azimuth lines is: (a) $N_{sta} = 1$; (b) $N_{sta} = 30$; (c) $N_{sta} = 100$; (d) $N_{sta} = 900$.

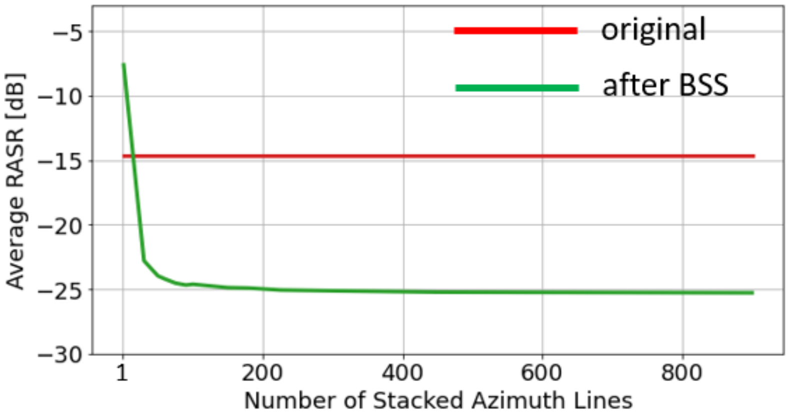

Figure 5.7: Average RASR performance versus number of stacked azimuth lines. The BSS is applied to range compressed data with RCM for the case of $\mathbf{A}_{LOW}$

stacking approach. Specifically, a significant improvement is observed when comparing the result with no stacking and the one obtained by stacking 30 azimuth lines. As the number of stacked azimuth lines increases beyond 100, the improvement reaches saturation.

The results depicted in Figure 5.7 validate the significance of the stacking approach in enhancing the range ambiguity suppression performance. This approach holds significant importance as it allows for a larger sample size, enhancing the optimization of the BSS performance, thereby ensuring an unbiased estimation of the kurtosis. This necessity for a considerably large number of samples becomes particularly relevant when dealing with data that tend to exhibit a Gaussian distribution, such as range-compressed data.

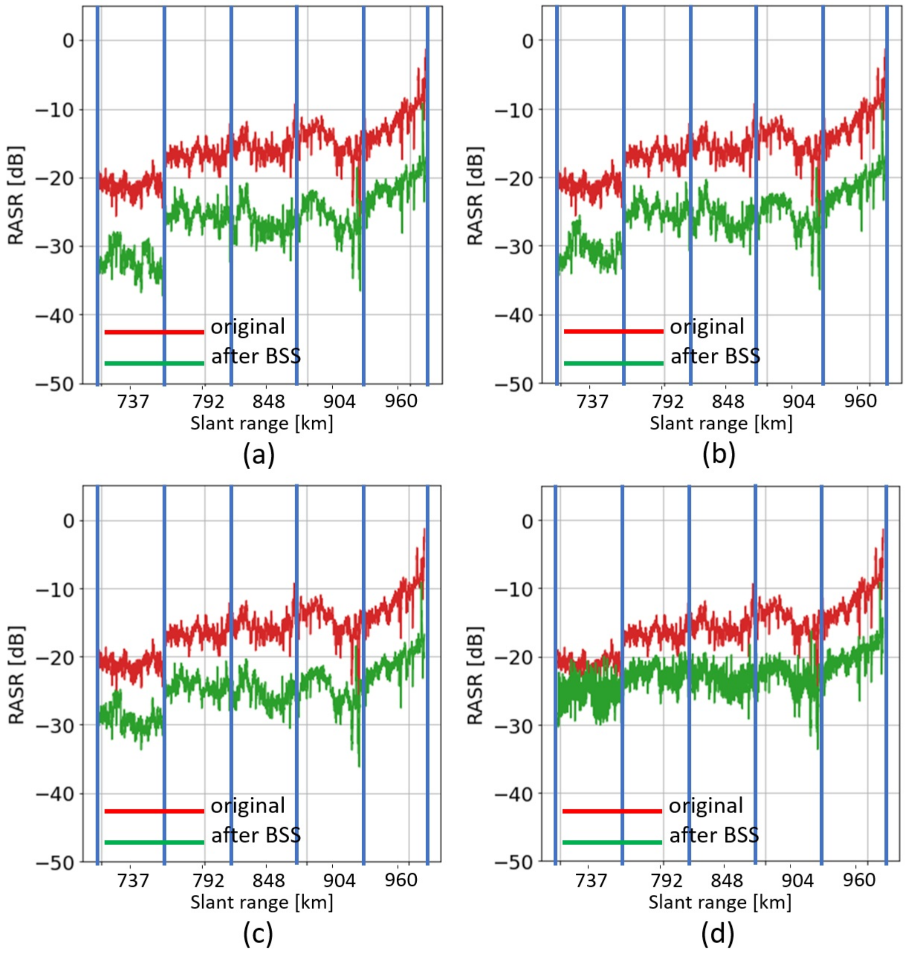

Figure 5.8: Assessment of combined approach by RASR performance for the case of $\mathbf{A}_{LOW}$. $N_{sta} = 100$ is selected and the number of azimuth sub-bands is varied: (a) $N_{sub} = 1$; (b) $N_{sub} = 5$; (c) $N_{sub} = 11$; (d) $N_{sub} = 15$. The BSS is applied on the range-compressed data.

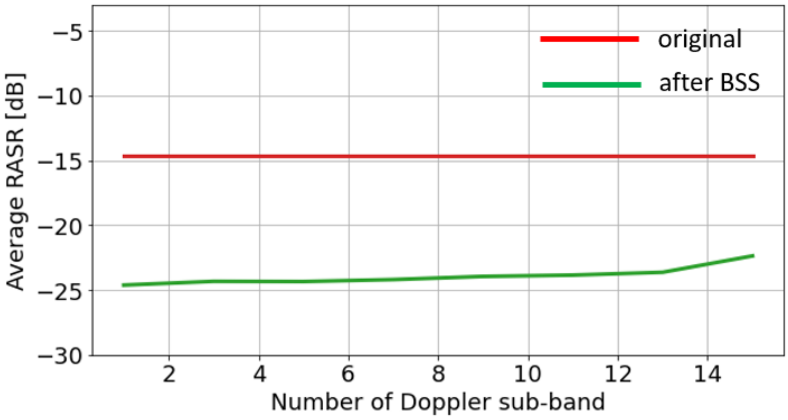

Figure 5.9: Average RASR performance of combined approach, for the case of $\mathbf{A}_{LOW}$, with respect to $N_{sta} = 100$ and varying number of azimuth sub-bands. The BSS is applied to range-compressed data with RCM.

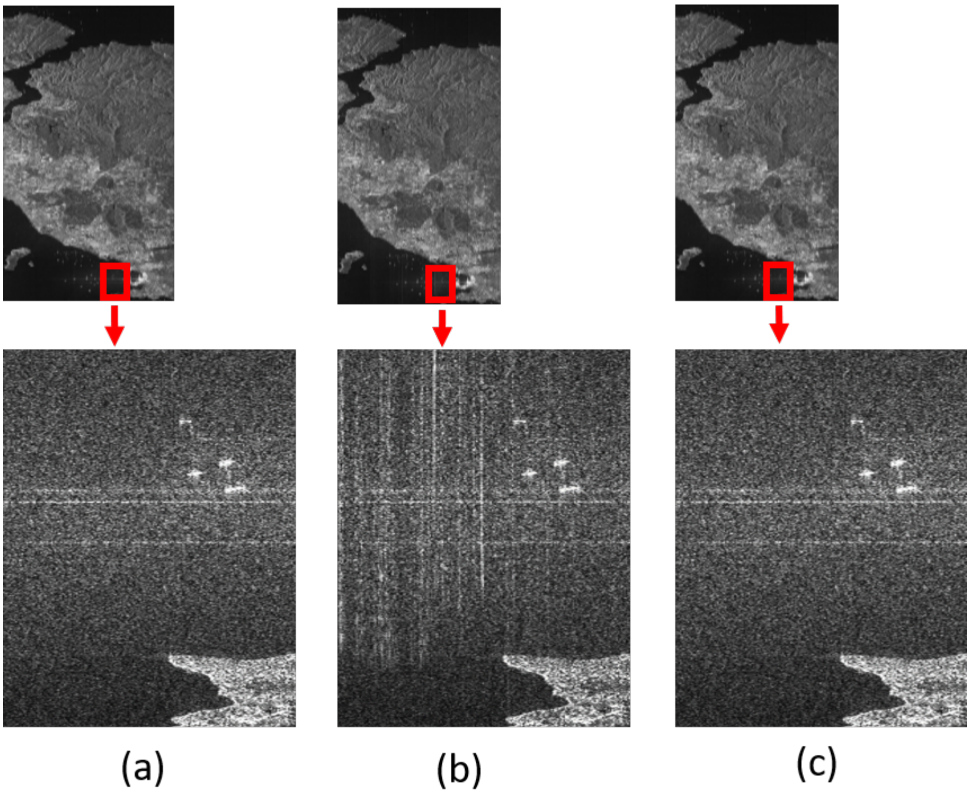

Figure 5.10: Simulated L-band SAR images: (a) ambiguity-free image; (b) ambiguous image; (c) ambiguity-suppressed image. The horizontal axis indicates the range direction, the vertical axis azimuth. The spatial separation between the simulated swath segments is not visualized here.

The impact of the azimuth sub-band decomposition approach on RASR performance is evaluated through empirical analysis, which involves setting a fixed number of stacked azimuth lines and varying the number of azimuth sub-bands. It is noted that the effectiveness of the azimuth sub-band approach is unaffected by the number of stacked azimuth lines. The results are depicted in Figure 5.8. These findings suggest that implementing the azimuth sub-band approach in systems with a Doppler-independent mixing matrix leads to poorer RASR performance. This trend is further highlighted in Figure 5.9, illustrating the average RASR performance concerning different numbers of azimuth sub-bands (N_{sub}).

The degradation in range ambiguity suppression caused by introducing azimuth sub-bands arises from the reduced bandwidth of each sub-band dataset, resulting in a more Gaussian statistic, as indicated by the lower CSK value in Table 5.2. Furthermore, the intent behind employing azimuth sub-bands is to address the Doppler-dependency of the mixing matrix, which also corresponds to the issue of range cell migration. The lower bandwidth will degrade the performance. Therefore, the azimuth sub-band decomposition approach should not be employed for systems which have a Doppler-independent mixing matrix.

A qualitative assessment of the ambiguity suppression effectiveness is showcased in Figure 5.10. The figure compares the simulated ambiguity-free SAR image, the ambiguous SAR image, and the ambiguity-suppressed SAR image. For simplicity, the spatial separation between the simulated swath segments is not visualized. The horizontal lines in Fig. 5.10 are caused by sidelobes of strong targets outside the displayed image area and are not related to range ambiguities. To emphasize the achieved ambiguity suppression, a closer view of the areas marked by red boxes is provided. These areas exhibit a notable improvement attained through the proposed method, particularly in backscattering surfaces like the sea. Such surfaces are characterized by low intensity and are significantly affected by ambiguous disturbances.

In summary, the proposed method has shown that selecting range-compressed data with the RCM effect and stacking approach can significantly improve the performance of range ambiguity suppression. In contrary, the implementation of the azimuth sub-band decomposition degrades the RASR performance for the Doppler-independent mixing matrix case.

5.3 Range-Dependent Mixing Matrix

In this section, the proposed method is applied to a system encountering range-dependent mixing matrix, specifically a SAR system with a planar antenna array employing multiple SCORE beams. This section commences by showing the SCORE beam resulting from the DBF processing in the planar antenna system, consequently leading to a range-dependent mixing matrix.

A planar antenna array system consists of a set of N_{elem} identical antenna elements arranged in a planar grid. The steering of the array is determined by the combination of the element factor and the array factor. Here, the element factor is considered 1 for simplicity. Therefore, the steering of the array is influenced by the array factor, which is a function of the geometric configuration of the antenna array and the direction of the radiation, here denoted by $g_{DBF}(\theta_s)$. Accordingly,

The expression of the steered antenna pattern can be written as [125], [126]:

$$g_{DBF}(\theta_s) = \sum_{n=0}^{N_{elem}-1} w_n \cdot \exp\left\{ j \cdot \frac{2 \cdot \pi \cdot n \cdot d}{\lambda} \cdot \sin(\theta_s) \right\}, \tag{5.5}$$

where θ_s is the look angle; w_n the complex weighting coefficients for the nth element; and d the spacing between elements.

Furthermore, the considered DBF technique used in the simulation is time-variant weighting [69], where the complex weight vector $\mathbf{w} = [w_1 \; w_2 \; .... \; w_{N_{elem}}]$ are determined with the aim to make sure that the receiving beam center exactly points to the direction of central position, given by [69]

$$w_n = \exp\left\{ -j \cdot 2 \cdot \pi \cdot \frac{n \cdot d}{\lambda} \cdot \sin(\theta_0) \right\}, \tag{5.6}$$

where θ_0 is the scalar steering angle or direction of interest.

Table 5.3: Simulation parameters of the planar antenna array

Parameter	Symbol	Value
Antenna height	L_a	5 m
No. channel in elevation	N_{chel}	34
No. of antenna elements/channel	N_{elem}	1
Element spacing	d	14.3 cm
Elevation beamforming algorithm	-	Time-variant weighting
Number of active elements for elevation beamforming	N_{act}	34

Table 5.3 displays the parameters of the antenna system used in this section, in addition to general data parameters in Table 5.1. The mapping of five swaths covers an approximate total swath width of approximately 300 km on the ground.

Figure 5.11(a) and (b) show the simulated SCORE beams. It is important to note that in SCORE, the RX antenna pattern changes as the beams follow the received

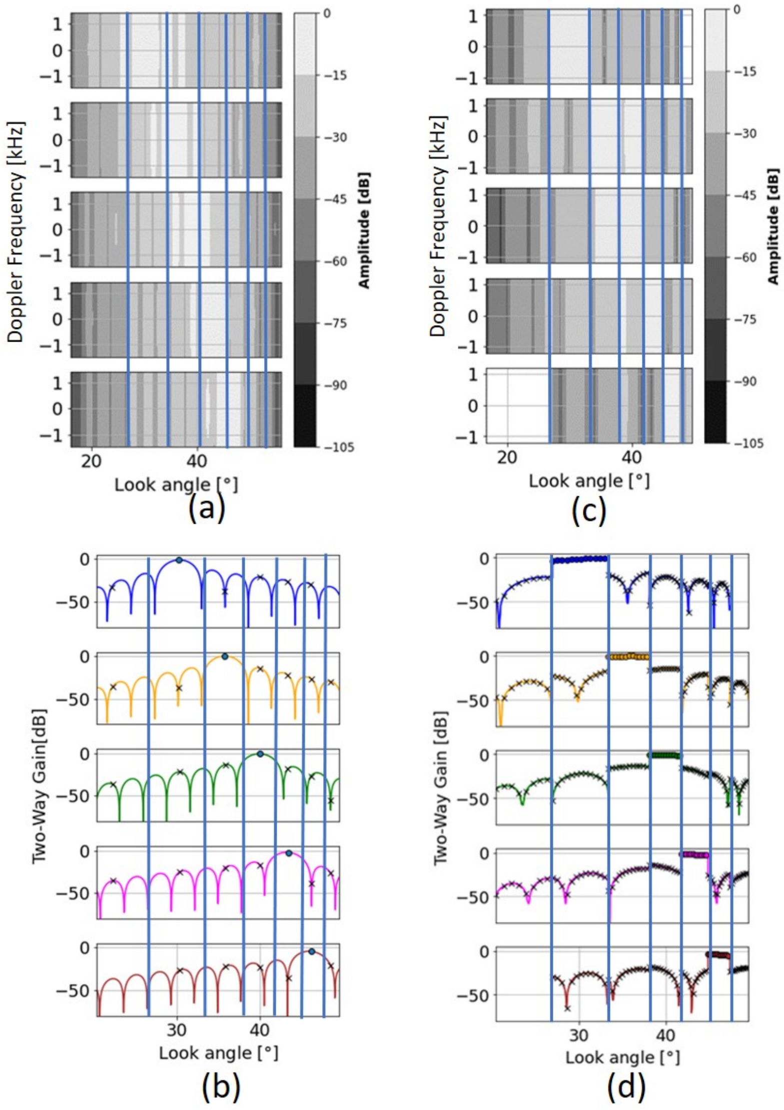

Figure 5.11: SCORE beam as a result of DBF processing: (a) exemplary two-dimensional pattern (b) and its cut at zero Doppler (c) equivalent pattern (d) cut of equivalent pattern zero Doppler. The blue vertical lines indicate the boundary between the simulated swath segments. In (b) and (d), the circles indicate useful signals, and the crosses indicate range-ambiguous signals.

echoes along the swath. To offer an improved way of visualizing the SCORE beams, Figure 5.11(c) and (d) have been added. These figures demonstrate the equivalent pattern, which is defined as the collection of the antenna pattern gains at the locations of the mainlobe and sidelobes the SCORE pattern sweeps the entire swath, expressed by

$$g''(\theta_s) = \sum_j \sum_k g_{DBF,j}(\theta_s) \cdot \delta(\theta_s - \theta_{jk}), \tag{5.7}$$

where θ_{jk} is the look angle at the location of j, k; j denotes index of the SCORE pattern, sweeping from the intended swath minimum look angle θ_{min} to the maximum look angle θ_{max}; k the integer number indicating the order of the ambiguity where $k = 0$ is the useful signal; and δ the Kronecker delta.

It is worth mentioning that the empty regions in the far range of the first beam and the near range of the fifth beam of the equivalent pattern, i.e., Figure 5.11 (c) and (d), are due to the fact that in this simulation, the maximum order of ambiguity is 4. Ambiguities beyond the 4th order are not simulated since they are less significant, especially in the case of five elevation beams SAR systems.

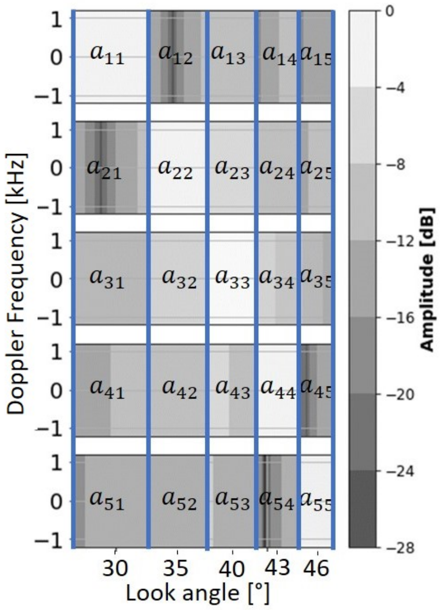

Figure 5.12: Mixing matrix, $\mathbf{A}_{PLA}$, extracted from SCORE DBF antenna patterns. The blue vertical lines indicate the boundary between the simulated swath segments.

The mixing matrix for planar antenna case, $\mathbf{A}_{PLA}$ as illustrated in Figure 5.12, is derived from the antenna pattern, as outlined in Section 3.1. It is evident from the figure that the values of the mixing matrix vary over range time but remain constant across Doppler frequency. As a result, the dependency condition of the mixing matrix occurs solely along the range direction, leading to a range-dependent mixing matrix.

The initial analysis focuses on the influence of the stacking approach. Figure 5.13 illustrates the impact of varying numbers of stacked azimuth lines ($N_{sta} = 1, 30, 100, 900$) on the performance of the BSS method. Although the stacking approach evidently improves the performance, further investigation of the RASR performance dependence on the number of stacked azimuth lines is demonstrated in

Figure 5.14. The figure indicates that beyond $N_{sta} = 200$, the performance begins to degrade due to range dependent variations surpassing the improvement. This trend differs from the case of the range-independent mixing matrix, where the RASR performance improves as the number of N_{sta} increases due to the lack of range dependent variations in the case of the range-independent mixing matrix. The figure also demonstrates that the RASR value increases along the range direction, which is commonly observed in real SAR environments.

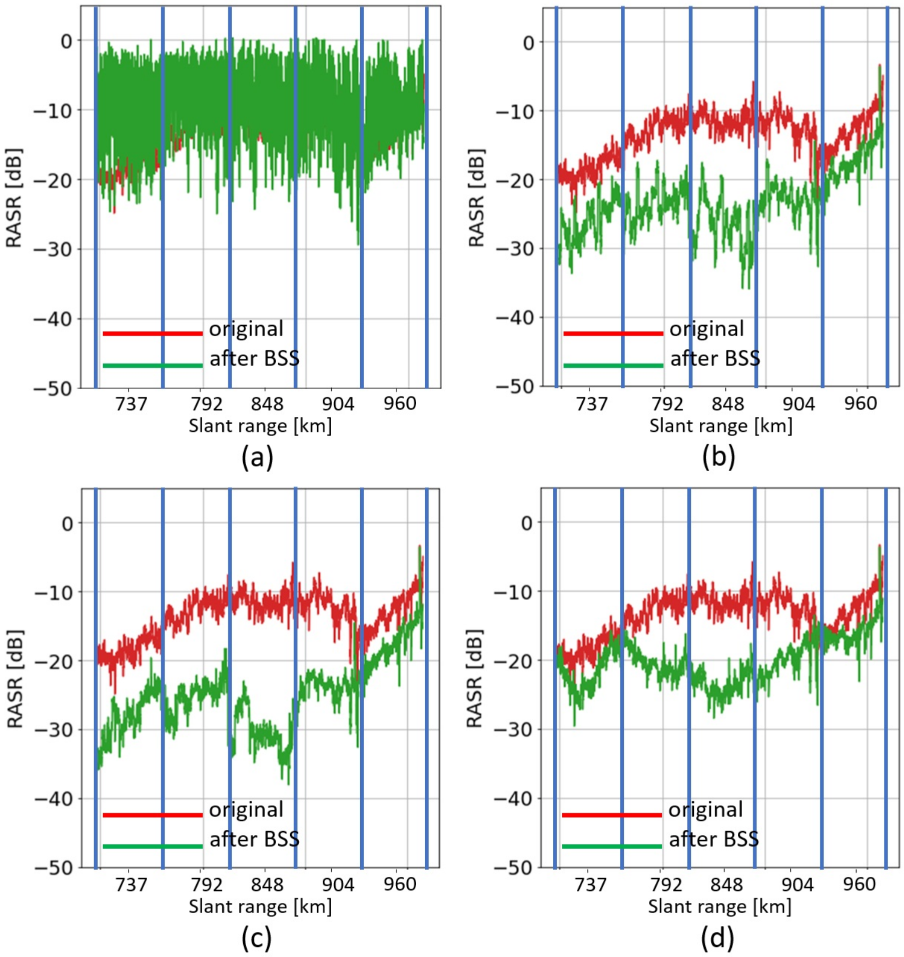

Figure 5.13: RASR performance for the case of $\mathbf{A}_{PLA}$. The BSS is applied on the range-compressed data with RCM. The stacking optimization approach is included. The number of stacked azimuth lines is: (a) $N_{sta} = 1$; (b) $N_{sta} = 30$; (c) $N_{sta} = 100$; (d) $N_{sta} = 900$.

The trend highlights the necessity of empirical analysis when dealing with the dependencies of the mixing matrix along the range, to determine the optimal N_{sta} that yields the best RASR performance. Based on the discussion of the stacking approach in Section 4.2.2 and the outcome presented in Figure 5.14, two conclusions can be

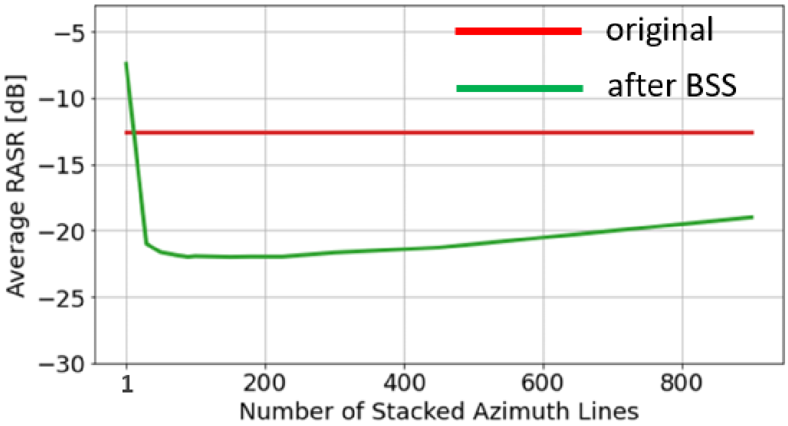

Figure 5.14: Average RASR performance, for the case of $\mathbf{A}_{PLA}$, versus number of stacked azimuth lines. The BSS is applied to range-compressed data with RCM.

inferred: (i) until $N_{sta} = 90$, the stacking approach improves the performance significantly more than the degradation caused by the underestimation of the mixing matrix; (ii) above $N_{sta} = 200$, the degradation due to the underestimation of the mixing matrix exceeds the performance improvement due to the stacking approach. The latter observation is consistent with the results observed in the case of a range-independent mixing matrix, where the improvement achieved through the stacking approach saturates for $N_{sta} > 200$.

The impact of the azimuth sub-band decomposition approach on the performance is assessed by applying the method to varying numbers of sub-bands while fixing the number of stacked azimuth lines. Figure 5.15 demonstrates how different numbers of azimuth sub-bands ($N_{sub} = 1, 5, 11,$ and 15) affect the performance of the BSS method. The RASR performance is found to be relatively consistent across the different sub-bands, with the exception of $N_{sub} = 15$, which exhibits lower performance. The lower performance for the far-range swath is due to the contribution of out-of-swath ambiguities, which considerably affect the far-range swath, as seen in the high sidelobe level of the out-of-swath far-range antenna pattern in Figure 5.11.

Figure 5.16 investigates the relation between the number of azimuth sub-bands and RASR performance. Since the mixing matrix in the planar system is Doppler-independent, the effect of the azimuth sub-band decomposition is similar to the case of a mixing matrix in Section 5.2. Furthermore, the analysis presented in Figure 5.16 encompasses two primary issues. First, the discussion involves the impact of RCM on performance, which was initially mentioned in the azimuth sub-band approach discussion in Section 4.2.3, namely, that RCM degrades performance and could be overcome through an azimuth sub-band decomposition approach. Second, when the sub-band decomposition technique is performed, the data of each sub-band have a lower bandwidth, resulting in a more Gaussian distribution as indicated by the

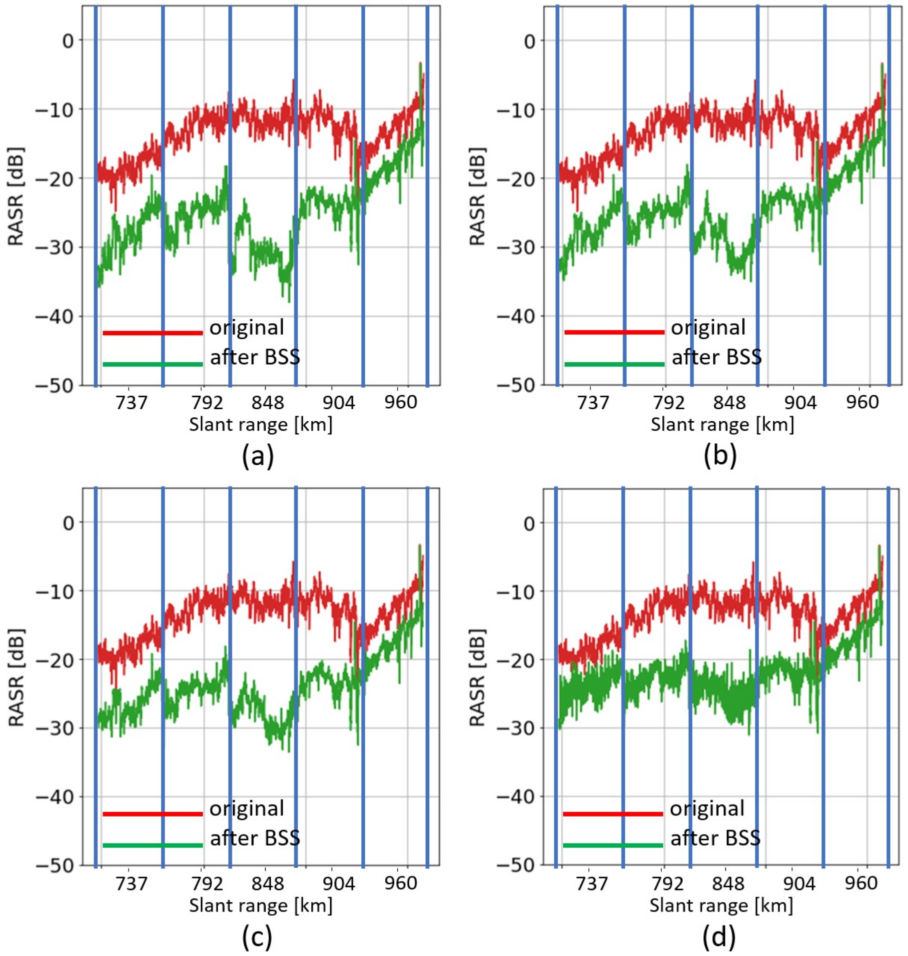

(a) (b)

(c) (d)

Figure 5.15: RASR performance for the case of $\mathbf{A}_{PLA}$. The BSS is applied to the range compressed data. The stacking approach ($N_{sta} = 100$) and the azimuth sub-band decomposition are included. The number of sub-bands is: (a) $N_{sub} = 1$; (b) $N_{sub} = 5$; (c) $N_{sub} = 11$; (d) $N_{sub} = 15$.

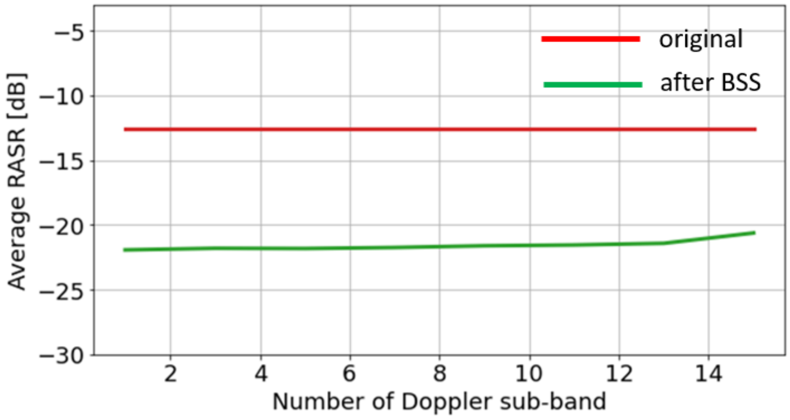

Figure 5.16: Average RASR performance, for the case of $\mathbf{A}_{PLA}$, versus number of azimuth sub-bands. The BSS is applied to range-compressed data with RCM.

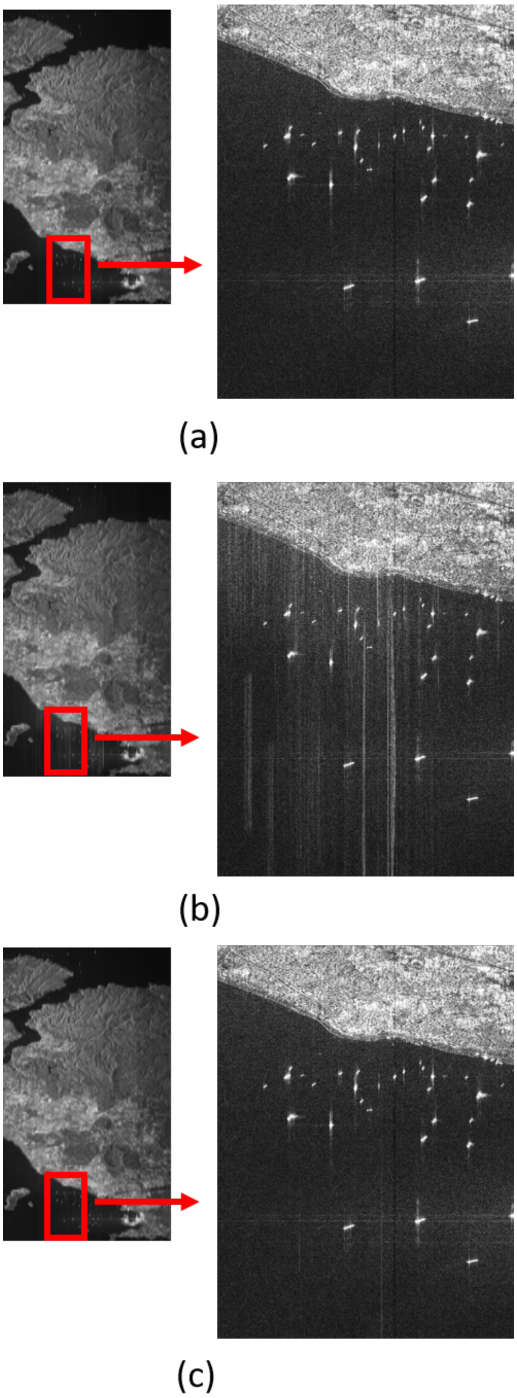

Figure 5.17: Simulated planar L-band SAR images: (a) ambiguity-free image; (b) ambiguous image; (c) ambiguity-suppressed image. The horizontal axis indicates the range direction, the vertical axis azimuth. The spatial separation between the simulated swath segments is here not visualized.

lower CSK value in Table 5.2. Accordingly, when the value of the mixing matrix is dependent along the Doppler direction, the overall RASR performance will be degraded.

Based on the aspects mentioned earlier, two conclusions can be drawn. Firstly, for N_{sub} values up to 13, the degradation caused by the sub-band technique due to the reduction of the non-Gaussianity level is well compensated by the improvement due to mitigating RCM effect. Secondly, for N_{sub} values greater than 13, the degradation due to the sub-band technique becomes greater than the improvement due to mitigating the RCM effect. Therefore, in the present case, the number of azimuth sub-bands can be chosen within $0 \leq N_{sub} \leq 10$.

Based on the empirical analysis of the planar antenna, it is concluded that the optimal values for N_{sta} and N_{sub} are in the ranges of $90-200$ and $0-10$, respectively. It should be noted that the reference system in this chapter operates in L-band. For X-band systems, the level of RCM is significantly lower than for L-band systems, which makes the use of the azimuth sub-band decomposition approach less effective, as the contribution of RCM in performance degradation is also less significant.

Figure 5.17 presents a qualitative assessment of the effectiveness of the ambiguity suppression. The figure displays a comparison between the simulated ambiguity-free SAR image, the ambiguous SAR image, and the ambiguity-suppressed SAR image. For simplicity, the spatial separation between the simulated swath segments is not visualized. To highlight the achieved ambiguity suppression, a closer view of the areas marked by red boxes is included. These areas reveal a substantial improvement resulting from the proposed method, especially for backscattering surfaces such as the sea. These surfaces are characterized by low intensity and are significantly impacted by ambiguous disturbances.

5.4 Range- and Doppler-Dependent Mixing Matrix

In this section, the proposed method is applied to a system encountering a range- and Doppler-dependent mixing matrix, specifically a SAR system with an array-fed reflector antenna with SCORE beams. Similar to the planar system, this section commences by demonstrating simulated multiple SCORE beams for the array-fed reflector system.

The array-fed reflector antenna system is composed of a reflector dish and an array of feed elements. The positioning of the feed elements in the array is determined by the desired radiation pattern of the antenna, which is typically arranged in a regular grid pattern on a planar surface. The relative phase and amplitude of each feed element is determined by its position within the grid, with the spacing between elements typically being a fraction of the operating frequency wavelength. The size of the grid is chosen based on the desired aperture size and resolution.

The design process usually involves modeling the antenna system using electromagnetic simulation software, and then adjusting the position and phase of each feed element until the desired radiation pattern is achieved. In this thesis, the radiation pattern of each feed element are identical from the work of Tandem-L mission [65]. As a result, the simulator employed for this type of antenna has been simplified, using only the MVDR beamforming algorithm to direct the beam in a specific direction, as determined by:

$$g_{DBF}(\theta_s) = \sum_{n \in N_{act}} w_n \cdot g_n(\theta_s), \tag{5.8}$$

where θ_s is the look angle; N_{act} the number of activated array channels; w_n the weight applied to the n-th channel; and $g_n(\theta_s)$ describes the radiation pattern of the individual channel.

Table 5.4: Simulation parameters of the array-fed reflector antenna

Parameter	Symbol	Value
Diameter	d	15 m
No. channel in elevation	N_{chel}	35
Focal length	l_{fc}	13.5 m
Feed element spacing	d	15.7 cm
Number of simultaneous elevation beams	N	5
Elevation beamforming algorithm	-	MVDR
Number of active elements for elevation beamforming	N_{act}	5

To obtain the weight vector $\mathbf{w}$, it is recalled that the MVDR weight vector is given by:

$$\mathbf{w} = \frac{\mathbf{R}_{cov}^{-1}\mathbf{g}(\theta_0)}{\mathbf{g}^H(\theta_0)\mathbf{R}_{cov}^{-1}\mathbf{g}(\theta_0)}, \tag{5.9}$$

where $\mathbf{g} = \{g(n) | n \in N_{act}\}$ is the steering vectors; $\mathbf{R}_{cov}$ the covariance matrix of the received signals at the array; and θ_0 is the steering of the pattern. While the weight vector formulation relies on the received signal, it is important to note that in the simulation, the pattern generation step is independent of the signal. Therefore, in this simulation it is assumed that $\mathbf{R}_{cov} = \mathbf{I}$. Accordingly, the weight vector is simplified to

$$\begin{aligned} \mathbf{w} &= \frac{\mathbf{I}\mathbf{g}(\theta_0)}{\mathbf{g}^H(\theta_0)\mathbf{I}\mathbf{g}(\theta_0)}, \\ &= \frac{\mathbf{g}(\theta_0)}{\mathbf{g}^H(\theta_0)\mathbf{g}(\theta_0)}. \end{aligned} \tag{5.10}$$

In this case, it can be seen that the MVDR weight vector is proportional to the matched filter weight vector but scaled to achieve unity gain in the direction of interest, θ_0. Therefore, the simplification where $\mathbf{R}_{cov} = \mathbf{I}$ still maintains the unity gain requirement of the MVDR beamformer.

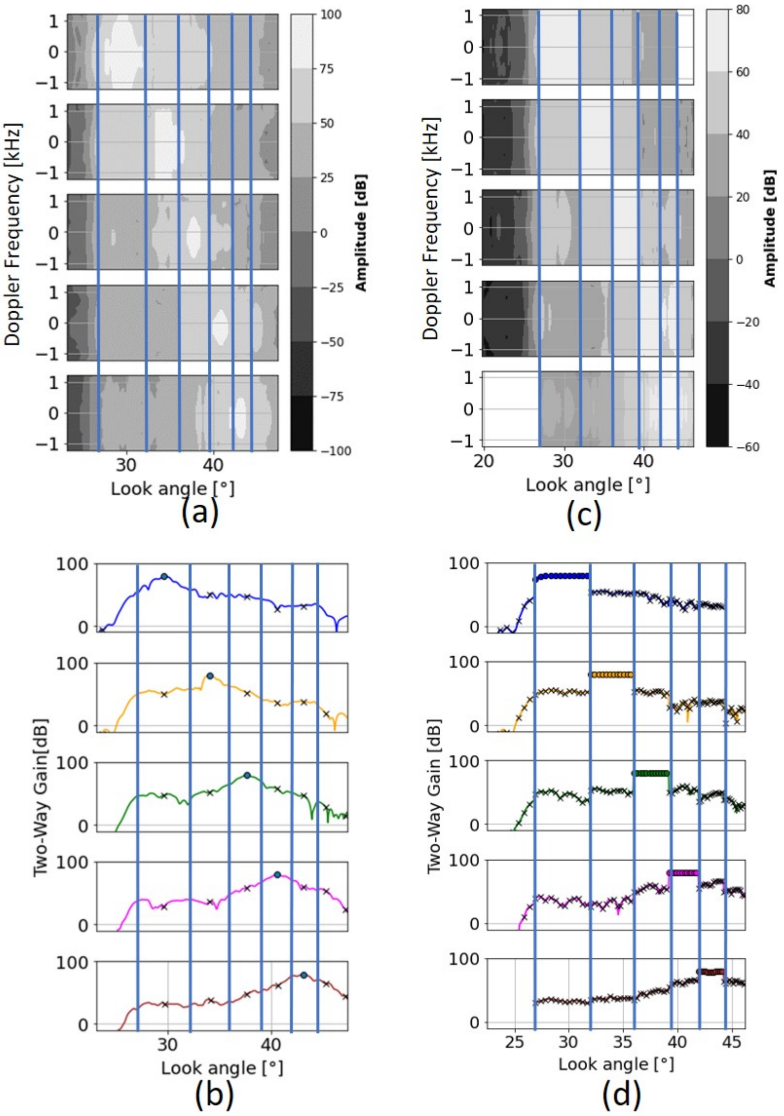

Figure 5.18: SCORE beam as a result of DBF processing from an array-fed reflector: (a) exemplary two-dimensional pattern and its (b) cut in zero Doppler (c) equivalent pattern (d) cut of equivalent pattern in zero Doppler. The blue vertical lines indicate the boundary between the simulated swath segments. In (b) and (d), the circles indicate useful signals, and the crosses indicate range-ambiguous signals.

Table 5.4 outlines the parameters of the reference system utilized in this section, which has been designed partially similar to Tandem-L [40]. The system comprises a Transmit-Receive Module (TRM) with a peak power of 143W and employs a reflector antenna with a 15-meter diameter. This design ensures that the system achieves a Noise Equivalent Sigma Zero (NESZ) below -25 dB, signifying a high sensitivity to detect radar echoes. Consequently, the system is configured to map five swaths, covering a total ground swath extent in the order of 300 km with an azimuth resolution of 6 m. The main difference compared to Tandem-L regards the orbit height, which is lower due to the intention of introducing a slightly higher range-ambiguity value.

In contrast to the planar system where all Rx channels must be activated to form the SCORE beam, the array-fed reflector antenna requires only few active channels to create a narrow SCORE beam for each range. This characteristic showcases the advantages of using an array-fed reflector antenna system, which demands fewer activated channels compared to a planar antenna to obtain SCORE beams. However, in the Tx beams, all channels must be activated to produce a wide beam. This behavior stands in contrast to the planar system, which necessitates all channels to be active in the Rx beams, illustrating the opposite behaviors of the two antenna types concerning channel activation for beam generation.

Figure 5.18 presents the multiple SCORE two-way patterns and their corresponding equivalent patterns. The resulting mixing matrix $\mathbf{A}_{TDL}$ derived from these patterns is depicted in Figure 5.19. It can be observed that the values of the matrix vary along both the range and Doppler dimensions, indicating the existence of a range- and Doppler-dependent mixing matrix. This dependency leads to a more complicated mixing matrix structure, as compared to the case of planar antenna array systems. Furthermore, it is worth noting that the off-diagonal elements in $\mathbf{A}_{TDL}$ have two significant characteristics: (i) their values exhibit a strong variation, particularly along the range direction; and (ii) they can reach extremely low values of -35 dB. These characteristics make the successful application of the method challenging. As compared to a planar antenna, the RASR value in a reflector antenna is lower, and this also becomes another advantage of using a reflector antenna.

Since a system with a range- and Doppler-dependent mixing matrix leads to a more challenging mixing matrix structure compared to other previously discussed systems, a more detailed and comprehensive analysis will be conducted. The initial analysis will focus on distributed targets, emphasizing the RASR as a key metric. Subsequently, the second analysis will assess the method's impact on the impulse response quality.

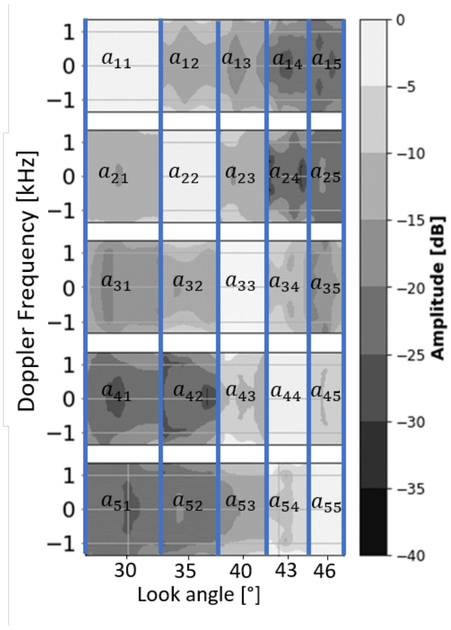

Figure 5.19: Mixing matrix, $\mathbf{A}_{TDL}$, extracted from Tandem-L DBF antenna patterns. The blue vertical lines indicate the boundary between the simulated swath segments.

5.4.1 Performance Analysis

The SAR input data used in this analysis refer to the range-compressed data where the RCM is not corrected, as depicted in Figure 5.3(c). The first analysis focuses on evaluating the performance of the BSS method solely using the stacking approach, without implementing the azimuth sub-band decomposition approach. Figure 5.20 displays the RASR performance for various numbers of stacked azimuth lines, specifically $N_{sta} = 1, 30, 100$, and 900. In general, employing the stacking technique leads to a substantial improvement in RASR performance, as observed in the case discussed in Sections 5.2 and 5.3, respectively.

To determine the optimized value of N_{sta}, it is essential to conduct another empirical analysis because the currently considered system, the array-fed reflector antenna, may possess a different optimized value of N_{sta} compared to a planar antenna system due to the fact that the optimized value depends on the antenna pattern. Figure 5.21 summarizes the impact of the varying number of N_{sta} on the average RASR performance. Examining the results presented in Figure 5.21, three conclusions can be drawn: (i) Until $N_{sta} = 100$, the stacking approach significantly enhances RASR performance, despite the underestimation of the mixing matrix; (ii) Beyond $N_{sta} = 100$, the degradation resulting from the underestimation of the mixing matrix outweighs the improvement gained from the stacking approach; (iii) Starting from $N_{sta} = 450$, the degradation due to the underestimation of the mixing matrix becomes comparable to the improvement obtained from the stacking approach. This third observation suggests that $\mathbf{A}_{TDL}$ exhibits lower variation along range compared to the mixing matrix of a planar antenna, $\mathbf{A}_{PLA}$.

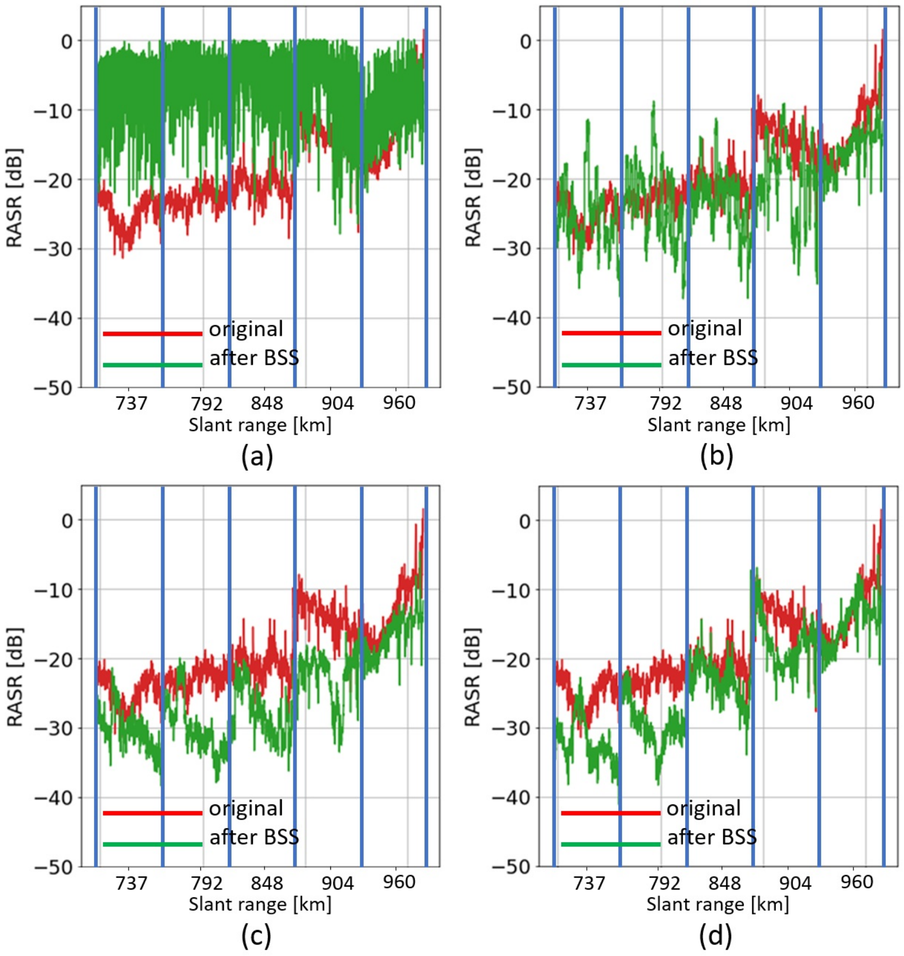

Figure 5.20: Assessment of the stacking approach by RASR performance for the case of $\mathbf{A}_{TDL}$. The BSS is applied in the range compressed data. The number of stacked azimuth lines is: (a) $N_{sta} = 1$; (b) $N_{sta} = 30$; (c) $N_{sta} = 100$; (d) $N_{sta} = 900$.

This finding confirms the significance of the performance degradation caused by the limited number of samples, as discussed in Section 4.2.2, and further validates the numerical justification for using the stacking approach as a way to provide a larger number of samples and to reduce the number of outliers, as presented in Section 5.2. This issue outweighs the degradation caused by the Doppler-dependent mixing matrix.

The next analysis examines the combined empirical effect of stacking and azimuth sub-band strategies on achieving optimal RASR performance. The analysis involves

Figure 5.21: Average RASR performance, for the case of $\mathbf{A}_{TDL}$, versus number of stacked azimuth lines. The BSS is applied to range compressed data with RCM.

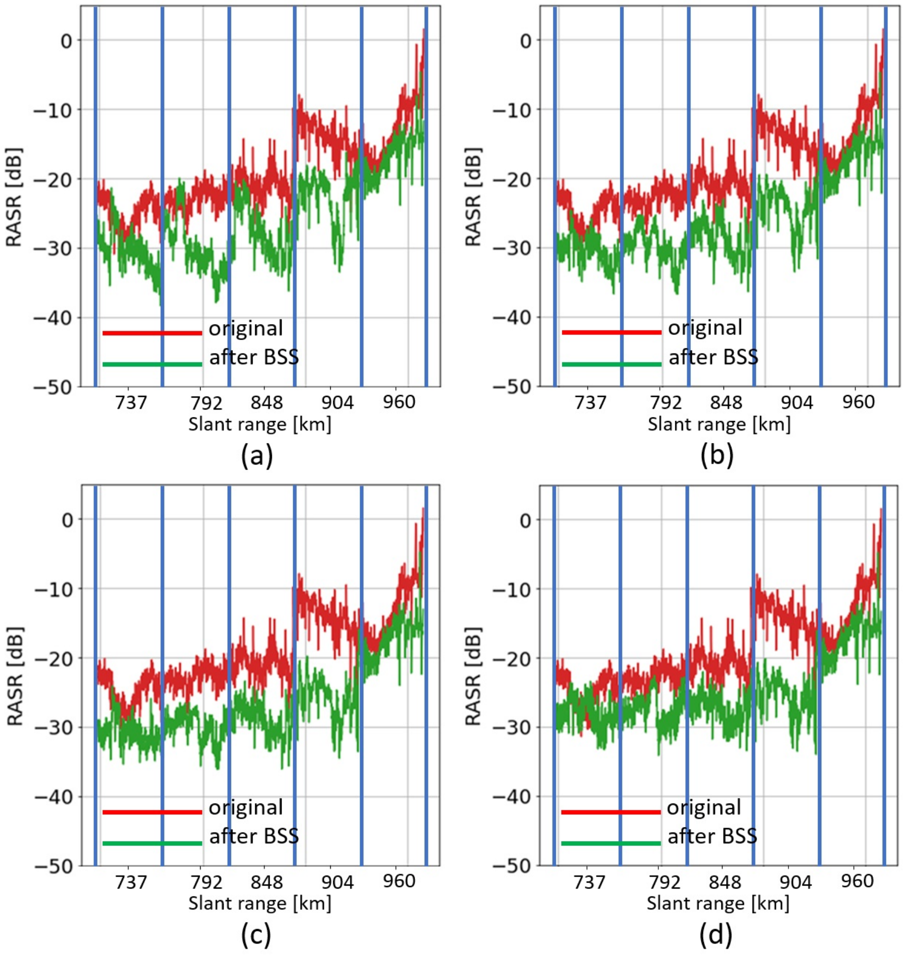

Figure 5.22: Assessment of combined approach by RASR performance for the case of $\mathbf{A}_{TDL}$. $N_{sta} = 100$ is selected and the number of azimuth sub-bands is varied: (a) $N_{sub} = 1$; (b) $N_{sub} = 3$; (c) $N_{sub} = 7$; (d) $N_{sub} = 15$. The BSS is applied to the range-compressed data.

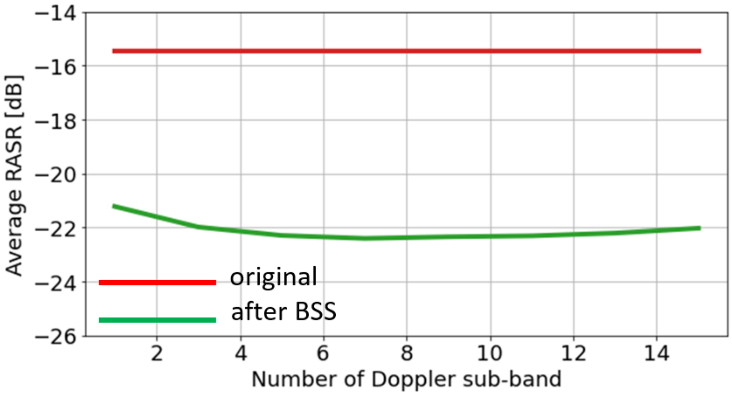

Figure 5.23: Average RASR performance of combined approach, for the case of $\mathbf{A}_{TDL}$, with respect to $N_{sta} = 100$ and varying number of azimuth sub-bands. The BSS is applied to range-compressed data with RCM.

evaluating $N_{sta} = 100$, the optimal number of stacked azimuth lines, while varying the number of sub-bands ($N_{sub} = 1, 5, 11$, and 15). The results are presented in Figure 5.22. Although the azimuth sub-band approach shows less improvement compared to the stacking approach, it is still evident that when both strategies are combined, a notable improvement of approximately 8 dB is observed for $N_{sub} = 7$, particularly in the subswaths centred at slant ranges of 790 km and 840 km.

Figure 5.22 also highlights that range ambiguity suppression performs less well in the far range subswath compared to the other subswaths. This is attributed to the contribution of the out-of-swath ambiguity signals that are still significant enough in the far range subswath. This reflects the imperfect attenuation of range ambiguities in the far range by the Tx pattern. The issue could be solved by either having a better shape of the Tx pattern or adding an additional auxiliary Rx beam to collect appropriate data from the far range region.

The discussion regarding the impact of the number of azimuth sub-bands on RASR performance, along with the utilization of the stacking approach, as summarized in Figure 5.23, can be categorized into four aspects: the variation of $\mathbf{A}_{TDL}$ along the Doppler direction, range cell migration, the gain of the antenna pattern in non-zero Doppler regions, and the statistics of the sub-band data. Based on the analysis of these aspects, two conclusions can be drawn: (i) until $N_{sub} = 7$, the improvement due to the variation of A_{TDL} and the range cell migration effect, as discussed in Section 4.2, outweighs the degradation due to the reduction of non-Gaussian values within each sub-band; (ii) from $N_{sub} = 7$, the degradation due to the previously mentioned reasons is greater than the improvement. Moreover, it can be observed that the azimuth sub-bands offer a lower improvement in performance compared to the stacking approach, as the antenna pattern values, weighting the ambiguous signals, already aid in suppressing the range ambiguities components in the non-zero Doppler region.

In summary, the optimal RASR performance is obtained when using $N_{sub} = 7$ and $N_{sta} = 100$, resulting in a range ambiguity suppression average of 6 dB. It is important to note that the ideal number of stacked azimuth lines heavily depends on the length of data take. When the longer data are considered, the number of stacked azimuth lines can be reduced. Additionally, the number of stacked azimuth lines and azimuth sub-bands also depends on the assumed antenna patterns and how the main-to-sidelobe ratio varies with range and azimuth. Therefore, the values obtained in this study should be applicable to similar antenna designs.

5.4.2 Further Analysis

Since the SAR system with an array-fed reflector antenna leads to the most challenging mixing matrix structure, it is worth discussing this method in more detail.

The initial discussion concerns the sequence of implementing two optimization strategies: stacking and azimuth sub-band decomposition. In the proposed method as suggested in Figure 4.6, the azimuth sub-band approach is applied before the stacking approach. Figure 5.24 illustrates that when these strategies' order is reversed, implementing stacking first followed by the azimuth sub-band approach, a similar result is obtained.

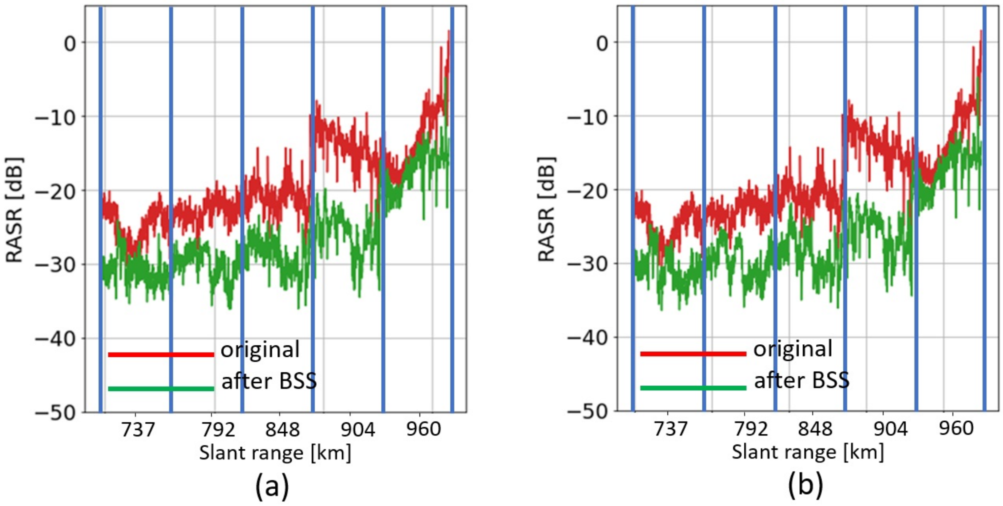

Figure 5.24: Comparison of RASR performance when the order of implementing two strategies is reversed: (a) azimuth sub-band approach implemented first, followed by the stacking approach, as seen in Figure 5.22(c); and (b) stacking approach implemented first, followed by the azimuth sub-band approach.

The second discussion concerns the resilience of the proposed method against the range cell migration (RCM) effect. To assess this, a parameter modification is performed by doubling the wavelength value. Referring to equations (4.9)-(4.11), doubling the wavelength leads to a fourfold increase in the amount of RCM that needs correction. The simulated value of range cell migration is depicted in Figure 5.25.

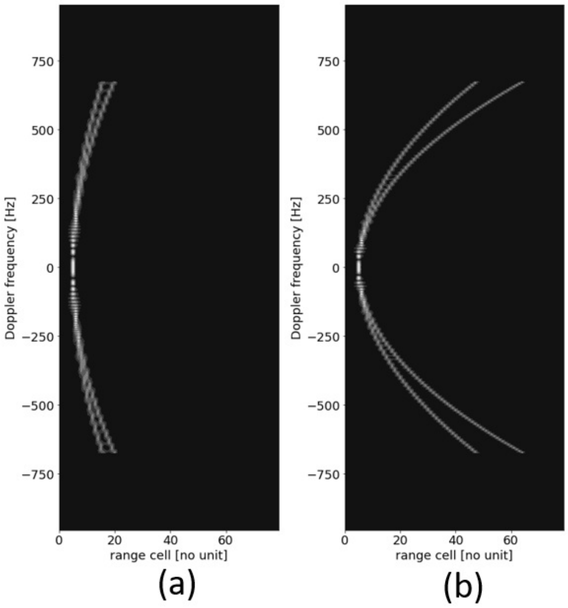

Figure 5.25: RCM simulation depicting the scenario involving range-compressed data of the useful target combined with range-ambiguous target for: (a) Reference L-band SAR. (b) A modified $\lambda = 48$ cm, i.e., twice the reference value, as in P-band SAR. The plot is represented in the range-Doppler domain.

The proposed method is applied to the SAR input using suggested optimal strategies, which involve implementing uncorrected RCM in range-compressed data and employing stacking strategies with 100 azimuth lines ($N_{sta} = 100$), along with azimuth sub-band decomposition strategies utilizing 7 azimuth sub-bands ($N_{sub} = 7$). Figure 5.26 displays the results of the proposed method in a scenario with a fourfold increase in range cell migration. It demonstrates the effectiveness of the proposed method in handling such a case. A comparison of these results with those obtained by applying the proposed method to the reference systems, as depicted in Figure 5.22 (c), indicates a similar level of performance. This validates the robustness of the proposed method against RCM. In the case of a higher amount of RCM, a higher N_{sub} is expected to improve performance with increased uncorrected RCM, outweighing the degradation from azimuth-dependent mixing matrix effects, although the improvement is anticipated to be modest.

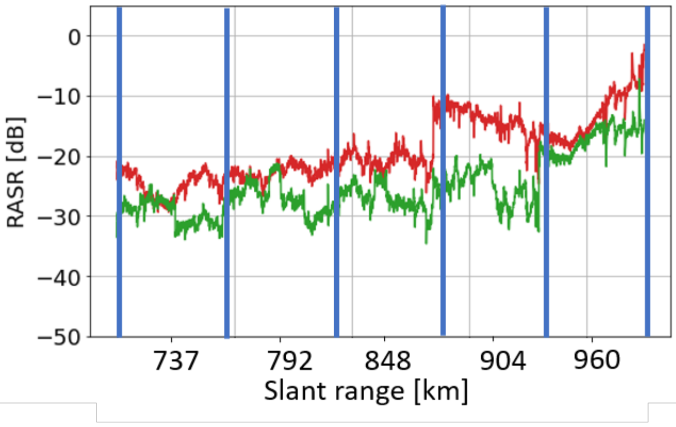

Figure 5.26: RASR performance for the system with 4 times reference system's RCM.

To further clarify the advantages of the proposed method, the third discussion presents a performance comparison between this method and others. Figure 5.27 illustrates two relevant benchmarks for range ambiguity suppression: the MVDR as proposed in [72], which requires knowledge of the antenna pattern, and the BSS approach based on second-order blind identification (SOBI) as proposed in [53], which does not require knowledge of the antenna pattern. To simulate more realistic input data accounting for inaccuracies in the knowledge of the antenna pattern, digital channel errors are introduced. These errors include phase error standard deviation levels of $\sigma_\zeta = 40°$ and magnitude standard deviation levels of $\sigma_\xi = 0.2$, as described in [72] and illustrated in Figure 5.28. Furthermore, various levels of noise are added to the simulated SAR data, leading to mean image data SNR of 15 dB and 10 dB. It is important to note that both simulated SNR values are realistic for advanced HRWS L-band systems with a NESZ of -25 dB. Additionally, it is noted that SAR data can have varying SNR values depending on incident angle and polarization type [127], [128].

The results obtained are reported in Figure 5.27 (a) and (b), respectively for SNR = 15 and 10 dB. These results demonstrate that the proposed method outperforms the others in both simulated scenarios. Particularly, an improvement of up to 10 dB in the near range can be achieved. Additionally, as expected from [97], [98], [99], the proposed method based on HO BSS exhibits higher robustness against noise compared to the SOBI (method based on SO BSS) in [53]. Even in noisier conditions (SNR = 10 dB), the proposed method continues to perform well, while the method in [53] shows a degradation of about 3 dB. The implementation of the SOBI algorithm in this case adopts the code described in [129], with the modification in a time-lagged covariance matrix to comply with the complex-valued signal, following the description in [94].

It is worth to note that the results shown in Figure 5.27 for MVDR are somewhat optimistic. The simulation simplifies the scenario by solely considering digital chan-

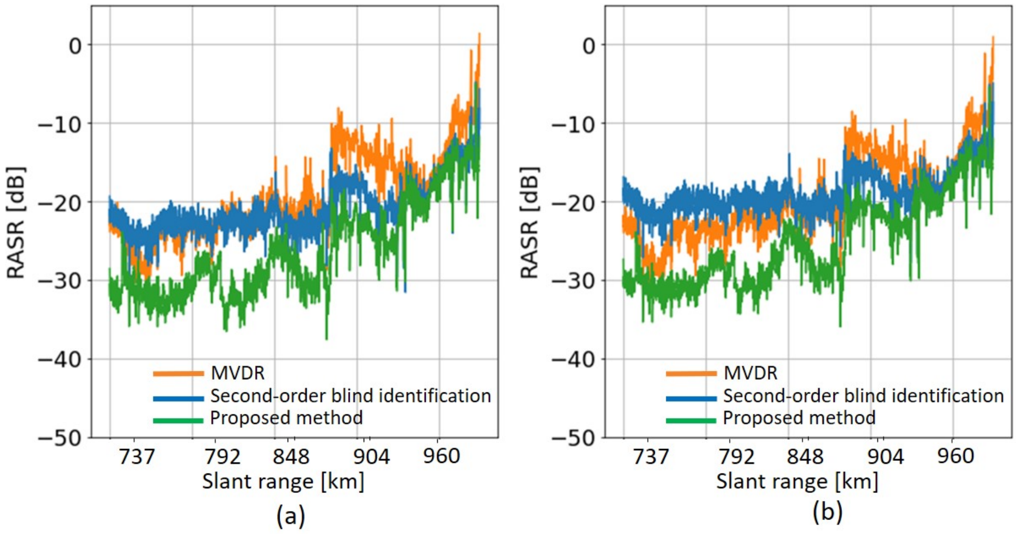

Figure 5.27: The RASR performance of different range ambiguity suppression methods, including MVDR (blue), SOBI (orange), and the proposed method (green).

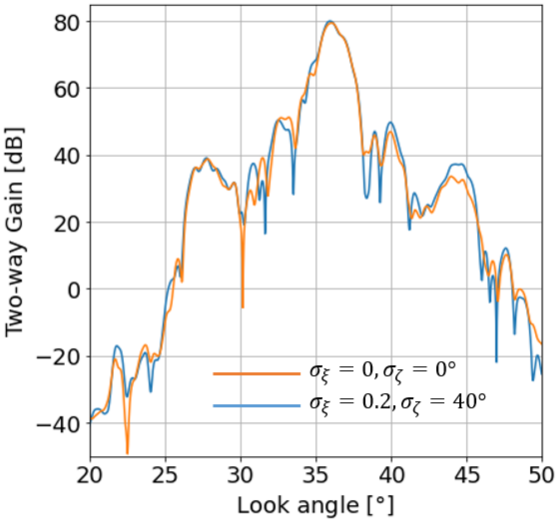

Figure 5.28: Example of two-way reflector antenna gain after MVDR beamforming in cases with and without digital channel errors, shown in blue and orange, respectively.

nel errors, which has a minimum effect in the reflector antenna pattern as modeled by [72] and shown in Figure 5.28. In reality, other errors stemming from pattern uncertainty, mispointing, and deformation of the reflector antenna must also be taken into account. These factors can significantly degrade the performance of the MVDR method. Conversely, the proposed method exhibits robustness even when considering these errors, resulting in a potentially wider performance gap between the proposed method and other deterministic methods.

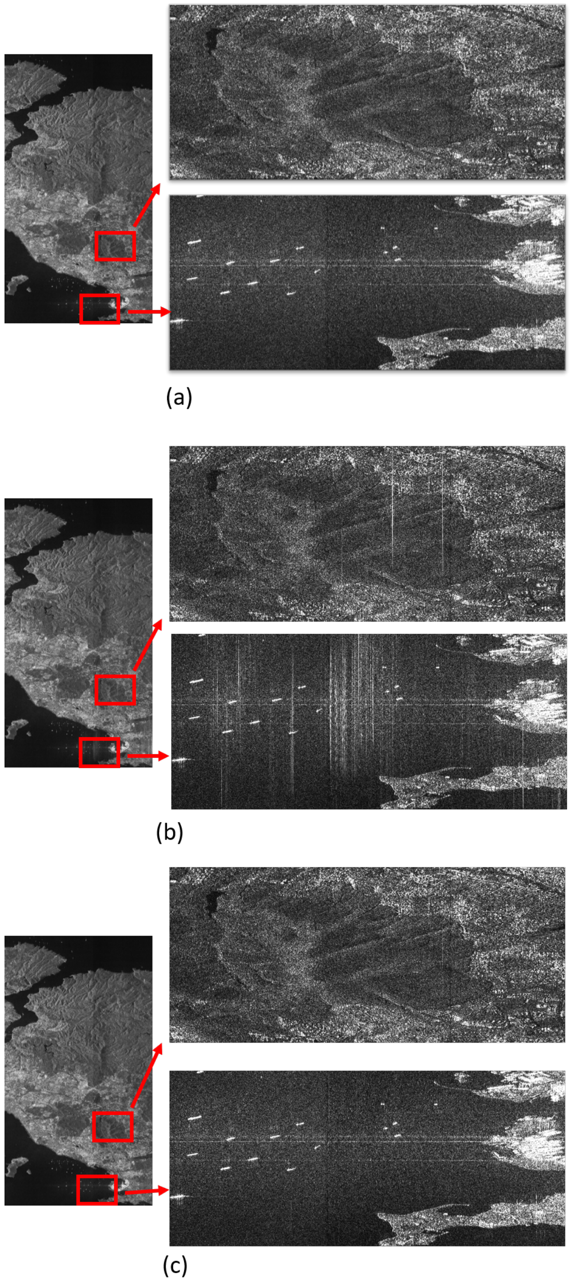

Figure 5.29: Simulated L-band SAR images: (a) ambiguity-free image; (b) ambiguous image; (c) ambiguity-suppressed image. The horizontal axis indicates the range direction, the vertical axis azimuth. Here, the spatial separation between the simulated swath segments is not visualized.

Finally, a qualitative assessment of the effectiveness of ambiguity suppression is presented in Figure 5.29. The figure compares three images: the simulated ambiguity-free SAR image, the ambiguous SAR image, and the ambiguity-suppressed SAR image. To maintain simplicity, the spatial separation between the simulated swath segments is not visualized. Accordingly, it is important to note that the brightness gap is visible, for instance, in the middle-right of the image, due to the fact that each subswath is simulated and processed individually. In fact, there is no continuity between subswaths due to the limited number of simulated samples.

To emphasize the achieved ambiguity suppression, a closer view of the areas marked by red boxes is provided in Figure 5.29. These areas demonstrate a significant improvement attributed to the proposed method, especially in backscattering surfaces such as the sea, characterized by low intensity and strongly affected by ambiguous disturbances.

5.5 Conclusions

This chapter commenced by describing the generation of range ambiguous SAR data obtained from a SAR system employing multiple elevation Rx beams to acquire an HRWS image (Section 5.1). The RABSS method was empirically analysed using SAR data affected by ambiguities stemming from a range- and Doppler-independent mixing matrix (Section 5.2). The analysis demonstrated that when dealing with the issue of range ambiguities which cannot be well suppressed when using BSS only, the stacking approach significantly improves performance. Conversely, the azimuth sub-band approach, on the other hand, slightly degrades performance. Subsequently, more realistic SAR data were presented, concentrating on multichannel SAR data obtained by a planar antenna system with SCORE (Section 5.3), leading to a range-dependent mixing matrix case. It is concluded that the azimuth sub-band decomposition approach provides no improvement due to the balanced trade-off between performance enhancement resulting from RCM and degradation due to lower bandwidth in sub-band data. Furthermore, the stacking approach yields significant improvement, highlighting the necessity of empirical analysis to determine the optimized number of stacked azimuth lines.

Furthermore, the RABSS method was applied to another SAR system, employing an array-fed reflector antenna, and the results were investigated in Section 5.4. This investigation demonstrated the effectiveness of the proposed method in handling dependencies of mixing matrix values along both the range and Doppler dimensions. The obtained results show that the method can achieve a maximum range ambiguity suppression of 16 dB, with an average suppression of 6 dB, even under challenging conditions, including five receive beams and a relatively high SNR of 10 dB.

In the more detailed discussion in Section 5.4.2, the RABSS method was compared with other methods, demonstrating that the proposed method outperforms the others. The promising results showcase the RABSS method's effectiveness in suppressing range ambiguities in SAR systems with multiple receive beams. These results indicate the potential for even greater improvement, especially for low-intensity backscattering surfaces commonly encountered over the sea, which typically exhibit high range ambiguity disturbances. However, the RABSS method performs less effectively in the far range. This is attributed to the contribution of out-of-swath ambiguity signals that are still significant in the far range subswath. It reflects the imperfect attenuation of out-of-swath range ambiguities in the far range by the Tx pattern.

It is crucial to note that the SAR image considered in the assessment displays a relatively heterogeneous distribution, indicating a non-Gaussian statistical distribution. This selectivity somewhat limits its applicability, as many real-world scenes, such as forests and seas, often exhibit homogeneity. To address this limitation, an enhanced method is proposed in Chapter 6. This method aims to tackle range ambiguities in scenarios where the scene is relatively homogeneous, complementing the current approach.

6 Calibrated Mixing Matrix Estimation Method

The range ambiguity suppression based on the higher-order blind source separation (RABSS) method has proven to be successful in various types of multichannel SAR systems. However, the SAR data considered in the previous chapters are heterogeneous and thus exhibit non-Gaussian statistics, which may not always be representative for all SAR scenarios. In the actual mission scenario, there are different types of imaged surfaces, ranging from heterogeneous to homogeneous surfaces, where the implementation of RABSS for homogeneous surfaces is expected to lead in poor performance due to Gaussian statistics. This chapter assesses the accuracy of the RABSS method in estimating the mixing matrix, a crucial element in suppressing range ambiguities. Accordingly, a comprehensive solution is provided on how the mixing matrix estimation is obtained to deal with different types of imaged surfaces, as expected in the actual mission scenario.

The chapter commences with the implementation of the RABSS method for various types of SAR data (Section 6.1), aiming to demonstrate that challenges related to the RABSS method within homogeneous SAR data do exist. Subsequently, a proposed calibrated mixing matrix estimation method is introduced in Section 6.2 to resolve the issues encountered with the RABSS method in homogeneous SAR images. In fact, Section 6.2.1 presents a comprehensive solution, named the calibrated range ambiguity suppression method and abbreviated as C-RABSS, to effectively tackle the range ambiguities problem across diverse data scenes, encompassing both heterogeneous and homogeneous images. Section 6.2.2 further includes simulation and numerical analysis of the proposed method, implemented on various multichannel SAR datasets. Finally, Section 6.3 concludes the chapter with closing remarks. Part of the material in this chapter has been published in [50], [51].

6.1 Challenges within Homogeneous SAR Images

It is discussed in [121], [122] that SAR images can be divided into homogeneous regions, heterogeneous regions, and extremely heterogeneous regions. Forested areas are an example of homogeneous regions, which are densely covered with trees of similar

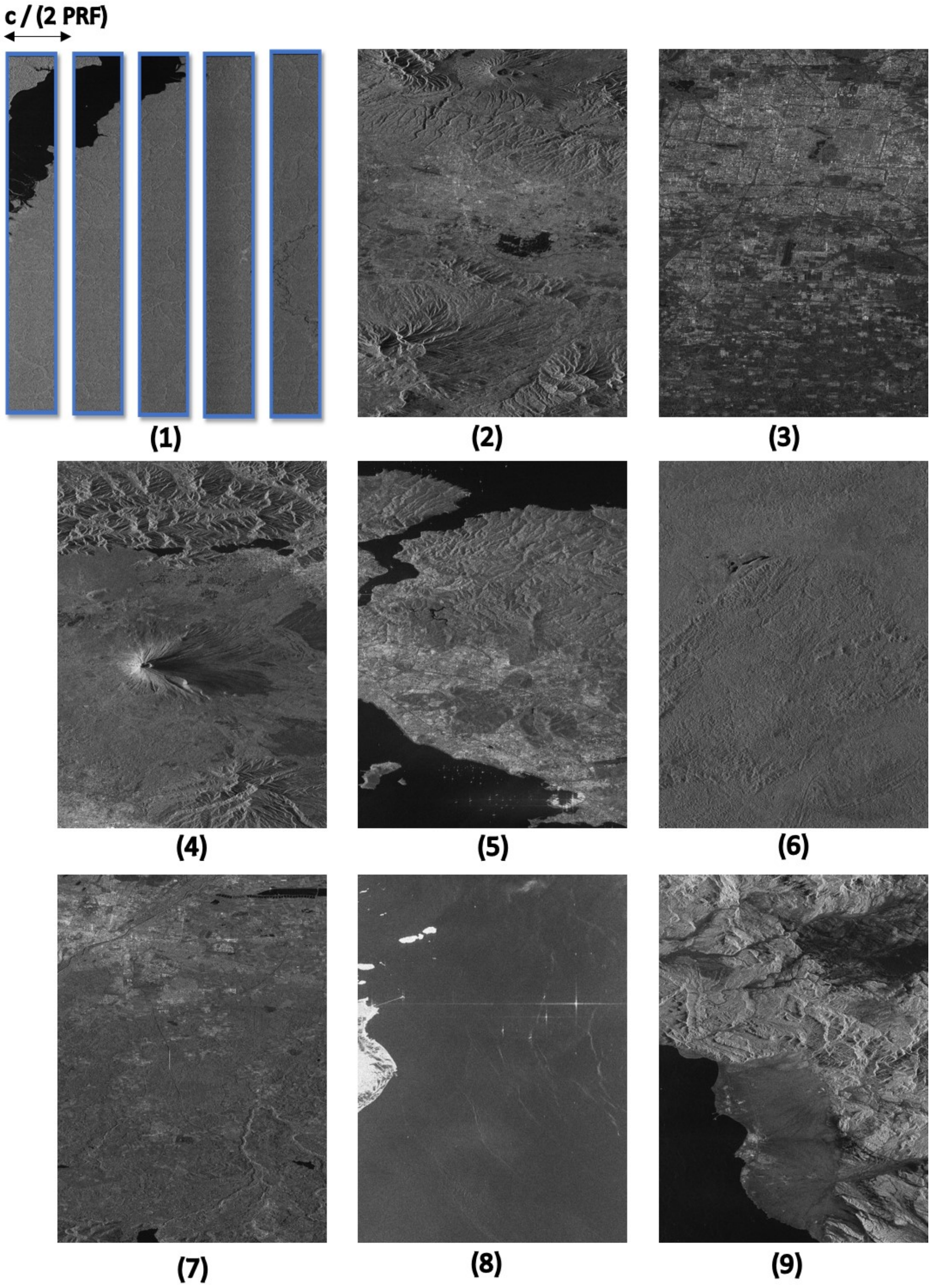

Figure 6.1: The dataset consists of nine SAR images. The horizontal axis represents the range direction, while the vertical axis represents the azimuth direction. The simulated data are derived from complex SAR image TerraSAR-X mission [112].

height and type, creating a relatively uniform landscape. In contrast, heterogeneous regions such as urban areas include buildings of various heights, roads, open spaces, and different types of structures. These different degrees of heterogeneity are related to the non-Gaussianity of the data.

Here, nine TerraSAR-X mission datasets are presented. Accordingly, the datasets are processed by the simulator utilizing an array-fed reflector antenna as demonstrated in Section 5.3 and consequently following the L-band system parameters in Table 5.4. Specifically, the simulator implements a multi-beam operational mode: a broad Tx beam illuminates a swath on the ground of approximately 300 km; a pulse repetition frequency (PRF) of 2700 Hz is chosen to achieve an azimuth resolution of 6 m; five narrow SCORE Rx beams are simulated simultaneously to collect the echoes from five mutually range-ambiguous subswaths. Accordingly, during the imaging processing, the system receives four strong ambiguous echoes. Moreover, two out-of-swath ambiguities are considered, originating from the near and far range, respectively. Furthermore, the selection of a system with an array-fed reflector antenna using SCORE is motivated by the challenges it poses in terms of the mixing matrix structure. Accordingly, the value of the mixing matrix is dependent on both range-time and Doppler-frequency. The off-diagonal elements of the mixing matrix in this case are relatively low in absolute value, which is known to be more difficult to estimate, as discussed in Section 3.4.5.

The simulated SAR data are depicted in Figure 6.1. Qualitatively, variations in homogeneity levels across the simulated data are observable: scenes (3) and (5) exhibit extreme heterogeneity, while scenes (1) and (6) are highly homogeneous; the remaining scenes fall in between these extremes. It is important to note that, although the SAR data presented in Figure 6.1 represent focused images, the input for the RABSS method are range-compressed data as proposed in Chapter 4.

The initial analysis focuses on assessing the accuracy of the RABSS method in estimating the mixing matrix, a crucial element in suppressing range ambiguities. Furthermore, the assumed mission scenario for the RABSS method is performing an adaptive estimation of mixing matrix, i.e., for the each received dataset, the mixing matrix is estimated, and subsequently, range ambiguities are suppressed. Here, each dataset has a length of approximately 50 km. This means that in this scenario, RABSS is applied over a short acquisition interval. Among the nine datasets displayed in Figure 6.1, the first example of mixing matrix estimation occurs for scene (6). Figure 6.2 illustrates a comparison between the amplitude and the phase of the estimated matrix obtained through the RABSS method and the actual mixing matrix obtained through simulation. The results indicate that the estimated matrix does not align well with the actual one, both for amplitude and phase due to the homogeneity of the dataset.

The second example of mixing matrix estimation is given for scene (5). Accordingly, Figure 6.3 shows the comparison between the estimated matrix obtained through the RABSS method and the actual mixing matrix for scene (5). The estimated mixing matrix exhibits a close agreement with the actual matrix. The RABSS method demonstrates a reliable estimation, not only in terms of amplitude, but also in phase.

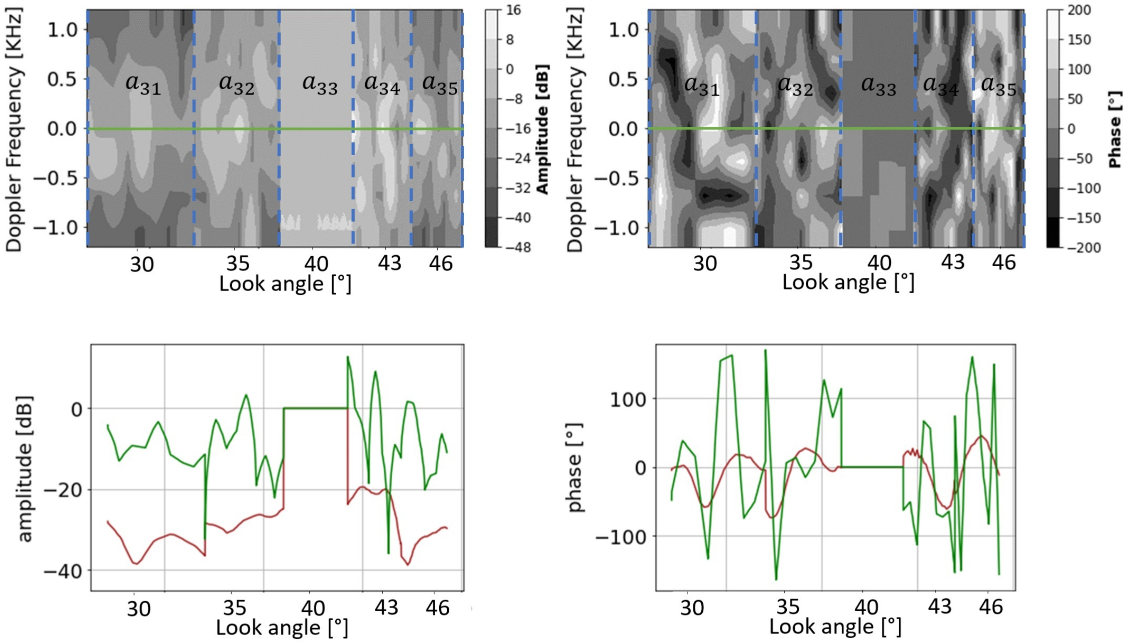

(a)

(b)

Figure 6.2: Amplitude (a) and phase (b) of the actual and estimated mixing matrix, obtained by the RABSS method implemented on scene (6) of Figure 6.1. The top plot shows the 2-D estimated mixing matrix. The bottom plot compares the estimated and actual zero-Doppler mixing matrices, indicated by the green and brown curves, respectively.

The accurate estimation of phase, besides crucial for range ambiguity suppression, also crucial for interferometry investigations.

To further numerically justify the accuracy of mixing matrix estimation, the similarity between the estimated pattern and the actual pattern is evaluated across both the range-time and Doppler-frequency domains. This similarity is quantified using the mixing matrix correlation coefficient, calculated as follows:

$$r_{\hat{a},a} = \frac{\left| \sum_{i=1}^{N\times N_a \times N_r} \left(\hat{a}_i - \bar{\hat{a}}\right)\left(a_i - \bar{a}\right) \right|}{\sqrt{\sum_{i=1}^{N\times N_a \times N_r} \left(\hat{a}_i - \bar{\hat{a}}\right)^2} \sqrt{\sum_{i=1}^{N\times N_a \times N_r} \left(a_i - \bar{a}\right)^2}}, \tag{6.1}$$

where $\hat{a}$ and a denote the estimated and actual element of the mixing matrix $\mathbf{A}$; $\bar{\hat{a}}$ and $\bar{a}$ represent the mean values of the estimated and actual matrices, respectively; N_r the number of range samples for each subswath in time domain; N_a the number of azimuth samples in Doppler domain; and N number of elevation beams. Index i refers to the index of the data samples. The value of the mixing matrix correlation

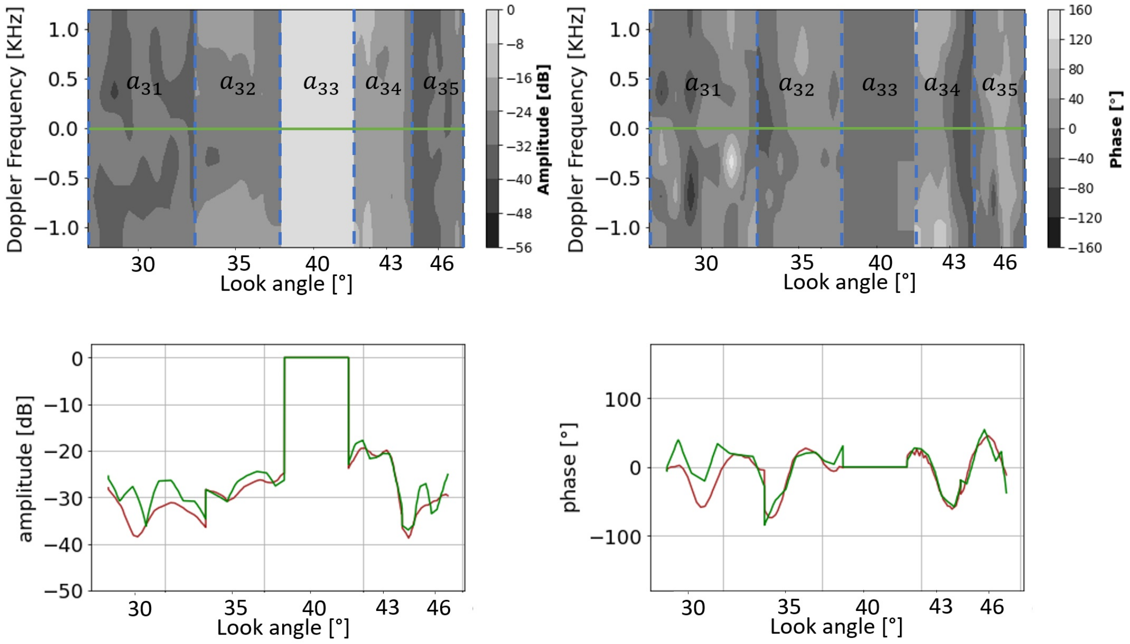

(a) (b)

Figure 6.3: Amplitude (a) and phase (b) of the actual and estimated mixing matrix, obtained by the RABSS method implemented on scene (5) of Figure 6.1. The top plot shows the 2-D estimated mixing matrix. The bottom plot compares the estimated and actual zero-Doppler mixing matrices, indicated by the green and brown curves, respectively.

coefficient, r, ranges between 0 (indicating the worst similarity) and 1 (representing the best similarity).

The matrix correlation coefficient results of the RABSS method for the datasets shown in Figure 6.1 are provided in Table 6.1. It is seen that for scenes (3) and (5) the correlation coefficients are the highest, indicating the most accurate estimation of the mixing matrix. On the other hand, scene (6) has the lowest value, indicating a poor estimation of the mixing matrix due to the homogeneity of the scene, which is quantified by the index proposed in the next section.

Table 6.1: Mixing matrix correlation coefficient

	1	2	3	4	5	6	7	8	9
Correlation coefficient	0.38	0.73	0.89	0.83	0.92	0.14	0.85	0.4	0.79

The final analysis concerns the RASR performance of the RABSS method. Figure 6.4 presents the RASR performance of the RABSS method for the datasets shown

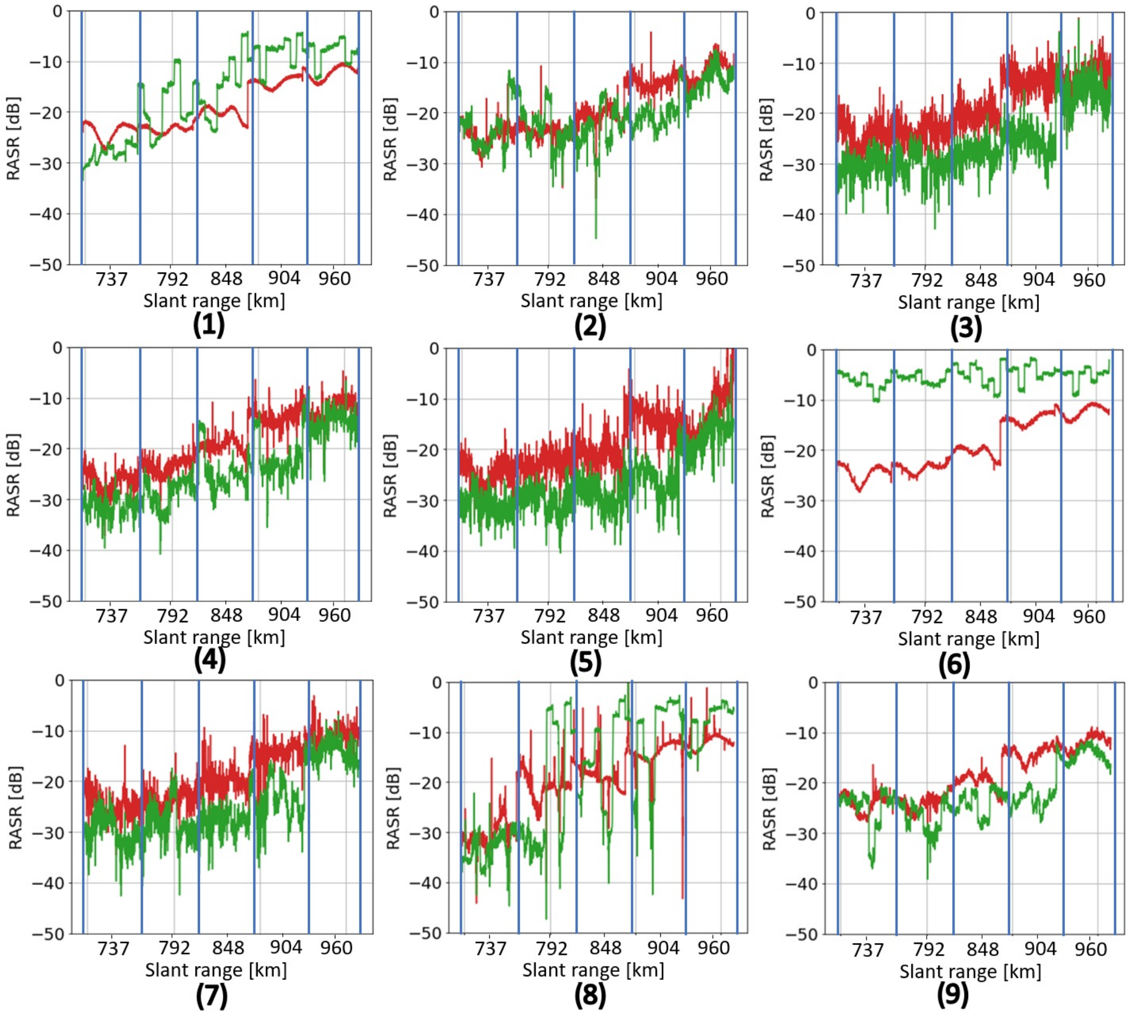

Figure 6.4: RASR performance of range ambiguity suppression method without calibration for datasets in Figure 6.1. The red and green curve show RASR for original, after range ambiguity suppression method based on HO-BSS, respectively. The blue vertical lines indicate the boundary between the simulated swath segments.

in Figure 6.1. The results reveal that the RABSS method works well in suppressing range ambiguities for heterogeneous scenes, such as those in Figure 6.1(3) and (5). On the other hand, for the homogeneous scenes, Figure 6.1(1) and (6), the RASR is actually worse after applying the RABSS method compared to before its application. Therefore, it is concluded that the RABSS method faces significant challenges when dealing with relatively homogeneous scenes.

Finally, it is worth to report that, based on the results presented in this section, a good estimation of the mixing matrix correlates with effective range ambiguity suppression. Figure 6.5 presents a plot that numerically justifies the relationship between the mixing matrix correlation coefficient and the RASR. The accurate estimation of the mixing matrix, shown by a high correlation coefficient, for instance in scene (6), leads to good range ambiguity suppression, as indicated by a low average

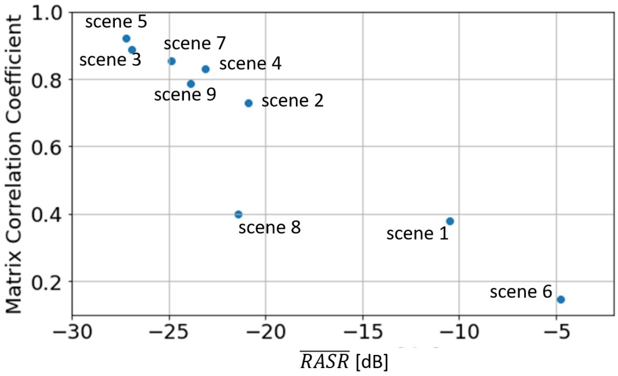

Figure 6.5: The relationship between RASR and mixing matrix correlation coefficients

RASR value. On the other hand, the poor estimation of the mixing matrix, shown by a low correlation coefficient, for instance in scene (5), leads to poor range ambiguity suppression, as indicated by a high average RASR value. Despite the general trend, Figure 6.5 reveals a peculiarity for scene (8), where a moderate estimation of the mixing matrix leads to relatively good RASR performance, at least in the near range. This is attributed to the good RASR performance at low backscattering levels in the near range (see Figure 6.4 (8) around 792 km slant range), where even a moderate estimation of the mixing matrix yields satisfactory results due to ambiguities arising from strong backscattering levels. Nevertheless, the relationship between mixing matrix estimation performance and RASR performance validates the mixing matrix as an important factor, highlighting its usefulness for the proposed calibration method detailed in the following section.

6.2 Calibrated Mixing Matrix Estimation

6.2.1 Proposed Method

The varying performance of the RABSS method for different kinds of imaged surfaces necessitates a need for a precise quantitative assessment of the suitability of SAR input data. To address this, a separation index, labeled as s_{idx}, is introduced as a quantitative measure to evaluate the homogeneity of the SAR imaged scene. In essence, the separation index serves as a means to provide an indication regarding the effectiveness of the RABSS method due to the fact that RABSS uses HO BSS as the main algorithm, and the performance of HO BSS heavily relies on the heterogeneity, i.e., non-Gaussianity, of the SAR input data.

The formulation of this index is based on Gaussianity, derived from the fourth-order cumulants, which is formulated using complex-signal kurtosis (CSK) as derived in (3.43). CSK measures the deviation of a signal's probability distribution from a

Gaussian distribution. The magnitude of the CSK is 0 for a complex Gaussian distribution, and it may have either negative or positive non-zero values for a complex non-Gaussian distribution [113]. It is worth noting that within the independent component analysis (ICA), there is no specific criterion that precisely defines the threshold for CSK level at which the method should be effective.

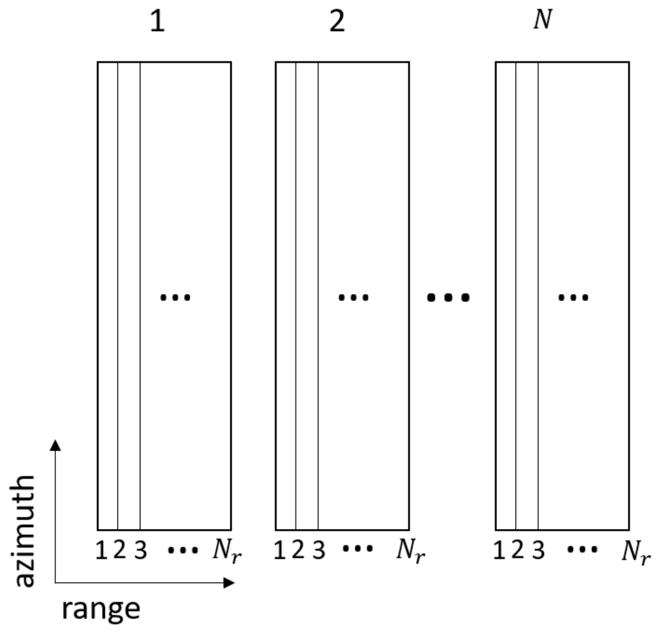

Figure 6.6: The data matrix of the SAR received signal with N elevation Rx beams.

Referring to the data matrix as illustrated in Figure 6.6, the separation index, which may vary from 0 to 10, is formulated as follows:

$$s_{idx} = \left\lfloor \frac{\sum_{i=1}^{N_r} f(i)}{N_r} \times 10 \right\rfloor, \tag{6.2}$$

where $\lfloor \cdot \rfloor$ denotes the floor operator (lower integer associated with a floating number); N_r denotes the total number of range samples for each swath; and the function $f(i)$ of the i-th range sample is given by:

$$f(i) = \begin{cases} 1, & \text{if } Y_i \geq N-1 \qquad \forall\, 1 \leq i \leq N_r \\ 0, & \text{otherwise} \end{cases}, \tag{6.3}$$

and

$$Y_i = \sum_{j=1}^{N} \Big[|\mathcal{CSK}(x_j(i))| > 2.3 \Big]. \tag{6.4}$$

Here, $\Big[\cdot \Big]$ is the Iverson bracket, serving as the indicator function that returns 1 if the condition inside is true and 0 otherwise. Furthermore, $x_j(i)$ denoting an azimuth line of the j-th Rx data matrix for each of the N imaged subswaths, $\mathcal{CSK}$ the complex signal kurtosis [113], and 2.3 being the assumed threshold value for a Gaussian distribution based on empirical evaluation (i.e., a Gaussian distribution is assumed to occur when the measured CSK value falls within the range of -2.3 to 2.3).

It is noteworthy that (6.3) is based on the principle of ICA [101]. This principle suggests that for the ICA method to achieve good performance, it is preferable for only one of the useful signals, $\mathbf{s}$, to be Gaussian. Although the input used in formulating the separation index corresponds to received signals, $\mathbf{x}$, rather than useful signals, $\mathbf{s}$, the similarity in Gaussianity between these signals is significant. Hence, the aforementioned ICA principle can be applied to the case of received signals.

As has been discussed in Section 4.2, the RABSS method involves two optimization strategies: azimuth sub-band decomposition and stacking. The former denotes as a technique where the SAR received signal is divided into several Doppler sub-bands to account for the dependence of the mixing matrix on the Doppler frequency. The SAR input data of separation index calculation, $x_j(i)$, refers to the sub-band near zero Doppler to maintain computational efficiency.

From (6.2)-(6.4) it can be seen that s_{idx} is an integer number ranging from 0 to 10: the closer the value to 10, the lower the Gaussianity of the received signal, i.e., the better the expected RABSS performance in terms of estimation of the mixing matrix. Moreover, since the Gaussianity level reflects the homogeneity of the imaged backscattering surface, an s_{idx} close to 10 denotes a heterogeneous scene.

The computed separation index value, s_{idx}, serves the purpose of quantifying the estimation of the mixing matrix by adjusting it according to the heterogeneity observed in the imaged scene. Specifically, a threshold value k_{min} is empirically determined, such that when $s_{idx} > k_{min}$, a significant heterogeneity is assumed and the basic RABSS procedure is employed to obtain the estimated separation matrix, $\hat{\mathbf{B}}$. Conversely, when $s_{idx} \leq k_{min}$, a relatively homogeneity is assumed and a different approach is adopted: instead of applying the higher-order (HO) BSS directly to the actual Rx signals, $\hat{\mathbf{B}}$ is adopted from a previously acquired scene with a $s_{idx} > k_{min}$. It is worth to remark that the selected threshold value, k_{min}, depends on the antenna pattern and the acquisition geometry and, accordingly, it remains valid for a given system and operational mode.

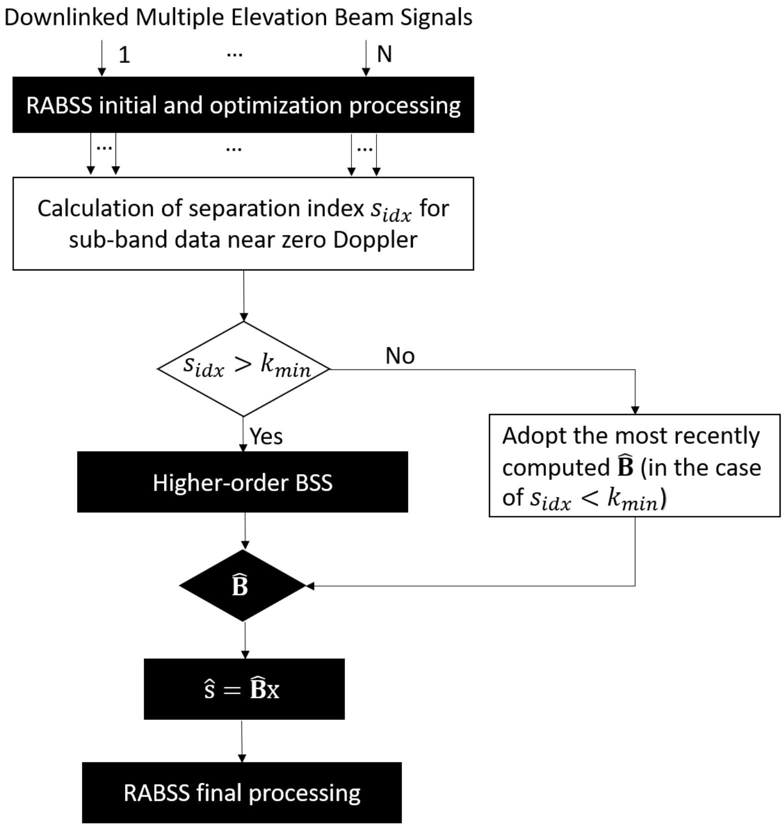

Figure 6.7: Flowchart of the C-RABSS, integrating the computation of the separation index, calibration concept, and utilizing existing features of RABSS denoted by the black boxes, such as performance optimization and blind source separation (BSS).

In a comprehensive and detailed proposal, the method, here denoted as calibrated-RABSS and abbreviated as C-RABSS, comprises four main steps as shown in Fig. 6.7. First, the separation index s_{idx} is calculated. Second, the BSS method is applied to scenes with $s_{idx} > k_{min}$, resulting in the estimated separation matrix $\hat{\mathbf{B}}$ and estimated signals $\hat{\mathbf{s}}$. It is crucial to highlight that in order to anticipate a robust performance of the BSS method, it is necessary for the scene to exhibit sufficiently strong heterogeneity. Lastly, for scenes with $s_{idx} \leq k_{min}$, the input $\mathbf{x}$ is processed using $\hat{\mathbf{B}}_{ref}$ to generate the estimated signals $\hat{\mathbf{s}}$. It is important to note that when an s_{idx} value exceeds k_{min}, the computation of the mixing matrix relies on the current acquisition scenario, even if a previous estimation with a higher s_{idx} is available. This approach ensures the accurate consideration of the actual antenna pattern shape, which might be affected by factors such as temperature or pointing variations.

In the next section, as a proof of concept, C-RABSS will be verified based on the previously presented datasets as shown in Figure 6.1, where each dataset is formed from a short acquisition interval. However, in practice, the C-RABSS method is not intended to be repetitively applied over short acquisition intervals; instead, it is applied on longer data takes and therefore serves as a periodic calibration tool. The stacking optimization approach as discussed in Section 4.2.2 and Chapter 5 indicates that longer azimuth data takes will improve the performance of the method. This means that the mixing matrix can be more precisely estimated. Additionally, longer azimuth data takes give the possibility of increasing the heterogeneity of the data. For instance, when longer data are taken, the acquired data covering the scene in Figure 6.1(1) might no longer be extremely homogeneous, because there will be a chance to meet different types of backscattering structure, which will increase the heterogeneity of the data. Furthermore, the stability of the mixing matrix can be assumed over a few consecutive acquisitions.

6.2.2 Numerical Analysis

To perform a numerical analysis of the C-RABSS method, a reference DBF HRWS SAR system based on an array-fed reflector antenna, as described in Section 5.4, is considered. Similar to the previously discussed analysis in Section 6.1, the key parameters are provided in Table 5.4, and the corresponding datasets are shown in Figure 6.1.

The initial analysis concerns the computation of the separation index, as defined in (6.2) and reported in Table 6.2. It can be seen that, as expected, scenes (1) and (6) have the lowest separation index, while scenes (3) and (5) have the highest index.

Table 6.2: Calculated separation index for different scenes in Figure 6.1.

	1	2	3	4	5	6	7	8	9
Separation Index	1	3	10	4	10	1	7	2	3

To validate the reliability of the separation index as a performance indicator for the RABSS method when applied to SAR received signals, Figure 6.8 displays the computed separation index values plotted against the average RASR performance of the RABSS method. The plot clearly demonstrates a definitive relationship between the separation index, indicating the homogeneity of the received signals, and the RASR performance: higher index values, which correspond to heterogeneous SAR received signals, lead to lower RASR values. Based on these observations, it can be concluded that the formulated separation index effectively serves as a metric for evaluating the RASR performance achieved by the RABSS method in relation to the homogeneity of the SAR received signal.

Figure 6.9 illustrates the relationship between the computed separation index and the mixing matrix correlation coefficient. The plot reveals that when RABSS is applied to a scene with a high separation index, for instance, scene (5), the accurate

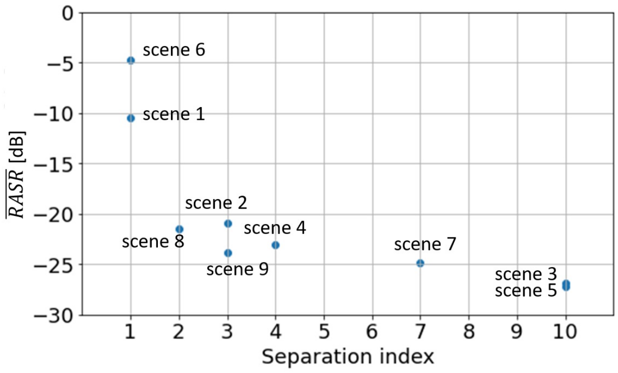

Figure 6.8: The relationship between the formulated separation index, s_{idx}, and the average RASR performance of RABSS when implemented for the scenes in Figure 6.1.

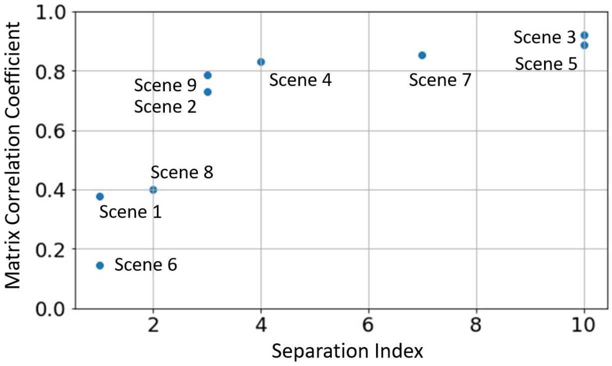

Figure 6.9: The relationship between the formulated separation index, s_{idx}, and the mixing matrix estimation of RABSS when implemented for the scenes in Figure 6.1.

estimation of the mixing matrix is obtained, shown by a high matrix correlation coefficient. On the other hand, when RABSS is applied to a scene with a low separation index, for instance, scene (6), a poor estimation of the mixing matrix is obtained, shown by a low matrix correlation coefficient. Based on these observations, it can be concluded that the formulated separation index effectively serves as a metric for evaluating the performance of mixing matrix estimation by the RABSS method in relation to the corresponding SAR received signal.

To evaluate and validate the effectiveness of the proposed method in suppressing range ambiguities, the RASR performance of the C-RABSS method for nine different datasets are presented in Figure 6.10. It is observed that, in comparison, the RASR after applying the C-RABSS method (indicated by the green curve) is lower than the RASR before applying the C-RABSS method (indicated by the red curve) for all scenes. This comparison highlights the benefit of utilizing the C-RABSS method compared to the RABSS method. Notably, when only applying the RABSS method, the homogeneous scene 1 and scene 6 exhibit significantly poorer RASR results compared to the result before the RABSS method is applied as previously shown in Figure 6.4. The findings confirm that the proposed C-RABSS method plays a crucial

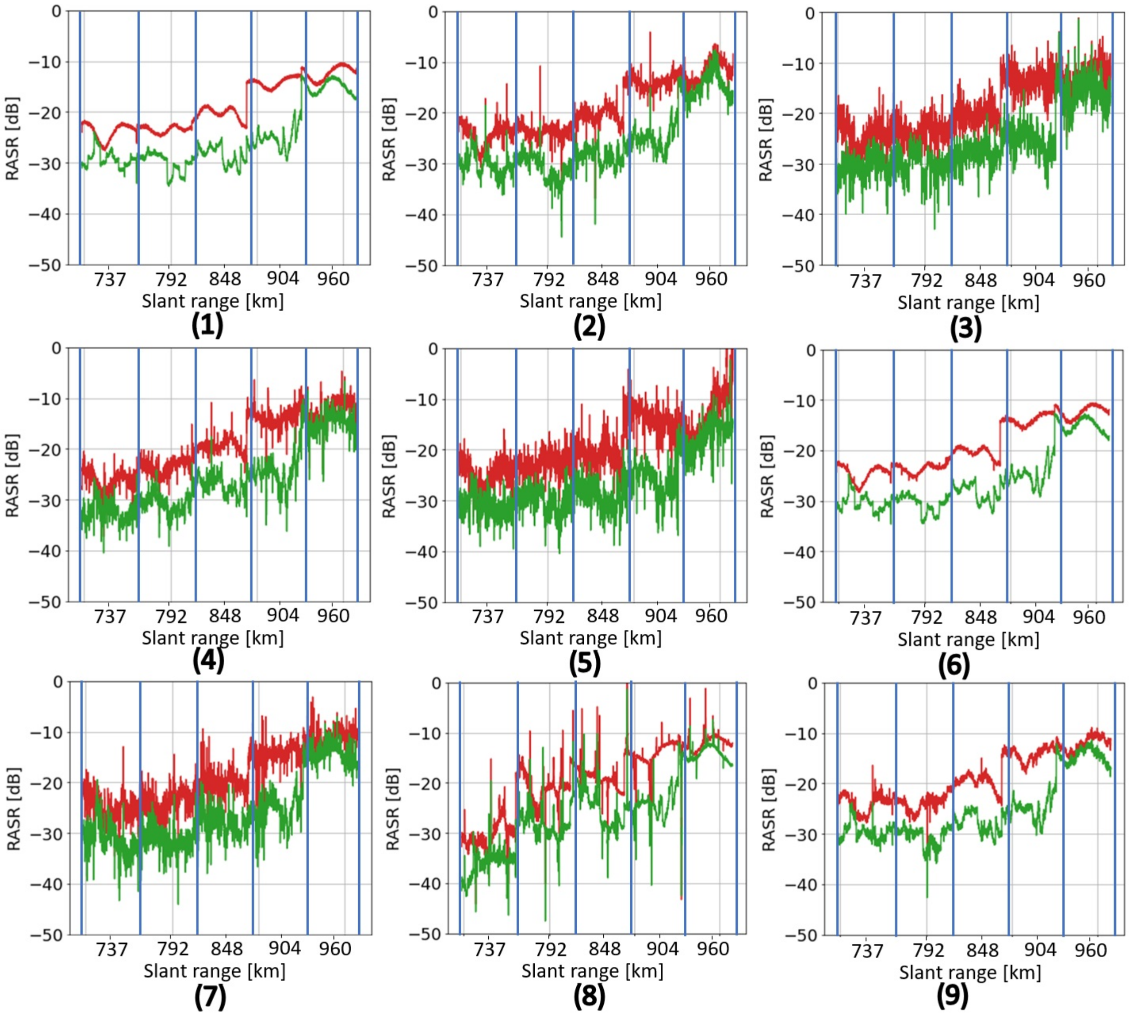

(1) (2) (3) (4) (5) (6) (7) (8) (9)

Figure 6.10: RASR performance for scenes in Figure 6.1. The red and green curves show the RASR for the original image and after C-RABSS method, respectively. The blue vertical lines indicate the boundary between the simulated swath segments.

role in enhancing the performance of range ambiguity suppression, particularly in relatively homogeneous regions.

Finally, in order to provide a qualitative assessment of the achieved ambiguity suppression, Figure 6.11 shows three simulated, focused, SAR images. They all refer to scene (8): (a) the ambiguity-free image; (b) the initial, ambiguous, image; (c) the ambiguity-suppressed image, obtained by using the proposed C-RABSS method. It is noted that each image consists of five subswaths, where each subswath is simulated and processed individually, and there is no overlap between the subswaths. Additionally, since there is no relative pattern correction, a brightness discontinuity between the subswaths is visible, for instance, in the middle right of the image. This final step can be easily implemented by a normalization factor for each sub-swath so that the resulting image preserves its radiometric calibration.

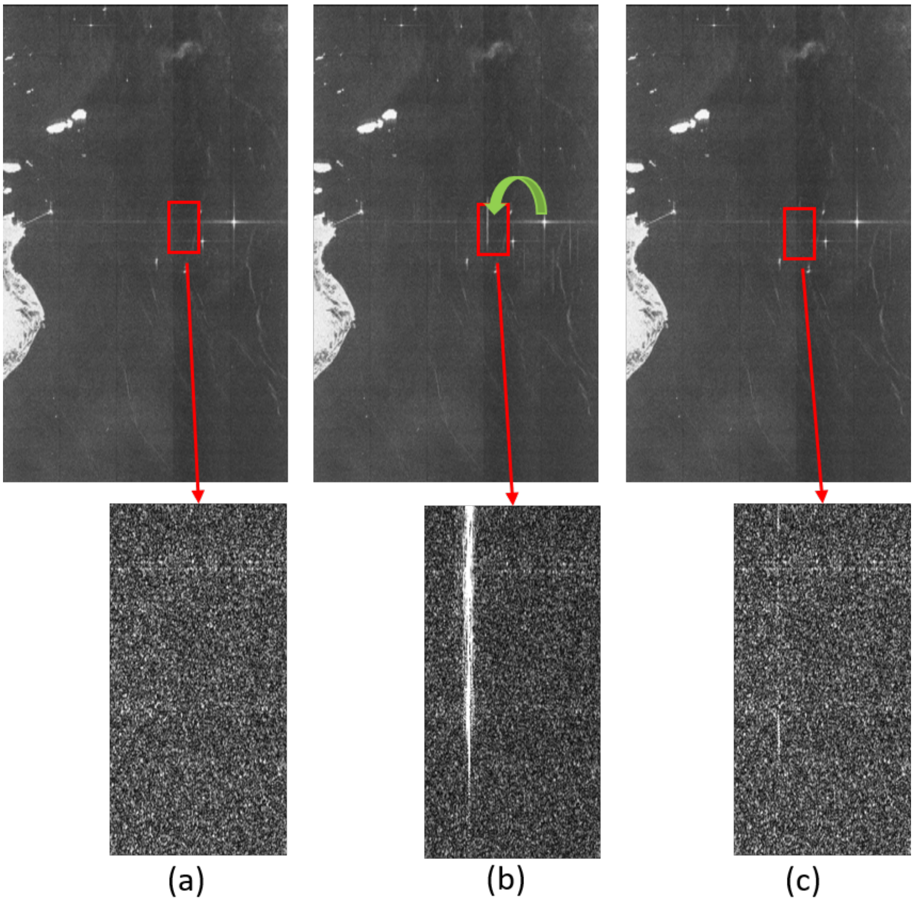

Figure 6.11: Simulated SAR scene (8) according to Fig. 6.1; (a) ambiguity-free image; (b) ambiguous image; and (c) ambiguity-suppressed image using C-RABSS method. The horizontal axis indicates the range direction, the vertical axis the azimuth direction. The spatial separation between the simulated swath segments is not visualized here. Here, no relative pattern correction is applied.

A closer examination of the areas indicated by the red boxes highlights the presence of a significant ambiguity in Fig. 6.11 (b), and demonstrates the effectiveness of the proposed C-RABSS method for range ambiguity suppression. The displayed range ambiguity disturbance originates from a strongly backscattering point-like target, located outside the red box on the right as indicated by the green arrow. Clearly recognizable for this ambiguity are the smearing in the azimuth direction due to the mismatched azimuth compression. The reduction in range ambiguities serves as a clear indication of the positive impact of the C-RABSS method in enhancing the overall quality of SAR images.

6.3 Remarks

This chapter introduced the C-RABSS method, designed to complement the RABSS method presented in Chapter 4. Its purpose is to address the limitation of the RABSS method in handling homogeneous scenes, stemming from the non-Gaussianity requirement in the HO BSS algorithm. To justify the limitation of RABSS, the RABSS method's evaluation involves nine complex-valued SAR datasets, covering both homogeneous and heterogeneous backscatter characteristics.

The C-RABSS method includes the estimation of the separation index for each acquired data set, providing an indication of whether HO BSS should be applied to such data. When the separation index is low, C-RABSS proposes adopting the separation matrix estimated from a previous high-separation index scene. Consequently, C-RABSS offers a solution capable of effectively managing various levels of scene homogeneity. The obtained results show that the RASR after the C-RABSS method is lowered by up to 18 dB, with an average lowering of 6 dB for various surface types. The C-RABSS method's effectiveness in suppressing range ambiguities independently of the specific, homogeneous or heterogeneous, backscatter of the imaged scene clearly demonstrates the superiority of C-RABSS, compared to the RABSS method. Furthermore, in practise, C-RABSS is not intended to be applied over short acquisition intervals; instead, it will based on the longer data takes, which are expected to lead to more precise and stable mixing matrix estimation, thereby serving as a periodic calibration tool.

7 Conclusion

Concluding the thesis, this chapter presents an overview of the accomplished results and provides an outlook on potential future research directions.

7.1 Thesis Objectives and Results

This thesis introduces a novel and robust method for effectively suppressing range ambiguities in SAR systems with multiple elevation beams without adding complexity on board. Chapter 2 extensively discusses the issue of range ambiguities in both conventional SAR systems and multichannel SAR systems with multiple elevation receive beams. It also justifies the significance of adopting a robust method for multiple elevation receive beam SAR, primarily due to the various errors that are often overlooked in the majority of range ambiguity suppression methods. These errors significantly impair the performance of range ambiguity suppression and, as a result, degrade the overall image quality.

In Chapter 3, the cocktail party phenomenon is analytically derived in the context of the multichannel SAR system. This derivation leads to the development of a novel concept for range ambiguity suppression, eliminating the need for any prior knowledge of the antenna pattern. The cocktail party phenomenon is closely linked to the mixing matrix, a crucial parameter that characterizes the relationship between useful signals and range ambiguities within the system, and it is directly related to the shape of the antenna pattern. Chapter 3 thoroughly discusses and derives this mixing matrix.

To address the cocktail party problem, a widely recognized technique called blind source separation (BSS) is employed and validated specifically for the multichannel SAR system. This verification demonstrates the effectiveness of blind source separation in tackling the challenges posed by the cocktail party phenomenon in SAR data processing. However, despite the suitability of the cocktail party phenomenon in classical problems and SAR, the implementation of BSS in SAR encounters significant challenges, and thus, relying solely on BSS is not sufficient for suppressing range ambiguities effectively. Section 3.3 thoroughly discusses and numerically justifies the factors that degrade the application of BSS in SAR.

To address these challenges, Chapter 4 proposes the RABSS method that combines several strategies in conjunction with the BSS technique. This method is implemented on the ground using downlinked data, adhering to one of the objectives of the thesis, which is to avoid adding complexity on board. The chosen data type for implementing the BSS technique are range-compressed data with curvature (without range cell migration compensation). The RABSS method incorporates a stacking approach, which is introduced to greatly enhance performance by providing larger datasets. Additionally, another approach involves decomposing the data into several azimuth sub-bands to handle systems where the mixing matrix values depend on Doppler frequency and to address the effect of range cell migration. Both of these strategies are considered empirically, meaning that different SAR antenna systems may have varying optimum numbers of stacked azimuth lines and azimuth sub-bands, and this is closely related to the characteristic of the antenna pattern.

In Chapter 5, the RABSS method is validated for various simulated SAR systems, which corresponds to different mixing matrix structures. Since there are currently no operational HRWS spaceborne SAR systems utilizing multiple-elevation receive beams, the chapter starts by explaining the approach used to simulate such data. The simulation is based on real input data, from the TerraSAR-X mission. To assess the RABSS method's effectiveness while disregarding the mixing matrix's dependence on range-time and Doppler frequency, it is tested in a system with a mixing matrix whose values are independent in both range-time and Doppler frequency. The results reveal that implementing the BSS technique in the range-compressed data, using a large number of samples by stacking as many azimuth lines as possible, significantly improves the ambiguity suppression performance. This demonstrates the method's strong performance in realistic SAR environments.

Next, the RABSS method is applied to two commonly used architectures in HRWS multichannel SAR systems: planar and array-fed reflector antenna systems, leading to a range-dependent and a range- and Doppler-dependent mixing matrix problem, respectively. Through empirical analysis, the study highlights the distinctions between these two architectures concerning the optimal number of stacked azimuth lines and azimuth sub-bands. In general, even under worst-case conditions, such as five sub-swaths, a realistic SNR value of 10 dB, and extremely low values of the mixing matrix, the RABSS method still achieves an additional range ambiguity suppression improvement of up to 16 dB (average improvement of approx. 6 dB).

While Chapter 5 focused solely on implementing the proposed method for one heterogeneous scene, Chapter 6 demonstrates the implementation of the RABSS method across various types of scenes, ranging from extremely homogeneous to extremely heterogeneous. The results indicate that for relatively homogeneous scenes, an additional calibration method for the mixing matrix is necessary. Consequently, this chapter introduces a calibrated mixing matrix estimation procedure, leading to an enhanced method called C-RABSS. The obtained results show that the RASR after the C-RABSS method is further improved by up to 18 dB (average improvement of 6 dB) for various surface types, resulting in a new comprehensive range ambiguity suppression method that effectively addresses range ambiguities in any type of imaged backscattering surface. The successful implementation and validation of the C-RABSS method demonstrates its capability to handle a wide range of scenarios.

Based on the presented results, the thesis is deemed successful in achieving its original objective of proposing a robust range ambiguity suppression method without detailed knowledge of the antenna pattern and without any additional on-board complexity. The method demonstrates significant potential for practical implementation in multiple elevation beams SAR systems, which are expected to be a common type of future HRWS SAR systems.

7.2 Outlook on Further Work

The range ambiguity suppression method in this thesis is designed to mitigate the strong range ambiguities that occur within the illuminated swath in multiple elevation receive beam SAR systems. Looking ahead, it would be beneficial to address the issue of out-of-swath range ambiguities originating from outside the swath. Despite being theoretically weakened due to their suppression by the Tx pattern, it has been demonstrated that in a majority of cases, the out-of-swath ambiguities from far range cannot be neglected. Introducing an auxiliary beam to collect data from this far range region is a promising solution that deserves further investigation.

The method's applicability is restricted to scenarios with multiple elevation beams featuring a constant pulse repetition interval (PRI). It cannot be directly applied to staggered SAR systems, where the PRI is varied to obtain a gapless SAR image. However, in the context of BSS, varying PRI violates the cocktail party phenomenon of the multiple elevation beams SAR, because the range ambiguity of a signal does not superimpose with the useful signal of another signal. This limitation deserves particular attention. To apply the method to staggered SAR, a calibration mode may be employed to achieve a constant PRI. Once the mixing matrix is estimated, interpolation is then performed to derive the mixing matrix for the staggered PRI. Investigating solutions like this in the future holds promise for enhancing the method's versatility and generality.

The next aspect deserving investigation is the consideration of topography, especially concerning the calibrated range ambiguity suppression method that adopts the mixing matrix from another scene. When taking topography into account, the adoption of a mixing matrix from other scenes must also consider the fact that the estimated mixing matrix should be topography-dependent. It cannot be simply adopted for other scenes, especially when they possess extremely different topographic profiles.

While the phase of the mixing matrix is well-estimated by the RABSS and C-RABSS methods, the analysis regarding how these methods impact the interferometric phase between interferometric SAR images is not included in this thesis. Such analysis deserves attention in future work.

In the future, multistatic SAR systems like MirrorSAR [130] or distributed SAR are highly desirable due to their cost-effectiveness in realizing high-resolution wide-swath imaging. The final aspect that demands particular attention is the potential application of the method in multistatic SAR configurations, where one possible imaging geometry that deserves investigation for the method's implementation involves a system with one transmit satellite and multiple receive satellites, mapping different sub-swaths. To effectively suppress range ambiguities, the geometry and antenna pattern need to be known accurately. In contrast, the proposed method offers an advantage, as it does not rely on the detailed knowledge of the antenna pattern. Consequently, it is expected to robustly suppress range ambiguities even when the relative distance dynamically changes between satellites. The key issue in applying the method in a multistatic SAR configuration concerns the misregistration between the acquired data, which could compromise the reciprocity properties and thus degrade the method's performance. An iterative approach - i.e., performing co-registration, applying the range ambiguity suppression method, and then repeating this cycle - might deserve to be investigated to refine the results.

A Joint Diagonalization

This appendix gives an explanation of joint diagonalization, which plays a crucial role within the JADE algorithm. A joint diagonalizer within the set $\mathcal{N} = \mathbf{N}_r | 1 \leq r \leq N$ of arbitrary square matrix is defined as a unitary matrix $\mathbf{V}$ that maximizes the criterion [96]:

$$C(\mathbf{V}, \mathcal{N}) = \sum_{r=1}^{N} \left\| \operatorname{diag}(\mathbf{V}^H \mathbf{N}_r \mathbf{V}) \right\|^2 . \tag{A.1}$$

Here, $\left\| \operatorname{diag}(\mathbf{V}^H \mathbf{N}_r \mathbf{V}) \right\|^2$ means the sum of squares of the diagonal. Achieving exact joint diagonalization is generally feasible only for problems involving two matrices. When dealing with more than two matrices, it remains achievable if there exists a shared structure among those matrices. Otherwise, the possibility is limited to approximate joint diagonalization.

The Jacobi technique serves as a method for approximately diagonalizing a set of arbitrary $N \times N$ matrices $\mathbf{N}_r | 1 \leq r \leq N$. The process commences with an exploration of the 2×2 case, where the matrix $\mathbf{N}_r$ takes the form:

$$\mathbf{N}_r = \begin{bmatrix} a_r & b_r \\ c_r & d_r \end{bmatrix}, \tag{A.2}$$

for $r = 1, \ldots, N$. A complex 2×2 rotation is characterized by the matrix

$$\mathbf{V} = \begin{bmatrix} \cos\theta & -e^{j\phi} \sin\theta \\ e^{-j\phi} \sin\theta & \cos\theta \end{bmatrix}. \tag{A.3}$$

It is established that the transformed matrix is given by:

$$\begin{bmatrix} a'_r & b'_r \\ c'_r & d'_r \end{bmatrix} = \begin{bmatrix} \cos\theta & e^{j\phi} \sin\theta \\ -e^{-j\phi} \sin\theta & \cos\theta \end{bmatrix} \begin{bmatrix} a_r & b_r \\ c_r & d_r \end{bmatrix} \begin{bmatrix} \cos\theta & -e^{j\phi} \sin\theta \\ e^{-j\phi} \sin\theta & \cos\theta \end{bmatrix}. \tag{A.4}$$

The objective of optimizing (A.1) is to determine suitable values for θ and ϕ such that $\sum_s |a'_r|^2 + |d'_r|^2$ is maximized. Note that $2(|a'_r|^2 + |d'_r|^2) = |a'_r - d'_r|^2 + |a'_r + d'_r|^2$ and that the trace $a'_r + d'_r$ is invariant in a unitary transformation. Therefore, the maximization of criterion (A.1) is equivalent to maximization of following cost function:

$$\mathcal{C} = \sum_r |a'_r - d'_r|^2. \tag{A.5}$$

It is verified through analysis that:

$$a'_r - d'_r = (a_r - d_r)\cos 2\theta + (b_r + c_r)\sin 2\theta \cos\phi + j(c_r - b_r)\sin 2\theta \sin\phi. \tag{A.6}$$

Furthermore, new vectors are introduced and defined as follows [94]:

$$\begin{aligned} \mathbf{u} &= [a'_1 - d'_1, ..., a'_N - d'_N]^T, \\ \mathbf{v} &= [v_1, v_2, v_3]^T = [\cos 2\theta, \sin 2\theta \cos\phi, \sin 2\theta \sin\phi]^T, \\ \mathbf{g}_r &= [a_r - d_r, b_r + c_r, j(c_r - b_r)]^T. \end{aligned} \tag{A.7}$$

Equation (A.6) can be written in the form of (A.7), such that

$$\mathbf{u} = \mathbf{G}\mathbf{v}, \tag{A.8}$$

where $\mathbf{G} = [\mathbf{g}_1, ..., \mathbf{g}_N]^T$, such that $\mathcal{C}$ in (A.5) can be rewritten as

$$\begin{aligned} \mathcal{C} &= \mathbf{u}^H\mathbf{u}, \\ &= \mathbf{v}^T\mathbf{G}^H\mathbf{G}\mathbf{v}. \end{aligned} \tag{A.9}$$

From (A.7), it is shown that $\mathbf{v}^T\mathbf{v} = 1$, therefore, equation (A.9) can be written as

$$\mathcal{C}\mathbf{v} = \mathbf{G}^H\mathbf{G}\mathbf{v}. \tag{A.10}$$

Equation (A.10) is the eigendecomposition of matrix $\mathbf{G}^H\mathbf{G}$, where the $\mathbf{v}$ is the eigenvector of $\mathbf{G}^H\mathbf{G}$, associated with the eigenvalue $\mathcal{C}$. It is reminded that, referring to description of (A.5), the goal is to find $\mathbf{v}$ which maximizes the value of $\mathcal{C}$. Furthermore, the entries of rotation matrix $\mathbf{V}$ can be computed from the $\mathbf{v}$ using Jacobi technique as described in [107].

Bibliography

[1] O. Darrigol, *Electrodynamics from Ampere to Einstein.* Oxford University Press, 2003.

[2] J. D. Kraus, "Heinrich Hertz-theorist and experimenter," *IEEE Transactions on Microwave Theory and Techniques*, vol. 36, no. 5, pp. 824–829, 1988.

[3] C. Hülsmeyer, "Verfahren, um entfernte metallische gegenstände mittels elektrischer wellen einem beobachter zu melden," *German Patent*, vol. 165, p. 30, 1904.

[4] R. Simons, "Guglielmo Marconi and early systems of wireless communication," *Gec Review*, vol. 11, no. 1, pp. 37–55, 1996.

[5] D. Pritchard, *The radar war: Germany's pioneering achievement 1904-45.* P. Stephens, 1989.

[6] R. Buderi, *The Invention That Changed the World: How a Small Group of Radar Pioneers Won the Second World War and Launched a Technological Revolution.* American Association for the Advancement of Science, 1996.

[7] M. I. Skolnik, *Radar handbook.* McGraw-Hill Education, 2008.

[8] C. A. Wiley, "Synthetic aperture radars," *IEEE Transactions on Aerospace and Electronic Systems*, no. 3, pp. 440–443, 1985.

[9] I. G. Cumming and F. H. Wong, "Digital processing of synthetic aperture radar data," *Artech house*, vol. 1, no. 3, pp. 111–231, 2005.

[10] R. L. Butterworth, "QUILL: The first imaging radar satellite," https://www.nro.gov/Portals/65/documents/foia/declass/QUILL/30.%20QUILL-The%20First%20Imaging%20Radar%20Satellite.pdf, National Reconnaissance Organzation, 2002.

[11] D. L. Evans, W. Alpers, A. Cazenave, C. Elachi, T. Farr, D. Glackin, B. Holt, L. Jones, W. T. Liu, W. McCandless *et al.*, "Seasat—a 25-year legacy of success," *Remote Sensing of Environment*, vol. 94, no. 3, pp. 384–404, 2005.

[12] E. Attema, G. Duchossois, and G. Kohlhammer, "ERS-1/2 SAR land applications: overview and main results," in *IGARSS'98. Sensing and Managing the Environment. 1998 IEEE International Geoscience and Remote Sensing. Symposium Proceedings.(Cat. No. 98CH36174)*, vol. 4. IEEE, 1998, pp. 1796–1798.

[13] K. Yoneyama, T. Koizumi, T. Suzuki, R. Kuramasu, T. Araki, C. Ishida, M. Kobayashi, and O. Kakuichi, “JERS-1 development status,” *Acta Astronautica*, vol. 21, no. 11-12, pp. 783–794, 1990.

[14] R. L. Jordan, B. L. Huneycutt, and M. Werner, “The SIR-C/X-SAR synthetic aperture radar system,” *IEEE Transactions on Geoscience and Remote Sensing*, vol. 33, no. 4, pp. 829–839, 1995.

[15] T. G. Farr and M. Kobrick, “Shuttle radar topography mission produces a wealth of data,” *Eos, Transactions American Geophysical Union*, vol. 81, no. 48, pp. 583–585, 2000.

[16] A. A. Thompson, “Overview of the radarsat constellation mission,” *Canadian Journal of Remote Sensing*, vol. 41, no. 5, pp. 401–407, 2015.

[17] N. Miranda, B. Rosich, P. J. Meadows, K. Haria, D. Small, A. Schubert, M. Lavalle, F. Collard, H. Johnsen, A. Monti-Guarnieri *et al.*, “The Envisat ASAR mission: A look back at 10 years of operation,” *ESA-SP*, no. 772, pp. 1–17, 2013.

[18] A. Rosenqvist, M. Shimada, N. Ito, and M. Watanabe, “ALOS PALSAR: A pathfinder mission for global-scale monitoring of the environment,” *IEEE Transactions on Geoscience and Remote Sensing*, vol. 45, no. 11, pp. 3307–3316, 2007.

[19] C. Livingstone, I. Sikaneta, C. Gierull, S. Chiu, and P. Beaulne, “RADARSAT-2 system and mode description,” in *Meeting Proceedings RTO-MP-SCI-150, Paper*, vol. 15, 2005.

[20] F. Covello, F. Battazza, A. Coletta, E. Lopinto, C. Fiorentino, L. Pietranera, G. Valentini, and S. Zoffoli, “COSMO-SkyMed an existing opportunity for observing the Earth,” *Journal of Geodynamics*, vol. 49, no. 3-4, pp. 171–180, 2010.

[21] G. Krieger, A. Moreira, H. Fiedler, I. Hajnsek, M. Werner, M. Younis, and M. Zink, “TanDEM-X: A satellite formation for high-resolution SAR interferometry,” *IEEE Transactions on Geoscience and Remote Sensing*, vol. 45, no. 11, pp. 3317–3341, Oct. 2007.

[22] M. Villano, N. Ustalli, L. Dell’Amore, S.-Y. Jeon, G. Krieger, A. Moreira, M. N. Peixoto, and J. Krecke, “Newspace SAR: disruptive concepts for cost-effective earth observation missions,” in *IEEE Radar Conference*. IEEE, 2020, pp. 1–5.

[23] P. Kourkouli, “Natural disaster monitoring using ICEYE SAR data,” in *Geoinformatics for Geosciences*. Elsevier, 2023, pp. 163–170.

[24] H. J. Kramer, “Umbra SAR commercial microsatellite constellation.” [Online]. Available: https://www.eoportal.org/other-space-activities/umbra#reference s

[25] G. Farquharson, W. Woods, C. Stringham, N. Sankarambadi, and L. Riggi, “The capella synthetic aperture radar constellation,” in *EUSAR 2018; 12th European Conference on Synthetic Aperture Radar.* VDE, 2018, pp. 1–5.

[26] D. Geudtner, R. Torres, P. Snoeij, M. Davidson, and B. Rommen, “Sentinel-1 system capabilities and applications,” in *2014 IEEE Geoscience and Remote Sensing Symposium.* IEEE, 2014, pp. 1457–1460.

[27] A. Moreira, G. Krieger, I. Hajnsek, K. Papathanassiou, M. Younis, P. Lopez-Dekker, S. Huber, M. Villano, M. Pardini, M. Eineder *et al.*, “Tandem-L: A highly innovative bistatic SAR mission for global observation of dynamic processes on the earth’s surface,” *IEEE Geoscience and remote sensing magazine*, vol. 3, no. 2, pp. 8–23, June 2015.

[28] K. Kellogg, P. Hoffman, S. Standley, S. Shaffer, P. Rosen, W. Edelstein, C. Dunn, C. Baker, P. Barela, Y. Shen *et al.*, “NASA-ISRO synthetic aperture radar (NISAR) mission,” in *2020 IEEE Aerospace Conference.* IEEE, 2020, pp. 1–21.

[29] G. Krieger, “SAR systems: Review and innovative concepts,” CCG SAR Intelligente Sensorik, 2016.

[30] J. Mittermayer and J. M. Martínez, “Analysis of range ambiguity suppression in SAR by up and down chirp modulation for point and distributed targets,” in *IGARSS 2003. 2003 IEEE International Geoscience and Remote Sensing Symposium. Proceedings (IEEE Cat. No. 03CH37477)*, vol. 6. IEEE, 2003, pp. 4077–4079.

[31] G. Krieger, “MIMO-SAR: Opportunities and pitfalls,” *IEEE transactions on geoscience and remote sensing*, vol. 52, no. 5, pp. 2628–2645, 2013.

[32] M. Villano, G. Krieger, and A. Moreira, “Waveform-encoded SAR: A novel concept for nadir echo and range ambiguity suppression,” in *EUSAR 2018; 12th European Conference on Synthetic Aperture Radar.* VDE, 2018, pp. 1–6.

[33] L. Dell’Amore, M. Villano, and G. Krieger, “Assessment of image quality of waveform-encoded synthetic aperture radar using real satellite data,” in *2019 20th International Radar Symposium (IRS).* IEEE, 2019, pp. 1–10.

[34] J. Dall and A. Kusk, “Azimuth phase coding for range ambiguity suppression in SAR,” in *IGARSS 2004. 2004 IEEE International Geoscience and Remote Sensing Symposium*, vol. 3. IEEE, 2004, pp. 1734–1737.

[35] A. W. Doerry, “SAR ambiguous range suppression.” Sandia National Laboratories (SNL), Albuquerque, NM, and Livermore, CA . . . , Tech. Rep., 2006.

[36] H. Wang, Y. Zhang, J. Xu, G. Liao, and S. Zhu, “Range ambiguity suppression in a synthetic aperture radar using pulse phase coding and two-pulse cancellation,” *International journal of remote sensing*, vol. 39, no. 20, pp. 6525–6539, 2018.

[37] J. Li, G.-C. Sun, X.-G. Xia, L. Guo, G.-B. Jing, M.-D. Xing, and Z. Bao, “A two-dimensional phase coding for range ambiguity suppression,” *Digital Signal Processing*, vol. 81, pp. 155–162, 2018.

[38] F. Bordoni, G. Krieger, and M. Younis, “Multifrequency subpulse SAR: Exploiting chirp bandwidth for an increased coverage,” *IEEE Geoscience and Remote Sensing Letters*, vol. 16, no. 1, pp. 40–44, 2018.

[39] S. Huber, M. Younis, A. Patyuchenko, G. Krieger, and A. Moreira, “Spaceborne reflector SAR systems with digital beamforming,” *IEEE transactions on aerospace and electronic systems*, vol. 48, no. 4, pp. 3473–3493, 2012.

[40] S. Huber, F. Q. de Almeida, M. Villano, M. Younis, G. Krieger, and A. Moreira, “Tandem-L: A technical perspective on future spaceborne SAR sensors for earth observation,” *IEEE Transactions on Geoscience and Remote Sensing*, vol. 56, no. 8, pp. 4792–4807, 2018.

[41] F. Feng, S. Li, W. Yu, P. Huang, and W. Xu, “Echo separation in multidimensional waveform encoding SAR remote sensing using an advanced null-steering beamformer,” *IEEE Transactions on Geoscience and Remote Sensing*, vol. 50, no. 10, pp. 4157–4172, 2012.

[42] Q. Zhao, Y. Zhang, W. Wang, Y. Deng, W. Yu, Y. Zhou, and R. Wang, “Echo separation for space-time waveform-encoding SAR with digital scalloped beamforming and adaptive multiple null-steering,” *IEEE Geoscience and Remote Sensing Letters*, 2020.

[43] G. Krieger, S. Huber, M. Younis, A. Moreira, J. Reimann, P. Klenk, M. Zink, M. Villano, and F. Q. de Almeida, “In-orbit relative amplitude and phase antenna pattern calibration for Tandem-L,” in *EUSAR 2018; 12th European Conference on Synthetic Aperture Radar*. VDE, 2018, pp. 1–6.

[44] J. Reimann, M. Schwerdt, K. Schmidt, N. T. Ramon, and B. Döring, “The DLR spaceborne SAR calibration center,” *Frequenz*, vol. 71, no. 11-12, pp. 619–627, 2017.

[45] M. Schwerdt, B. Brautigam, M. Bachmann, B. Doring, D. Schrank, and J. H. Gonzalez, “Final TerraSAR-X calibration results based on novel efficient methods,” *IEEE Transactions on Geoscience and Remote Sensing*, vol. 48, no. 2, pp. 677–689, 2009.

[46] G. Krieger, S. Huber, M. Villano, M. Younis, T. Rommel, P. L. Dekker, F. Q. de Almeida, and A. Moreira, “CEBRAS: Cross elevation beam range ambiguity suppression for high-resolution wide-swath and MIMO-SAR imaging,” in *2015 IEEE International Geoscience and Remote Sensing Symposium (IGARSS)*. IEEE, 2015, pp. 196–199.

[47] E. J. Amin, M. Younis, and G. Krieger, “Blind source separation: A novel range ambiguity suppression method in multichannel SAR,” in *ARSI Advanced Remote Sensing Instruments Conference*, 2019.

[48] E. Amin, M. Younis, and G. Krieger, “Two-dimensional range ambiguity suppression in multichannel SAR using blind source separation method,” in *EUSAR 2021; 13th European Conference on Synthetic Aperture Radar*. VDE, 2021, pp. 1–5.

[49] E. J. Amin, G. Krieger, M. Younis, F. Bordoni, A. B. C. da Silva, and A. Moreira, “A 2-D range ambiguity suppression method based on blind source separation for multichannel SAR systems,” *IEEE Transactions on Geoscience and Remote Sensing*, vol. 62, pp. 1–17, 2024.

[50] E. J. Amin, G. Krieger, M. Younis, F. Bordoni, and A. Moreira, “Mixing matrix calibration for BSS range ambiguity suppression in multichannel SAR systems,” *IEEE Geoscience and Remote Sensing Letters*, pp. 1–1, 2024.

[51] E. J. Amin, F. Bordoni, G. Krieger, M. Younis, and A. Moreira, “Insights on range ambiguity suppression based on blind source separation in multichannel SAR systems,” in *EUSAR 2024; 15th European Conference on Synthetic Aperture Radar*. VDE, 2024.

[52] S. Chang, Y. Deng, Y. Zhang, Q. Zhao, R. Wang, and K. Zhang, “An advanced scheme for range ambiguity suppression of spaceborne SAR based on blind source separation,” *IEEE Transactions on Geoscience and Remote Sensing*, June 2022.

[53] S. Chang, Y. Deng, Y. Zhang, R. Wang, J. Qiu, W. Wang, Q. Zhao, and D. Liu, “An advanced echo separation scheme for space-time waveform-encoding SAR based on digital beamforming and blind source separation,” *Remote Sensing*, vol. 14, no. 15, p. 3585, July 2022.

[54] J. C. Curlander and R. N. McDonough, *Synthetic aperture radar*. Wiley, New York, 1991, vol. 11.

[55] A. Freeman, W. T. Johnson, B. Huneycutt, R. Jordan, S. Hensley, P. Siqueira, and J. Curlander, “The myth of the minimum SAR antenna area constraint,” *IEEE Transactions on Geoscience and Remote Sensing*, vol. 38, no. 1, pp. 320–324, 2000.

[56] M. Younis and T. Bollian, “Circular orbit SAR geometry,” German Aerospace Center, Microwaves and Radar Institute, Technical Note TN-RK-ST-TN7562, issue 1.6, Mar. 2024.

[57] A. Moreira, J. Mittermayer, and R. Scheiber, “Extended chirp scaling algorithm for air-and spaceborne SAR data processing in stripmap and ScanSAR imaging modes,” *IEEE Transactions on geoscience and remote sensing*, vol. 34, no. 5, pp. 1123–1136, 1996.

[58] G. Di Martino and A. Iodice, “Coprime synthetic aperture radar (CopSAR): A new acquisition mode for maritime surveillance,” *IEEE Transactions on Geoscience and Remote Sensing*, vol. 53, no. 6, pp. 3110–3123, 2014.

[59] D. Velotto, M. Soccorsi, and S. Lehner, “Azimuth ambiguities removal for ship detection using full polarimetric X-band SAR data,” *IEEE transactions on geoscience and remote sensing*, vol. 52, no. 1, pp. 76–88, 2013.

[60] A. Moreira, “Suppressing the azimuth ambiguities in synthetic aperture radar images,” *IEEE Transactions on Geoscience and Remote Sensing*, vol. 31, no. 4, pp. 885–895, 1993.

[61] M. Süß, B. Grafmüller, and R. Zahn, “A novel high resolution, wide swath SAR system,” in *IGARSS 2001. Proceedings. IEEE 2001 International Geoscience and Remote Sensing Symposium*, vol. 3. IEEE, 2001, pp. 1013–1015.

[62] N. Gebert, G. Krieger, and A. Moreira, “Digital beamforming on receive: Techniques and optimization strategies for high-resolution wide-swath SAR imaging,” *IEEE Transactions on Aerospace and Electronic Systems*, vol. 45, no. 2, pp. 564–592, 2009.

[63] M. Younis and W. Wiesbeck, “SAR with digital beamforming on receive only,” in *IEEE 1999 International Geoscience and Remote Sensing Symposium. IGARSS’99 (Cat. No. 99CH36293)*, vol. 3. IEEE, 1999, pp. 1773–1775.

[64] M. Younis, C. Fischer, and W. Wiesbeck, “Digital beamforming in SAR systems,” *IEEE Transactions on Geoscience and Remote Sensing*, vol. 41, no. 7, pp. 1735–1739, 2003.

[65] S. Huber, “Spaceborne SAR systems with digital beamforming and reflector antenna,” Ph.D. dissertation, Deutsches Zentrum für Luft-und Raumfahrt e. V., 2014.

[66] S. Huber, M. Younis, A. Patyuchenko, and G. Krieger, “A novel digital beamforming concept for spaceborne reflector SAR systems,” in *European Radar Conference (EuRAD)*. IEEE, 2009, pp. 238–241.

[67] A. Freeman, G. Krieger, P. Rosen, M. Younis, W. T. Johnson, S. Huber, R. Jordan, and A. Moreira, “SweepSAR: Beam-forming on receive using a reflector-phased array feed combination for spaceborne SAR,” in *2009 IEEE Radar Conference*. IEEE, 2009, pp. 1–9.

[68] F. Q. de Almeida, M. Younis, G. Krieger, S. Hensley, and A. Moreira, “Investigation into the weight update rate for scan-on-receive beamforming,” in *IEEE Radar Conference (RadarConf20)*. IEEE, 2020, pp. 1–6.

[69] F. Feng, H. Dang, X. Tan, G. Li, and C. Li, “An improved scheme of digital beam-forming in elevation for spaceborne SAR,” in *IET International Radar Conference*. IET, 2013, pp. 1–6.

[70] H. L. Van Trees, *Optimum array processing: Part IV of detection, estimation, and modulation theory*. John Wiley & Sons, 2002.

[71] J. Capon, “High-resolution frequency-wavenumber spectrum analysis,” *Proceedings of the IEEE*, vol. 57, no. 8, pp. 1408–1418, 1969.

[72] S. Huber, M. Younis, G. Krieger, and A. Moreira, “Error analysis for digital beamforming synthetic aperture radars: A comparison of phased array and array-fed reflector systems,” *IEEE Transactions on Geoscience and Remote Sensing*, vol. 59, no. 8, pp. 6314–6322, 2020.

[73] E. Jaska, L. Corey, and S. Park, “Effects of random amplitude and phase errors on monopulse null depth in phased-array antennas,” in *International Symposium on Antennas and Propagation Society, Merging Technologies for the 90's.* IEEE, 1990, pp. 836–839.

[74] V. Shahmirian and A. Daryoush, “Pattern degradation due to random errors in active phased array antennas,” in *Digest on Antennas and Propagation Society International Symposium.* IEEE, 1989, pp. 396–399.

[75] M. Villano, G. Krieger, and A. Moreira, “Advanced spaceborne SAR systems with planar antenna,” in *IEEE Radar Conference (RadarConf).* IEEE, 2017, pp. 0152–0156.

[76] M. Bachmann, M. Schwerdt, and B. Brautigam, “TerraSAR-X antenna calibration and monitoring based on a precise antenna model,” *IEEE Transactions on Geoscience and Remote Sensing*, vol. 48, no. 2, pp. 690–701, 2009.

[77] J. Mi, H. Sun, Y. Xing, X. Zhao, J. Li *et al.*, “SAR antenna pattern measurement by internal calibration method for GF-3 satellite,” *International Journal of Antennas and Propagation*, vol. 2022, 2022.

[78] J. P. Kroll, M. Younis, and G. Krieger, “Clutter-based calibration for multichannel synthetic aperture radar instruments,” 2024, to be submitted.

[79] F. Q. de Almeida, “Multichannel staggered SAR for high-resolution wide-swath imaging,” Ph.D. dissertation, Deutsches Zentrum für Luft-und Raumfahrt, 2018.

[80] M. Younis, S. Huber, A. Patyuchenko, F. Bordoni, and G. Krieger, “Performance comparison of reflector-and planar-antenna based digital beam-forming SAR,” *International Journal of Antennas and Propagation*, vol. 2009, no. 1, p. 614931, 2009.

[81] F. Bordoni, M. Younis, E. Makhoul Varona, N. Gebert, and G. Krieger, “Performance investigation on scan-on-receive and adaptive digital beam-forming for high-resolution wide-swath synthetic aperture radar,” in *Proceedings of the International ITG Workshop of Smart Antennas*, 2009, pp. 114–121.

[82] S. Zhang, B. Duan, G. Yang, Y. Zong, and Y. Zhang, “An approximation of pattern analysis for distorted reflector antennas using structural-electromagnetic coupling model,” *IEEE transactions on antennas and propagation*, vol. 61, no. 9, pp. 4844–4847, 2013.

[83] K. Mouthaan, “Digital beamforming for spaceborne reflector SAR systems via FIR filter networks in the presence of uncertainties,” 2017.

[84] F. C. Reis Pinheiro, "Investigation of alternatives for the calibration of reflector-antenna SAR systems with multiple azimuth channels," Ph.D. dissertation, Instituto Tecnológico de Aeronáutica, 2019.

[85] W. T. Smith and R. J. Bastian, "An approximation of the radiation integral for distorted reflector antennas using surface-error decomposition," *IEEE Transactions on Antennas and Propagation*, vol. 45, no. 1, pp. 5–10, 1997.

[86] M. Younis, T. Rommel, F. Bordoni, G. Krieger, and A. Moreira, "On the pulse extension loss in digital beamforming SAR," *IEEE Geoscience and Remote Sensing Letters*, vol. 12, no. 7, pp. 1436–1440, 2015.

[87] F. Bordoni, G. Krieger, and D. Lind, "Radiometric degradation associated with terrain height variations and pulse duration in scan-on-receive SAR images," *IEEE Transactions on Geoscience and Remote Sensing*, vol. 60, pp. 1–14, 2022.

[88] E. C. Cherry, "Some experiments on the recognition of speech, with one and with two ears," *The Journal of the acoustical society of America*, vol. 25, no. 5, pp. 975–979, 1953.

[89] N. Moray, "Attention in dichotic listening: Affective cues and the influence of instructions," *Quarterly journal of experimental psychology*, vol. 11, no. 1, pp. 56–60, 1959.

[90] C. Jutten and J. Herault, "Blind separation of sources, part I: An adaptive algorithm based on neuromimetic architecture," *Signal processing*, vol. 24, no. 1, pp. 1–10, 1991.

[91] M. Villano, G. Krieger, and A. Moreira, "Nadir echo removal in synthetic aperture radar via waveform diversity and dual-focus postprocessing," *IEEE Geoscience and remote sensing letters*, vol. 15, no. 5, pp. 719–723, 2018.

[92] O. Dogan, V. Ignatenko, D. Muff, P. Leprovost, L. Lamentowsky, M. Nottinghama, A. Radius, and T. Seilonen, "Double dual focusing for range ambiguity suppression-experimental results," in *EUSAR 2022; 14th European Conference on Synthetic Aperture Radar.* VDE, 2022, pp. 1–6.

[93] L. Tong, V. Soon, Y. Huang, and R. Liu, "AMUSE: a new blind identification algorithm," in *IEEE international symposium on circuits and systems.* IEEE, 1990, pp. 1784–1787.

[94] A. Belouchrani, K. Abed-Meraim, J.-F. Cardoso, and E. Moulines, "A blind source separation technique using second-order statistics," *IEEE Transactions on signal processing*, vol. 45, no. 2, pp. 434–444, Feb. 1997.

[95] P. Comon, "Independent component analysis, a new concept?" *Signal processing*, vol. 36, no. 3, pp. 287–314, Apr. 1994.

[96] J.-F. Cardoso and A. Souloumiac, "Blind beamforming for non-Gaussian signals," in *IEE proceedings F (radar and signal processing)*, vol. 140, no. 6. IET, 1993, pp. 362–370.

[97] M. H. Fatnan, Z. M. Hussain, and H. R. Mohammed, “Blind source separation under semi-white Gaussian noise and uniform noise: Performance analysis of ICA, Sobi and JadeR,” *journal of Computer Science*, vol. 21, p. 22, 2019.

[98] N. Liu, J. Li, Q. Liu, H. Su, and W. Wu, “Blind source separation using higher order statistics in kernel space,” *COMPEL: The International Journal for Computation and Mathematics in Electrical and Electronic Engineering*, vol. 35, no. 1, pp. 289–304, 2016.

[99] S. Liu, B. Wang, and L. Zhang, “Blind source separation method based on neural network with bias term and maximum likelihood estimation criterion,” *Sensors*, vol. 21, no. 3, p. 973, 2021.

[100] A. Papoulis, *Probability and statistics.* Prentice-Hall, Inc., 1990.

[101] A. Hyvärinen and E. Oja, “Independent component analysis: algorithms and applications,” *Neural networks*, vol. 13, no. 4-5, pp. 411–430, 2000.

[102] J. Shlens, “A tutorial on independent component analysis,” *arXiv preprint arXiv:1404.2986*, 2014.

[103] A. Hyvarinen, J. Karhunen, and E. Oja, “Independent component analysis,” *Studies in informatics and control*, vol. 11, no. 2, pp. 205–207, 2002.

[104] P. Comon and J.-F. Cardoso, “Eigenvalue decomposition of a cumulant tensor with applications,” in *Advanced Signal Processing Algorithms, Architectures, and Implementations*, vol. 1348. SPIE, 1990, pp. 361–372.

[105] D. R. Brillinger, *Time series: data analysis and theory.* SIAM, 2001.

[106] P. Comon, “Tensor diagonalization, a useful tool in signal processing,” *IFAC Proceedings Volumes*, vol. 27, no. 8, pp. 77–82, 1994.

[107] G. H. Golub and C. F. Van Loan, *Matrix computations.* JHU press, 2013, vol. 3.

[108] X. Yu, D. Hu, and J. Xu, *Blind source separation: theory and applications.* John Wiley & Sons, 2013.

[109] P. Comon and C. Jutten, *Handbook of Blind Source Separation: Independent component analysis and applications.* Academic press, 2010.

[110] A. Ziehe, “Blind source separation based on joint diagonalization of matrices with applications in biomedical signal processing,” Ph.D. dissertation, Universität Potsdam, 2005.

[111] Z. Luo, C. Li, and L. Zhu, “A comprehensive survey on blind source separation for wireless adaptive processing: Principles, perspectives, challenges and new research directions,” *IEEE Access*, vol. 6, pp. 66 685–66 708, 2018.

[112] R. Werninghaus and S. Buckreuss, “The TerraSAR-X mission and system design,” *IEEE Transactions on Geoscience and Remote Sensing*, vol. 48, no. 2, pp. 606–614, 2009.

[113] X. Leng, K. Ji, S. Zhou, and X. Xing, “Ship detection based on complex signal kurtosis in single-channel SAR imagery,” *IEEE Transactions on Geoscience and Remote Sensing*, vol. 57, no. 9, pp. 6447–6461, Apr. 2019.

[114] E. Ollila, J. Eriksson, and V. Koivunen, “Complex elliptically symmetric random variables—generation, characterization, and circularity tests,” *IEEE Transactions on Signal Processing*, vol. 59, no. 1, pp. 58–69, Oct. 2010.

[115] J. Fischer, U. Benz, and A. Moreira, “Efficient SAR raw data compression in frequency domain,” in *IEEE 1999 International Geoscience and Remote Sensing Symposium. IGARSS’99 (Cat. No. 99CH36293)*, vol. 4. IEEE, 1999, pp. 2261–2263.

[116] K. J. Sangston, F. Gini, M. V. Greco, and A. Farina, “Structures for radar detection in compound Gaussian clutter,” *IEEE Transactions on Aerospace and Electronic Systems*, vol. 35, no. 2, pp. 445–458, 1999.

[117] K. Adhikari and S. Kay, “Optimal sparse sampling for detection of a known signal in nonwhite Gaussian noise,” *IEEE Signal Processing Letters*, vol. 28, pp. 1908–1912, 2021.

[118] J. R. Voss, L. Rademacher, and M. Belkin, “Fast algorithms for Gaussian noise invariant independent component analysis,” *Advances in neural information processing systems*, vol. 26, 2013.

[119] F. He, X. Ma, Z. Dong, and D. Liang, “Digital beamforming on receive in elevation for multidimensional waveform encoding SAR sensing,” *IEEE Geoscience and Remote Sensing Letters*, vol. 11, no. 12, pp. 2173–2177, 2014.

[120] G. Krieger, N. Gebert, and A. Moreira, “Multidimensional waveform encoding: A new digital beamforming technique for synthetic aperture radar remote sensing,” *IEEE Transactions on Geoscience and Remote Sensing*, vol. 46, no. 1, pp. 31–46, 2007.

[121] A. C. Frery, H.-J. Muller, C. d. C. F. Yanasse, and S. J. S. Sant’Anna, “A model for extremely heterogeneous clutter,” *IEEE transactions on geoscience and remote sensing*, vol. 35, no. 3, pp. 648–659, 1997.

[122] G. Gao, “Statistical modeling of SAR images: A survey,” *Sensors*, vol. 10, no. 1, pp. 775–795, 2010.

[123] J. M. Herrmann and F. J. Theis, “Statistical analysis of sample-size effects in ICA,” in *International Conference on Intelligent Data Engineering and Automated Learning.* Springer, 2007, pp. 416–425.

[124] F. Bordoni, D. Lind, A. Jakobsson, and G. Krieger, “Unconventional sources of error in high-resolution wide-swath SAR systems based on scan-on-receive,” in *EUSAR 2021; 13th European Conference on Synthetic Aperture Radar.* VDE, 2021, pp. 1–4.

[125] C. A. Balanis, *Antenna theory: analysis and design.* Wiley-Interscience, 2005.

[126] R. A. Monzingo and T. W. Miller, *Introduction to adaptive arrays.* Scitech publishing, 2004.

[127] D. D'Aria, D. Giudici, A. M. Guarnieri, P. Rizzoli, and J. Medina, "A wide swath, full polarimetric, L band spaceborne SAR," in *IEEE Radar Conference*. IEEE, 2008, pp. 1–4.

[128] H. Skriver, "Land-cover map information from polarimetric SAR using knowledge-based techniques," in *In: Proceedings of the Third International Symposium on Retrieval of Bio-and Geophysical Parameters from SAR Data for Land Applications*, vol. 475, 2002, pp. 105–110.

[129] D. Rigie, "Second-Order Blind Identification," https://github.com/davidrigie/sobi/blob/master/sobi/sobi.py, 2018.

[130] J. Mittermayer, G. Krieger, A. Bojarski, M. Zonno, M. Villano, M. Pinheiro, M. Bachmann, S. Buckreuss, and A. Moreira, "MirrorSAR: An HRWS add-on for single-pass multi-baseline SAR interferometry," *IEEE Transactions on Geoscience and Remote Sensing*, vol. 60, pp. 1–18, Dec. 2021.

Publications

Journal Publications

1. Ershad Junus Amin, Gerhard Krieger, Marwan Younis, Federica Bordoni, André Barros Cardoso da Silva, and Alberto Moreira. A 2-D range ambiguity suppression method based on blind source separation for multichannel SAR systems. *IEEE Transactions on Geoscience and Remote Sensing*, 62:1–17, 2024.
2. Ershad Junus Amin, Gerhard Krieger, Marwan Younis, Federica Bordoni, and Alberto Moreira. Mixing matrix calibration for BSS range ambiguity suppression in multichannel SAR systems. *IEEE Geoscience and Remote Sensing Letters*, pages 1–1, 2024.

Conference Publications

1. Ershad Amin, Marwan Younis, and Gerhard Krieger. Two-dimensional range ambiguity suppression in multichannel SAR using blind source separation method. In *EUSAR 2021; 13th European Conference on Synthetic Aperture Radar*, pages 1–5. VDE, 2021.
2. Ershad Junus Amin, Federica Bordoni, Gerhard Krieger, Marwan Younis, and Alberto Moreira. Insights on range ambiguity suppression based on blind source separation in multichannel SAR systems. In *EUSAR 2024; 15th European Conference on Synthetic Aperture Radar*. VDE, 2024.
3. Ershad Junus Amin, Marwan Younis, and Gerhard Krieger. Blind source separation: A novel range ambiguity suppression method in multichannel SAR. In *ARSI Advanced Remote Sensing Instruments Conference*, 2019.